Analog quantum simulator for the Tavis-Cummings model with superconducting qubits

Zur Erlangung des akademischen Grades eines
DOKTORS DER NATURWISSENSCHAFTEN
der Fakultät für Physik des
Karlsruher Instituts für Technologie (KIT)

genehmigte
Dissertation
von

M. Sc. Ping Yang

Contents

1 Introduction

Back in the year 1959 in the lecture "There's Plenty of Room at the Bottom" [Fey59], for the first time, Richard Feynman declared the possibility to employ quantum effect for computation. However, it was 22 years later when Paul Benioff built the Hamiltonian models of computers [Ben80]. From then on, quantum computing has been developing, and especially fast over the past 2 decades. Why is quantum computer so fascinating? Because "with a suitable class of quantum machines you could imitate any quantum system, including the physical world", said Richard Feynman [Fey82a].

The building block of a classical computer is the binary bit, which represents either zero or one. In contrast, for quantum computer, the building block is called quantum bit (qubit), which can be state zero or state one, or any arbitrary superposition of these two eigenstates of the qubit [NC02]. Thus, a quantum computer with N qubits could be in any arbitrary superposition of maximum 2^N states at the same time (without measurement). However, a classical computer with the same number of bits can only be in one of these states at one time.

It is the qubit that makes the quantum computer so powerful. A qubit is a two-state quantum-mechanical system which could be realized by various physical implementations. Such as photons, distinguished by its polarization (horizontal and vertical) or by Fock state (zero-photon state and single-photon state) [MW95]; trapped ions [CZ95], nucleus (NMR) [CFH97], and quantum dots [Ima+99], with spin-up and spin-down as the two states; natural atoms [Blo05], with the two states defined by the lowest two states in its energy level structure. There is another important type of qubits: superconducting qubits [DWM04; Koc+07; Man+09], which is employed in this work and also known as "artificial atom". It is supported by Josephson junctions (which causes the anharmonicity of the energy-ladder), and have many advantages which makes it a very promising candidate for quantum computation in the following aspects.

There are five key requirements called DiVincenzo's criteria [DiV+00] for building a quantum computer. The first one is scalable physical system with well characterized qubits. The superconducting qubits meet this crucial requirement perfectly. As shown in this work, all qubits are printed by a standard fabrication technique on

the surface of a silicon substrate. One could scale it up to an arbitrary number of qubits. It is also outstanding that the characteristic parameters can be designed according to the wishes, and for certain type of superconducting qubits (for example the transmon qubit [Koc+07] employed in this work) the transition frequencies of the superconducting qubits can be varied by changing magnetic field.

The second requirement is the ability to initialize the state of the qubits to a simple fiducial state. It is simple for superconducting qubits, because ones only needs to cool down the chip (with dilution refrigerator for example), and wait for the qubits to relax to the ground states. Due to the cryogenic temperature to maintain superconducting, thermal excitation is also suppressed. The third is long relevant decoherence times. Superconducting qubits have relatively short lifetime(nanosecond to microsecond scale) because of its mesoscopic scale. Nevertheless, there is enough time for thousands of gate-manipulations [DS13]. The fourth is a "universal" set of quantum gates. As for the superconducting qubit, it is achievable to rotate it to any arbitrary position in the Bloch sphere with microwave pulses. Thus one could build the universal set of quantum gates [Nis+07]. The last requirement is a qubit-specific measurement capability. Unlike the nature particles, one does not need to worry about locating the superconducting qubits he wants to manipulate or readout, since they are fixed on the chip. What's more, individual channel for manipulating each qubit could be build on-chip if necessary.

Nowadays, the interaction between the qubits and the readout resonator is of great importance for quantum information research[Bla+04]. The system consisting of one qubit and one readout resonator is well described by the Jaynes-Cummings model[JC63] which was established in the year 1963. And this model was generalized 5 years later to the model named Tavis-Cummings model[TC68] which describes the system of multiple qubits and a mutual resonator.

Multiple controllable two-level systems coupled to a mutual resonator has been employed in many novel applications: for example, the quantum von Neumann architecture [Mar+11], the systems for tunable long-range interaction between distant qubits [Fil+11a; Maj+07a; SPS07], the multi-qubit entanglement created by a collective interaction [RSR07], protection of the system against radiation decay [Fil+11b], and so on. The multifunctionality enables one to develop the potential of Tavis-Cummings systems in the field of quantum computers. An analog quantum simulation [Fey82b; GAN14] for a Dicke model [Dic54] (generalized Tavis-Cummings model) provides the possibility to study the interaction between light and mater in the ultra-strong coupling regime, such as the corresponding eigenenergies and the transient dynamics [Bra+17; Fri+18].

In this thesis, we study the Tavis-Cummings system which consists of a superconducting CPW resonator and 8 transmon qubits whose transition frequencies could be controlled individually. It is a well understood platform to study not only the desired effects but also the parasitic phenomenons in scaled-up quantum systems. Naturally, the more qubits we build in the system, the more complicated it gets, and the more challenging the circuit control is.

In this work, I show full tunability of a quantum register of 8 transmon qubits, and in principle, it could be scaled up to any number of qubits. And the calibration strategy allows for precise local frequency-control up to 6 qubits. When N qubits degenerate with the resonator, a level repulsion of $2g\sqrt{N}$ is expected in the spectrum. In other words, the $\sqrt{N}$ enhancement of the effective coupling strength of a qubit-ensemble to the resonator is a hallmark of Tavis-Cummings model. With the 8-qubit sample studied in this thesis, I am able to bring the transmon qubits one by one into resonance with the resonator, and measure the effective coupling strength. In this way it is proved to be an adequate analog quantum simulator for the Tavis-Cummings model. In previous experimental works, the number of qubits which play a role in the collective behavior is derived after measurement according to the fitting of theoretical model, rather than specified beforehand [Mac+14; Shu+17].

The experiments done in this thesis cover key properties of the system, such as local qubit control, calibration of crosstalk, decoherence, Fano-shaped resonator because of dissipative background, the higher-level transitions of the qubits. All of these are subtle features of any recent physical quantum simulators.

The aim of this thesis is to build up scalable fully-controllable qubit circuits. The approach combines parallel manipulation and readout of multiple qubits using a frequency-division multiplexing scheme, and meanwhile isolates the qubits from the non-corresponding control-components. Hence precise single-qubit manipulation could be done for all qubits. This type of system (multiple qubits manipulated and readout by a mutual resonator bus) could be used for many fields in quantum physics, not only for quantum simulation, but also for computational applications, many-body physics and so on.

The thesis is organized as follows: the fundamental theoretical background of the coplanar waveguide resonator, superconducting Josephson junction, and transmon qubit employed in our work is introduced in Chapter 2. The model of the coupled system and the readout method are discussed as well. Design of the samples including simulation with the generated pattern and the fabrication technique are explained in Chapter 3. Experimental results on the testing single-qubit chip is shown in Chapter 4. In this chapter, measurement on the interested 8-qubits chip

are discussed in details including fitting to the corresponding theoretical model. In Chapter 6 we summarize our work and foresee the potential applications.

2 Circuit QED

2.1 Coplanar waveguide resonator

In the field of Circuit quantum electrodynamics (Circuit QED), both the harmonic oscillator and the 2-level system work in GHz range, i.e. work with microwave. The typical macroscopical device to carry the high-power microwave pulses is coaxial cables. However, it is too bulky for the on-chip design of circuit QED. Instead, distributed element resonator is a perfect candidate. It could be used to couple the photons of microwave signal to the superconducting qubit, to implement qubit readout, and could also work as a quantum bus [Maj+07b] that couples more than one qubit together.

Superconducting micro-scale coplanar waveguide (CPW) resonator [Wen69; Göp+08] is chosen in our work because it has a number of favourable properties compared with other distributed element constructions, such as the micro strip line resonator. The impedance of CPW design is decided by its transverse size, rather than influenced significantly by the property of the substrate. What's more, no requirement of back-side metalization simplifies the fabrication process and protects the elements on the front side.

A conventional CPW structure consists of a single conducting strip (center conductor) accompanied by two pieces of much wider conductors which plays the role of ground plane. The gap from the center conductor to the ground plane on both sides are the same and stay constant along the center strip. All metalization is printed on the same side of the substrate, that's why it is called coplanar.

The illustration of CPW resonator could be found in Fig. 2.1. The length of the center conductor varies from several millimeter to two dozen millimeters, so that the frequency of the fundamental model of the $\lambda/2$ resonator is in GHz range. In the later discussion, introducing a effective permittivity is convenient. According to Ref. [Poz09], a metal layer sandwiched between the substrate and vacuum could
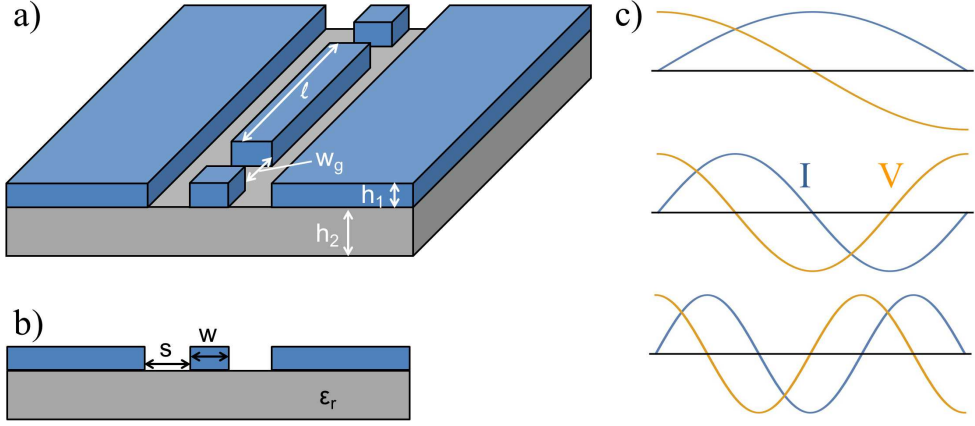
Figure 2.1: (Color online)The coplanar waveguide resonator [Poz09]. a) the 3D figure of the building block of the CPW resonator. The color of metal layer and the substrate are blue and gray respectively. a center superconductor and two accompanied grounding superconductor printed on a substrate. Both sides have the same gap between the center conductor and the grounding conductor. With a break on both ends of the center conductor, it forms a $\lambda/2$ resonator. b) cross-section illustration of CPW resonator corresponding to a). c) The distribution of voltage and current of the resonator. The voltage has antinodes on both ends of the resonator, while the current has nodes.

be represented by the metal layer inside a homogenous dielectric material with the effective permittivity, which is calculated by

$$\epsilon_e = \frac{\epsilon_r + 1}{2} + \frac{\epsilon_r - 1}{2}(1 + 12h_2/w)^{-1/2}, \qquad (2.1)$$

with the dimensions and parameters labeled in Fig. 2.1. ϵ_r is the relative permittivity of the substrate. The type of $\lambda/2$ resonator is chosen in our experiment. That means both ends of the center conductor are floating, as there are gaps at both ends with width w_g, which forms the standing wave of current and voltage inside the center conductor (Fig. 2.1 c) and the created coupling capacitor sets the coupling strength from the resonator to the in and out port. At both of the ends of center conductor the current has a node while the voltage has a antinode. Since the transmon qubits (discussed in Chap. 2.3) are capacitively coupled, for the fundamental model of the resonator, they must sit at the end of the resonator. The fundamental model of the resonator f_0 is straightforward:

$$f_0 = \frac{v_{ph}}{\lambda} = \frac{v_{ph}}{2l}. \qquad (2.2)$$

It corresponds to the wavelength of the fundamental model $\lambda_0 = 2l$. As l is the length of the resonator which must be integer multiples of half wave-length. Thus the higher model of the resonator $f_n = nf_0, n = 2, 3, 4 \ldots$. The phase velocity

$$v_{ph} = \frac{c}{\sqrt{\epsilon_e}}, \tag{2.3}$$

here c is the speed of light in vacuum, and $\sqrt{\epsilon_e}$ is the effective permittivity discussed above. The corresponding propagation constant is then given by

$$\beta = k\sqrt{\epsilon_e}. \tag{2.4}$$

According to Ref. [Göp+08], the capacitance and inductance per unit length C_l and L_l of CPW transmission line is

$$C_l = 4\epsilon_0\epsilon_e \frac{K(k_0)}{K(k_0')}, \tag{2.5}$$

$$L_l = \frac{\mu_0 K(k_0')}{4Kk_0}. \tag{2.6}$$

with K (the complete elliptic integral of the first kind) and arguments

$$k_0 = \frac{w}{w + 2s}, \tag{2.7}$$

$$k_0' = \sqrt{1 - k_0^2}. \tag{2.8}$$

Here w and s are the center conductor width and the gap width of the CPW respectively(See Fig. 2.1 b). One notices that C_l is determined by the geometry of the CPW resonator and effective permittivity ϵ_e, on the other hand, L_l is determined by the geometry only. The characteristic impedance of the CPW which is defined by the ratio of maximum voltage and current is calculated by

$$Z_0 = \sqrt{\frac{L_l}{C_l}}. \tag{2.9}$$

It is noteworthy that as discussed in Ref. [Sim04], the structure of the CPW is not with random value, but with the layout that results in the Z_0 getting close to 50Ω, because it is the standard impedance for all the electronic equipment used in measurement. For our work, the center conductor width $w = 6.6\mu m$ and the gap width $s = 6.6\mu m$ are chosen. The substrate is pure silicon with thickness of $300\mu m$ and relative permittivity $\epsilon_r = 11.6$. The design and measurement will be shown in Chap. 3.
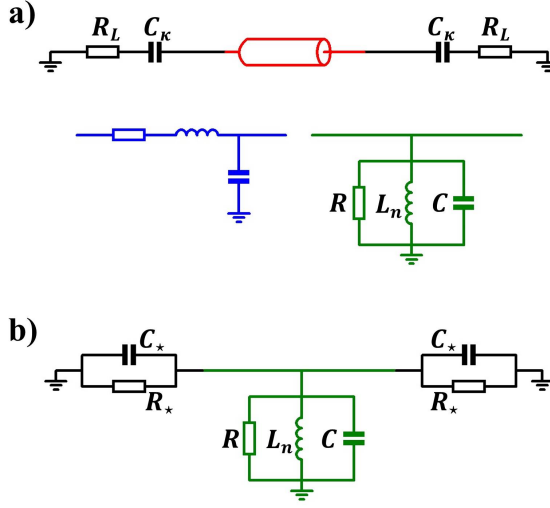
Figure 2.2: (Color online)The equivalent circuit diagram of CPW resonator. a) The resonator (red) is coupled to the input and output ports through a coupling capacitance and a serial loading resistor. The resonator could be replaced by distributed elements (blue). Around resonance, the resonator could be represented by a lumped-element RLC oscillator (shown in green). b) The coupling capacitance C_κ and serial loading resistor R_L are transformed to parallel capacitor and resistor according to Norton theorem to analyze their function.

The transmission line resonator could be presented by a parallel RLC oscillator [Göp+08] around its resonant frequency. The circuit diagram and corresponding parameters are shown in Fig. 2.2 (a). The impedance of the RLC oscillator is

$$Z_{RLC} = \left(\frac{1}{R} + \frac{1}{i\omega L_n} + i\omega C \right)^{-1}. \tag{2.10}$$

When the angular frequency ω approximates ω_n, where $\omega_n = 1/\sqrt{L_n C}$ is the angular frequency of the n_{th} mode,

$$Z_{RLC} \approx \frac{R}{1 + 2iRC(\omega - \omega_n)}, \tag{2.11}$$

with arguments

$$R = \frac{Z_0}{l\alpha}, \tag{2.12}$$

$$L_n = \frac{2L_l l}{n^2 \pi^2}, \tag{2.13}$$

$$C = \frac{C_l l}{2}, \tag{2.14}$$

where α is the attenuation constant. The coupling capacitance C_κ and serial loading resistor R_L (see Fig. 2.2 (a)) could be transformed to parallel capacitor $C_\star$ and resistor $R_\star$ according to Norton theorem to analyze their function (see Fig. 2.2 (b), and Ref. [Göp+08])

$$C_\star = \frac{C_\kappa}{1 + (\omega_n C_\kappa R_L)^2},\tag{2.15}$$

$$R_\star = \frac{1 + (\omega_n C_\kappa R_L)^2}{(\omega_n C_\kappa R_L)^2}.\tag{2.16}$$

Here R_L has a standard value of 50Ω, and C_κ could be obtained by simulation of the real geometry which will be discussed below.

Approximating CPW resonator to a RLC oscillator is convenient to characterize the resonator. For example the quality factor (i.e. Q factor), a crucial parameter which describes how fast the energy is lost of the resonator. The Q factor is defined by [Poz09]

$$Q = \omega_r \frac{average\ energy\ stored}{power\ loss}.\tag{2.17}$$

The internal Q factor Q_i is the quality factor of the resonator itself only. But an additional circuit coupled to the resonator is always needed to manipulate it, which cause addition loss corresponding to the coupling Q factor Q_c. Thus, the total Q factor of the coupled system is named as loaded quality factor Q_L, and the relation between these Q factors are

$$Q_L^{-1} = Q_c^{-1} + Q_i^{-1}.\tag{2.18}$$

The loaded Q factor corresponding to the symmetric Norton equivalent circuit is calculated by

$$Q_L = \omega_n^\star \frac{C + 2C_\star}{R^{-1} + 2R_\star^{-1}},\tag{2.19}$$

where

$$\omega_n^\star = 1/\sqrt{L_n(C + 2C_\star)}\tag{2.20}$$

is the shifted resonator angular frequency. For $C_\star \ll C$, the shift of the resonator is negligible, Q_i and Q_c could be calculated by

$$Q_i = \omega_n RC,\tag{2.21}$$

$$Q_c = \frac{\omega_n R_\star C}{2}.\tag{2.22}$$

2.2 Superconductivity and Josephson junction

2.2.1 Superconductivity

Exact zero electrical resistance was first found by H. K. Onnes [Onn11] in 1911 during the investigation on mercury at low temperature, which led to the production of liquid helium. The next milestone is the observation of complete expelling of magnetic flux fields in superconductors when cooled below their critical temperature, by W. Meissner and R. Ochsenfeld [MO33] in 1933.

There was no microscopic theoretical explanation of superconductivity until the year 1957, in which the BCS theory [BCS57] was proposed by J. Bardeen, L. Cooper and J. R. Schrieffer. According to their theory, particle called Cooper pair is formed by a pair of electrons with opposite spin and momentum because of a weak photon-induced attraction. Since the Cooper pairs have zero total spin and momentum, they obey the Bose-Einstein statistics [Bos24], and all condense to the lowest energy state at low temperature. The coupling between the pair of electrons of the Cooper pair also results in the energy gap Δ between the ground state (which is occupied by the Cooper pairs) and the excited states of the single electrons (which are called quasi-particles). This finite energy gap also explains the perfect conductivity of superconductors, because the scattering is inhibited. The quantization of flux [DF61; DN61] proofs that inside superconductor, the carriers of charge are Cooper pairs rather than single electrons which means the superconducting current in a closed loop is only able to create the flux of integer multiples of the flux quantum $\Phi_0 = h/2e$, where e is the electron charge and h is Planck constant.

In the year 1950, V. L. Ginzburg and L. D. Landau developed Ginzburg-Landau theory to describe superconductors without examining the microscopic properties [Tin04]. The wave function corresponding to macroscopic superconducting state is

$$\Psi(\vec{r}, t) = |\Psi(\vec{r}, t)| e^{i\theta(\vec{r}, t)}, \tag{2.23}$$

where the amplitude $|\Psi(\vec{r}, t)|$ corresponds to the Cooper pair density, and $\theta(\vec{r}, t)$ is the phase. There after, superconductivity was treated as a macroscopic quantum effect based on the behavior of the Cooper pairs in the superconductor.

2.2.2 Josephson Junction

A Josephson junction [Jos62] is a device consists of two superconductors connected by a thin layer insulator. The amplitude of the wave function remains constant

inside a bulky superconductor and decays exponentially exceeding the edge (see Fig. 2.3). However, if the insulator is thin enough, the wave function of one side is still non-negligible on the other side of the barrier, which means that the Cooper pairs are able to tunnel through the barrier to the other side. In the year 1962, B. D. Josephson developed two relations to describe the physics of Josephson junction [Jos62]: the superconducting phase evolution equation and weak-link current-phase relation, which are in the following form:

$$U(t) = \frac{\hbar}{2e} \frac{\partial \varphi}{\partial t}$$
$$I(t) = I_c \sin(\varphi t), \tag{2.24}$$

These two relations indicate as long as the constant supercurrent floating through the junction is no larger than the critical current, there is no voltage through the junction. If the supercurrent (or the phase) changes, the voltage through the junction depends on the time evolution of the phase.
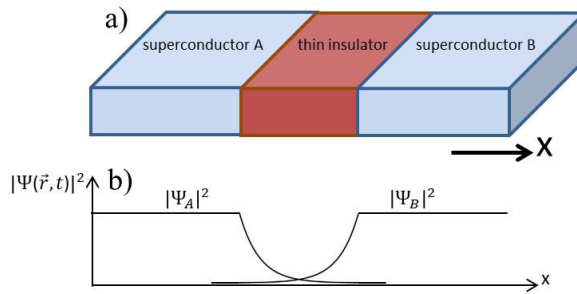
Figure 2.3: (Color online)The Josephson junction [Lis03]. (a) illustrates the building block of the Josephson Junction: two bulky superconductors separated by a thin layer of insulator. (b) shows the curve of the amplitude corresponds to the Cooper pair density. Inside the thin insulator, there is overlap between the 2 exponentially-decayed wavefunctions, which permits the interaction between the 2 superconductors.

2.3 Transmon qubit

In the past few decades, qubit based on superconducting Josephson junction has developed enormously. Because of its excellent scalability, controllability and well-established fabrication technique, superconducting qubit is considered as a promising candidate for quantum computing. It evolves from typical charge qubit [Bou+98], flux qubit [Moo+99; Chi+03] and phase qubit [Mar09], to more

complicated superconducting qubits, such as transmon qubit [Koc+07], Xmon qubit [Bar+13], fluxonium qubit [Man+09] and so on.

The qubit employed in this work is transmission-line shunted plasma oscillation qubit, namely transmon qubit. It is originated from the Cooper pair box (CPB) qubit, however works in a totally different region of the proportion of the Josephson energy (E_J) and charging energy (E_C), where $EJ \gg E_C$. The schematic diagram and equivalent circuit diagram are shown in Fig. 2.4. The red part in Fig. 2.4 (a) is the inter digital capacitance that creates the large shunting capacitance which corresponds to C_s in Fig. 2.4 (b). The two black crosses represent the Josephson junctions. The length of the upper and lower capacitors coupled to the center conductor and the ground respectively are varied, in order to change the effective coupling capacitance. The Hamiltonian of transmon is the same with the CPB qubit, which reads as [Koc+07]

$$\hat{H} = 4E_C(\hat{n} - n_g)^2 - E_J \cos \hat{\varphi}. \tag{2.25}$$

The decisive difference of transmon from the CPB system is the relatively large shunting capacitance (Cs), which therefor reduces the charging energy $E_C = e^2/2C_{total}$ ($C_{total} = C_g + Cs + C_J$), so that enhances the E_J/E_C ratio. The large E_J/E_C ratio reduces the sensitivity of charge noise, while sacrifices the anharmonicity of the energy level. However, that's worthwhile since the anharmonicity drops algebraically while the sensitivity decreases exponentially in E_J/E_C. The potential of transmon is cosine type because the term containing E_J plays the main role of the system. By expanding this term to the $4th$ order around $\varphi = 0$, and then treat the quartic term in the leading order perturbation theory, the eigenenergies inside the cosine potential are derived:

$$E_m \simeq -E_J + \sqrt{8E_J E_C}(m + \frac{1}{2}) - \frac{E_C}{12}(6m^2 + 6m + 3), \tag{2.26}$$

where m is the m_{th} level, and $\sqrt{8E_J E_C}/\hbar$ is the Josephson plasma frequency. The transition frequency between the ground state and the first excited state is

$$\begin{aligned} f_{01} &= \frac{E_{01}}{h} = \frac{E_1 - E_0}{h} \\ &= \frac{\sqrt{8E_J E_C} - E_C}{h}. \end{aligned} \tag{2.27}$$

The absolute anharmonicity is defined to be $\alpha \equiv E_{12} - E_{01}$, and the relative anharmonicity is $\alpha_r \equiv \alpha/E_{01}$. According to the eigenenergies in Eq. 2.26, one obtains

$$\begin{aligned} \alpha &\simeq -E_C, \\ \alpha_r &\simeq -\sqrt{E_C/8E_J}. \end{aligned} \tag{2.28}$$
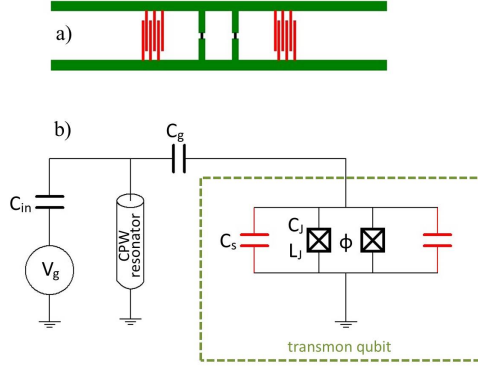
Figure 2.4: (Color online)Layout of the transmon qubit. (a) is schematic diagram of transmon qubit. the red part is the inter digital capacitance that creates the large shunting capacitance (C_s in figure b). The two black crosses represent 2 Josephson junctions. The upper and lower capacitors coupled to the center conductor and the ground respectively are varied to vary the effective coupling capacitance. (b) shows the equivalent circuit diagram of transmon coupled to a CPW resonator. The 2 Josephson junctions form a SQUID loop. By manipulating the flux penetrating this loop, one is able to control the transition frequency between the eigenstates of the transmon.

2.4 Theoretical model of qubits coupling to a harmonic oscillator

2.4.1 Jaynes-Cummings model

In the year 1963, E. T. Jaynes and F. W. Cummings built the most fundamental theoretical model to describe a single atom interacting with a harmonic cavity [JC63]. Under the rotating wave approximation which eliminate the energy non-conservation terms in the interaction Hamiltonian, the Hamiltonian of this model is known as:

$$\hat{H} = \hbar\omega_c(\hat{a}^\dagger\hat{a} + \frac{1}{2}) + \frac{\hbar\omega_a}{2}\hat{\sigma}_z + \hbar g_0(\hat{a}\sigma^+ + \hat{a}^\dagger\sigma^-), \qquad (2.29)$$

where ω_c and ω_a are the frequencies of the cavity and the atom respectively, and g_0 is the coupling strength between them. This Hamiltonian could be solved analytically. Define detuning $\Delta = \omega_a - \omega_c$. In the basis $|g, n+1\rangle, |e, n\rangle$ (n is the photon number in the resonator, and $|g\rangle, |e\rangle$ denotes the uncoupled ground state and excited states respectively), one obtains the eigenenergies

$$
\begin{aligned}
E_{\pm,n} &= (n+1)\hbar\omega_c \pm \frac{\hbar}{2}\sqrt{4g_0^2(n+1) + \Delta^2}, \\
E_{g,0} &= -\frac{\hbar\Delta}{2}.
\end{aligned}
\qquad (2.30)
$$

and correspond dressed states

$$
\begin{aligned}
|+, n\rangle &= \cos\theta|e, n\rangle + \sin\theta|g, n+1\rangle, \\
|-, n\rangle &= -\sin\theta|e, n\rangle + \cos\theta|g, n+1\rangle, \\
\text{ground state} &= |g, 0\rangle,
\end{aligned}
\tag{2.31}
$$

where

$$
\theta = \frac{1}{2}\arctan\left(\frac{2g_0\sqrt{n+1}}{\Delta}\right)
\tag{2.32}
$$

Two important opposite conditions of the coupled system are discussed in the following subsections: zero detuning and dispersive limit. At zero detuning the system gets to an maximally entangled state, and dispersive limit is very useful for qubit measurement.

2.4.2 Zero detuning

In Circuit QED, the atom is represented by the superconducting qubit, and the cavity by a on-chip distributed elements resonator (in our case, a $\lambda/2$ CPW resonator). However, the Hamiltonian remains similar to Eq. 2.29. In the zero detuning case, i.e. the detuning between the qubit and the resonator $\Delta = 0$ (from now on, the frequency ω_a and ω_c are replaced by ω_q and ω_r respectively). The energy-level scheme of the uncoupled system is depicted in Fig. 2.5 by the colorized lines on the two sides, and the eigenenergies of the dressed states are represented by the black line in the middle. The eigenenergies of Eq. 2.30 are reduced to

$$
\begin{aligned}
E_{\pm, n} &= (n+1)\hbar\omega_r \pm \hbar g_0\sqrt{(n+1)}, \\
E_{g, 0} &= 0.
\end{aligned}
\tag{2.33}
$$

The vacuum Rabi splitting for a pair of dressed states $|\pm, n\rangle$ reaches its minimum value

$$
\Delta E_n = 2\hbar g_0\sqrt{n+1}.
\tag{2.34}
$$

The angel θ defined by Eq. 2.32 is equal to $\pi/2$. Thus, the eigenstates reduce to the maximally entangled states (except for the ground state)

$$
\begin{aligned}
|+, n\rangle &= \frac{1}{\sqrt{2}}|e, n\rangle + \frac{1}{\sqrt{2}}|g, n+1\rangle, \\
|-, n\rangle &= -\frac{1}{\sqrt{2}}|e, n\rangle + \frac{1}{\sqrt{2}}|g, n+1\rangle.
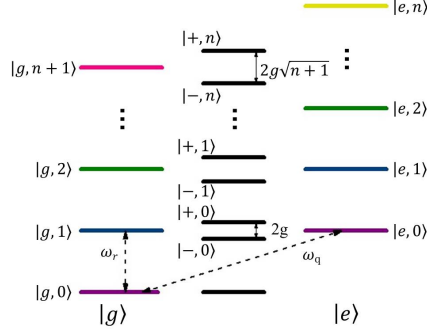\end{aligned}
\tag{2.35}
$$

Figure 2.5: (Color online)Energy level scheme of single 2-level qubit interacting with a resonator in the zero detuning case. The energy levels of the uncoupled system is depicted by the colorized lines on the two sides, and the eigenenergies of the dressed states are represented by the black line in the middle. For dressed states, the energy level difference (vacuum Rabi splitting) between a pair of the dressed states scales up with $\sqrt{n}$.

2.4.3 Dispersive limit

The goal of Circuit QED is to coherently control and readout the superconducting qubit. It has been illustrated that in the dispersive limit, it is probable to operate and readout a transmon qubit through the coupled resonator [Koc+07]. Operating the qubit is simply done by sending a microwave pulse through, while readout is realized by measuring the shift of the phase or amplitude of the microwave field transmitted (or reflected) by the resonator.

The dispersive limit means the detuning between the qubit and the resonator Δ is very large compared to the corresponding coupling strength, namely $g_0/|\Delta| \ll 1$. Employing a unitary operator

$$\hat{U} = exp\left[\beta_0(a\sigma^+ - a^\dagger\sigma^-)\right],\tag{2.36}$$

where $\beta_0 = g_0/\Delta$. And making the canonical transform $\hat{U}\hat{H}\hat{U}^\dagger$ on the Hamiltonian of Eq. 2.29. The interaction term is eliminated to the lowest order in β_0, so that the following effective Hamiltonian is obtained:

$$\hat{H}_{eff} = \hbar(\omega_r + \frac{g_0^2}{\Delta}\hat{\sigma}_z)\hat{a}^\dagger\hat{a} + \frac{\hbar}{2}(\omega_q + \frac{g_0^2}{\Delta})\hat{\sigma}_z.\tag{2.37}$$

By defining the dispersive shift

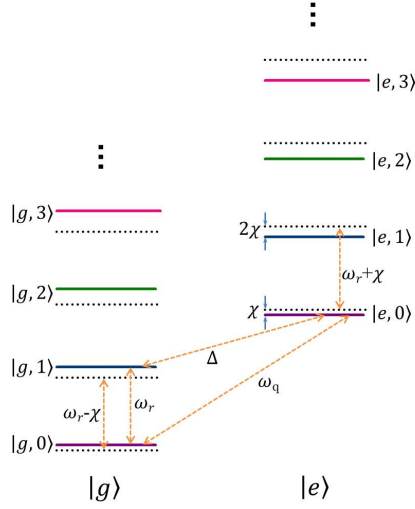$$\chi_0 = \frac{g_0^2}{\Delta},\tag{2.38}$$

Figure 2.6: (Color online)Energy levels of Jaynes-Cummings model under dispersive limit. The qubit frequency is renormalized by the dispersive shift. The resonator transition frequency depends on the state of the qubit.

the effective Hamiltonian is rewritten as

$$\hat{H}_e = \hbar(\omega_r + \chi_0 \hat{\sigma}_z)\hat{a}^\dagger \hat{a} + \frac{\hbar}{2}(\omega_q + \chi_0)\hat{\sigma}_z. \tag{2.39}$$

One notices that the transition frequency of the qubit is shifted by χ_0 because of the interaction. More interestingly, the frequency of the resonator now depends on the state of the qubit. If the qubit is at the ground state, the resonator is shifted down to $\omega_r - \chi_0$, to the contrary, the resonator shifts up in frequency to $\omega_r + \chi_0$. Thus, by measuring the shift of the resonator, the state of the qubit could be deduced. The energy-level scheme in dispersive limit is shown in Fig. 2.6.

2.4.4 Jaynes-Cummings model for Transmon qubit

The difference between natural atom and the transmon qubit which is used in our work is that the anharmonicity of the atom is much larger, so that the higher energy levels are ignored, only the first two states work. To the contrary, due to relatively small anharmonicity, higher levels of transmons should also be taken into account in the theoretical model for transmon qubit coupled to resonator. The energy ladder

scheme of a transmon coupled to a resonator is shown in Fig. 2.7. Thus, in the basis of the non-coupled transmon states $|i\rangle$, by generalizing Eq. 2.29,Jaynes-Cummings Hamiltonian of the system consists of one transmon qubit and one resonator is obtained [Koc+07]

$$\hat{H} = \hbar\omega_r\hat{a}^\dagger\hat{a} + \hbar\sum_i \omega_i|i\rangle\langle i| + \hbar\sum_{i,j} g_{i,j}|i\rangle\langle j|(\hat{a} + \hat{a}^\dagger). \tag{2.40}$$

The coupling energy

$$g_{i,j} = 2\beta eV_{rms}^0\langle i|\hat{n}|j\rangle/\hbar, \tag{2.41}$$

where $V_{rms}^0 = \sqrt{\frac{\hbar\omega_r}{2C_r}}$, $\beta = C_g/C_{total}$, and $\hat{n}$ denotes the Cooper pair number operator of the transmon, and has the following form

$$\hat{n} = -i\sqrt[4]{\frac{E_J}{32E_C}}(\hat{b} - \hat{b}^\dagger). \tag{2.42}$$

Under the condition $E_J \gg E_C$, the term $\langle j+k|\hat{n}|j\rangle$ ($|k| > 1$) tends to zero. This means only the coupling between adjacent energy levels of the transmon play the dominating role. Getting rid of the nonadjacent-level coupling terms and apply the rotating wave approximation likewise, one derives the effective Jaynes-Cummings Hamiltonian for transmon interacting with a harmonic oscillator

$$\hat{H}_{eff} = \hbar\omega_r\hat{a}^\dagger\hat{a} + \hbar\sum_j \omega_j|j\rangle\langle j| + \hbar\sum_j (g_{j,j+1}|j\rangle\langle j+1|\hat{a}^\dagger + H.c.). \tag{2.43}$$

This Hamiltonian is block-diagonal and does not have an analytical solution. In spite of this, under the dispersive condition (discussed below), the according Hamiltonian could be solved analytically.

To readout the transmon qubit, as discussed in the last section, the coupled system should work in the dispersive limit. Defining the detuning between the transmon and resonator as $\Delta_{i,i+1} = \omega_{i,i+1} - \omega_r$, dispersive limits means $\Delta_{i,i+1} \gg g_{i,i+1}$, especially $\Delta_{0,1} \gg g_{0,1}$. Employing a unitary operator

$$\hat{U} = exp\left[\sum_i \beta_{i,i+1}(\hat{a}|i+1\rangle\langle i| - \hat{a}^\dagger|i\rangle\langle i+1|)\right], \tag{2.44}$$

where $\beta_{i,i+1} = g_{i,i+1}/\Delta_{i,i+1}$. And making the canonical transform $\hat{U}\hat{H}\hat{U}^\dagger$ on the Hamiltonian of Eq. 2.40, the interaction term is eliminated to the lowest order in $\beta_{i,i+1}$. Keeping in mind that the virtual transitions by the excited states is allowed due to the relatively small anharmonicity, and restricting the Hilbert space to the first 2 states of the transmon, the following effective Hamiltonian is obtained:

$$\hat{H}_{eff} = \frac{\hbar}{2}(\omega_{01} + \chi)\hat{\sigma}_z + \hbar(\omega_r - \frac{\chi_{12}}{2} + \chi\hat{\sigma}_z)\hat{a}^\dagger\hat{a}. \tag{2.45}$$
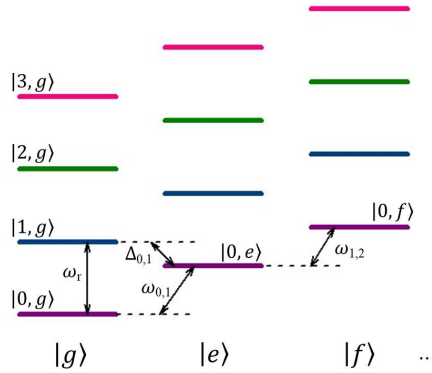
Figure 2.7: (Color online)Energy level scheme of a transmon qubit coupled to a resonator [Koc+07]. States $|g\rangle$, $|e\rangle$, $|f\rangle$ denote the ground state, first excited state and the second excited state of the transmon respectively. The number in the coupled sates (for example $|0,g\rangle$) stands for the photon number of the resonator. $\Delta_{0,1}$ is the detuning between the frequency of the resonator and the transition frequency of the qubit.

The dispersive shift $\chi = \chi_{01} - \frac{\chi_{12}}{2}$, where

$$\chi_{ij} = g_{ij}^2 / (\omega_{ij} - \omega_r). \tag{2.46}$$

One notices that not only the transition frequency of the qubit is shifted because of the interaction. More importantly, the frequency of the resonator is renormalized based on the qubit state. If the qubit is on the ground state, the renormalized resonator frequency $\omega_r^- = \omega_r - \chi_{01}$, while on the contrary, $\omega_r^+ = \omega_r + \chi_{01} - \chi_{12}$. Thus, by measuring the frequency of the resonator, the state of the qubit is deduced (shown in Fig. 2.8). Moreover, higher level transition of the qubit is also observed and distinguishable by spectroscopically measure the shift of resonance frequency of the resonator, as the higher the transition level is, the more the resonator is shifted.

2.4.5 Tavis-Cummings model

The Tavis-Cummings model was introduced 5 years later than the Jaynes-Cummings model, by M. Tavis and F. W. Cummings to describe multiple two-level system coupled to a single resonator [TC68]. It is of more interest, because single qubit is not enough to build a system that is able to perform quantum computing or quantum
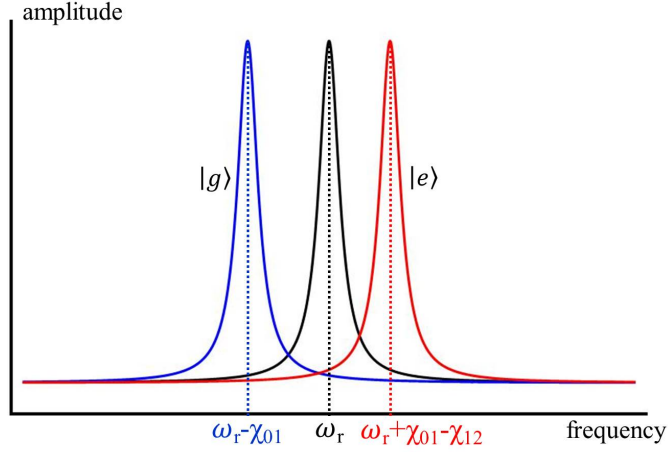
Figure 2.8: (Color online)Dispersive readout scheme of the transmon qubit. The transmission frequency of the resonator depends on the coupled transmon qubit state. To measure the qubit state, one point on the frequency that is sensitive to the resonator shift is picked out. By observing the change on the amplitude of this point, one deduces the state of the qubit.

simulation. For multiple atoms coupled to a cavity, analogous to Eq. 2.29, neglect the interaction between the atoms, the Hamiltonian of Tavis-Cummings model is

$$\hat{H} = \hbar\omega_c\hat{a}^\dagger\hat{a} + \hbar\sum_{i=1}^{N}\left(\frac{\omega_i}{2}\hat{\sigma}_i^z + g_i(\hat{a}\sigma_i^+ + \hat{a}^\dagger\sigma_i^-)\right), \qquad (2.47)$$

where i denote the i_{th} qubit, and N is the total number of the qubits.

Converting it into the system I study, based on Eq.2.43, I obtain the effective Hamiltonian:

$$\hat{H} = \hbar\omega_r\hat{a}^\dagger\hat{a} + \hbar\sum_{i=1}^{N}\sum_{j}\left(\omega_{i_j}|j\rangle\langle j| + (g_{i_{j,j+1}}|j\rangle\langle j+1|\hat{a}^\dagger + H.c.)\right), \qquad (2.48)$$

where i denotes the i_{th} qubit and j denotes the j_{th} level of that qubit. In the later chapters about the experiment, one notices that when the power of the driving field for the transmon qubits are small enough, only the transition between the lowest 2 levels are excited, the higher the power, the more higher levels are visible.

3 Sample design and fabrication

The pattern of our sample is designed employing one of the Tanner softwares called L-Edit, which is very convenient to build models (named T-cell) of different components, and adjust the geometry automatically. Fig. 3.1 shows the window of 1-qubit-chip designing. The multicolored structure is because that the design is covered by multiple layers. The final pattern (see Fig. 3.2) is generated in the form of GDS file by boolean derivation of the layers. Thus, for different fabrication procedure, the corresponding layout could be generated separately applying different algorithm.

The complete layout of the Circuit QED system studied in this work is illustrated in Fig. 3.2. The single-transmon chip depicted in figure (a) is designed to do the test on the quality of the Josephson junction, transmon qubit and the resonator. The big pink meander structure is the CPW resonator. The transmon qubit is the small block at the left end of the resonator with violet color. The long "U-shape" pink structure on top of the qubit is the flux bias line that connected to DC current source. The nine large violet structure with 4 square paddle for each are the test Josephson junctions which could be measured by the 4-point probe station. The most interesting 8-qubit sample is shown by figure (b), which has the same design as figure (a), only with more qubits and flux bias lines, and fabricated at the same time with the single-qubit chip.

In this chapter I talk about how the CPW resonator and the transmon qubit are designed and fabricated. The layout is printed onto a intrinsic silicon substrate which has large internal quality factor. The material of superconductor is chosen to be aluminum due to its high performance for high Q resonator and well-established fabrication process for Josephson junction.

3.1 Design of the CPW resonator

3.1.1 Geometry of the resonator

Fig. 3.2 (c) shows the layout of our meandered $\lambda/2$ CPW resonator. The three insets show the zoom-in of the coupling gap to input/output ports(blue), the meandered
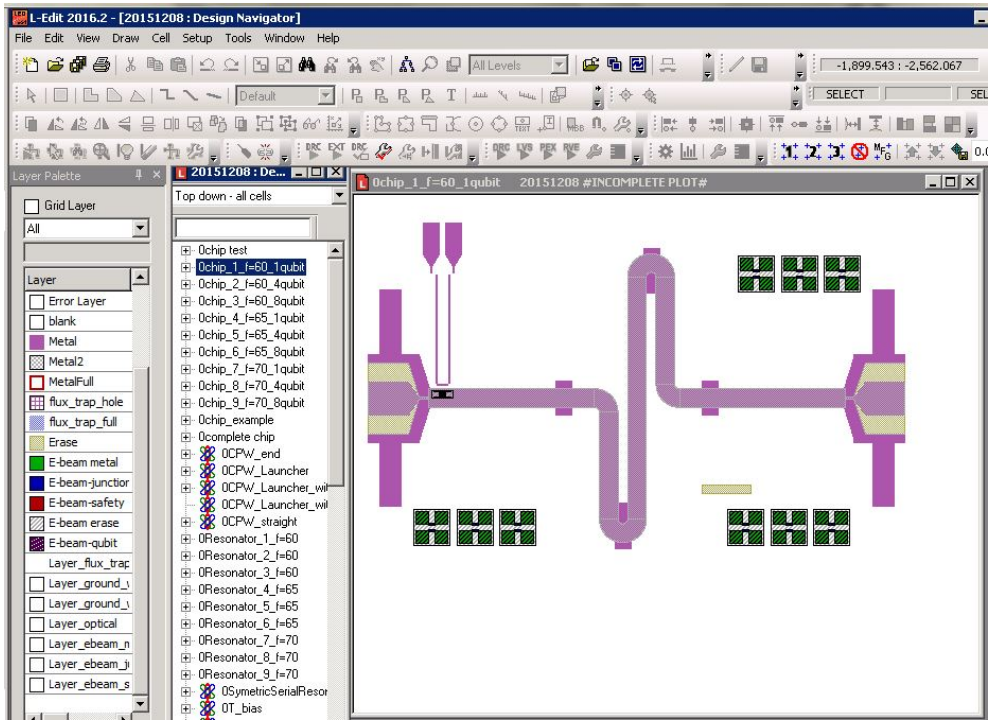
Figure 3.1: (Color online)Design of the sample employing L-Edit. Different layers are indicated by different colors. The final pattern is generated in the form of GDS file by boolean derivation of the layers. Thus, for different fabrication procedure, the corresponding layout could be generated separately applying different algorithm.

structure (green) which reduce the size of the chip, and the slots for transmon qubits (black). Corresponding to Fig. 2.1, the center conductor width $w = 10\mu m$ is chosen. The thickness of intrinsic silicon substrate is $h_2 = 300\mu m$ with relative permittivity $\epsilon_r = 11.6$. According to Eq. 2.1, the effective permittivity is calculated to be $\epsilon_r \approx 6.6$. As discussed in the last chapter, the ratio $k_0 = w/(w + 2s)$ defines the capacitance and inductance per unit length C_l and L_l, which in turn determines the characteristic impedance Z_0. The gap s between the center conductor is not chosen randomly, it should meet $Z_0 \approx 50\Omega$, which matches the industrial standard for all equipment and the coaxial cables. As a result, the gap of 6.0 μm is chosen. The characteristic parameters of the resonator are calculated to be $C_l = 159.9\ pF$ (Eq. 2.5), $L_l = 438.5\ nH$ (Eq. 2.6) and $Z_0 = 50.6\ \Omega$ (Eq. 2.9).

Considering the technical limitation of the measurement setup which I discuss later and the transition frequency of qubits I want to measure, the fundamental frequency
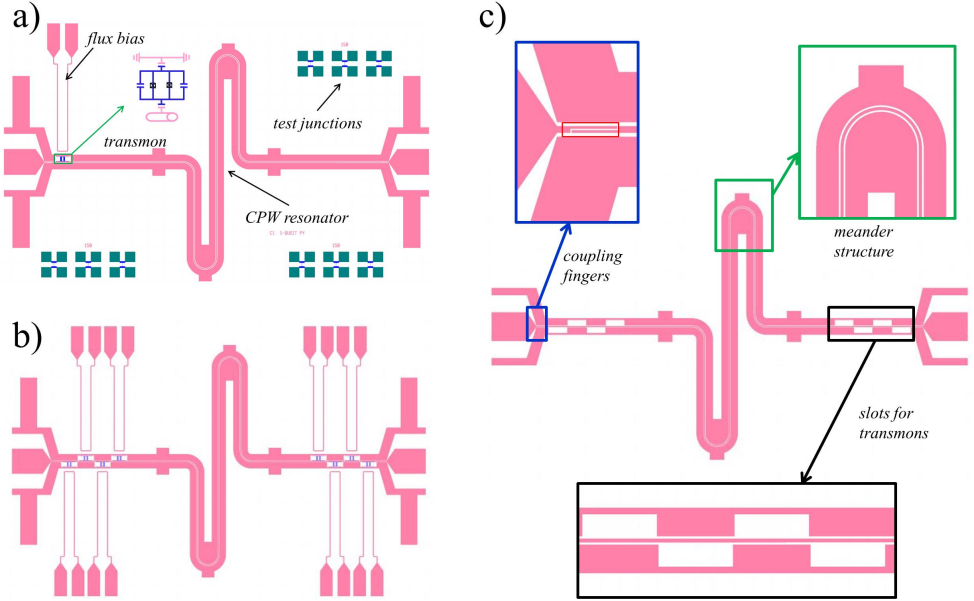
Figure 3.2: (Color online)Layout of the sample. (a) The sample with only 1 qubit coupled to the CPW resonator. The big pink meander structure is the CPW resonator. The transmon qubit is the small "I-shape" component at the left end of the resonator with violet color. The long "U-shape" pink structure on top of the qubit is the flux bias line that connected to DC current source. The nine large violet structure with 4 square paddle for each are the test Josephson junctions which could be measured by the 4-point probe station. (b) The same design as illustrated in figure a, only with more qubits and flux bias lines. (c) Layout of the CPW resonator only. The three insets show the zoom-in of the coupling gap to input/output ports (blue), the meander structure (green) which reduce the size of the chip, and the slots for transmon qubits (black).

of resonator at 7.0 GHz is targeted. The corresponding length of the resonator could be calculated [Göp+08]

$$l = \frac{v_{ph}}{2f_0} = \frac{c}{\sqrt{\epsilon_e}} \frac{1}{2f_0}. \tag{3.1}$$

Plugging in the numbers into this equation, the length of 8.349 *mm* of the fundamental mode is obtained. It is worth noticing that, the angular frequency of the resonator is not exactly 7 GHz, but shifted downwards due to the coupling to the readout components. A more accurate frequency could be calculated by Eq. 2.20, which considers not only the resonator's capacitance, but also the effective capacitance of coupling to readout ports.

3.1.2 Coupling to the readout ports and quality factor determination

The coupling capacitance

The capacitor C_κ created by the gap at both ends of the resonator to the input and output ports is a crucial parameter of the resonator. It determines the coupling strength of the resonator to its readout ports, thus decides the coupling quality factor and the loaded quality factor as well. By adjusting the coupling finger length (or the gap) shown in the inset with blue frame in Fig. 3.2 (c), C_κ could be varied. A targeted loaded quality factor $Q_L = 5000$ is suitable, as it is neither too low which makes the resonator very lossy, nor too high which results in a too small bandwidth of the resonator, making it inappropriate for qubit-readout. According to our design, C_κ should be around 5.6 fF. Based on this value, the loaded quality factor is calculated to be $Q = 4945$ according to Eq. 2.19.

How to get the value of the coupling capacitor of the designed geometry? A convenient software named Sonnet is employed (see Fig. 3.3). The box wall is acquiescently grounded (black frame shown in Fig. 3.3 (a). Two ports are placed on the wall and linked to the 2 coupling fingers. Running the simulation within a self-defined broad frequency range, one is able to view the result by the response viewer. Adding the equation curve to the graph named "Capacitance2" which gives the capacitance between any pair of ports, the capacitance is obtained (shown in Fig. 3.3 (b)-(d). Although it looks undulant, actually the range is rather tiny (within the range of ± 0.002 fF). The longer the fingers, the larger the coupling to the input/output ports. The finger length in (b), (c) and (d) are 60 μm, 70 μm and 80 μm respectively. According to the result, a length of 70 μm suits the target the best.

Scattering matrix of 2-port network

As long as the length of coupling finger is decided, the next step is to study the propagation behavior of the coupled resonator before fabrication. To determine the scattering character of the resonator, a commonly-used presentation named two-port network [Poz09] (see Fig. 3.4) is employed and could be measured experimentally by a vector network analyzer (VNA) and simulatively by a Sonnet project including the whole geometry of the CPW resonator. The characterization is given by the scattering matrix, where one considers the voltages and currents for the 2 ports. The
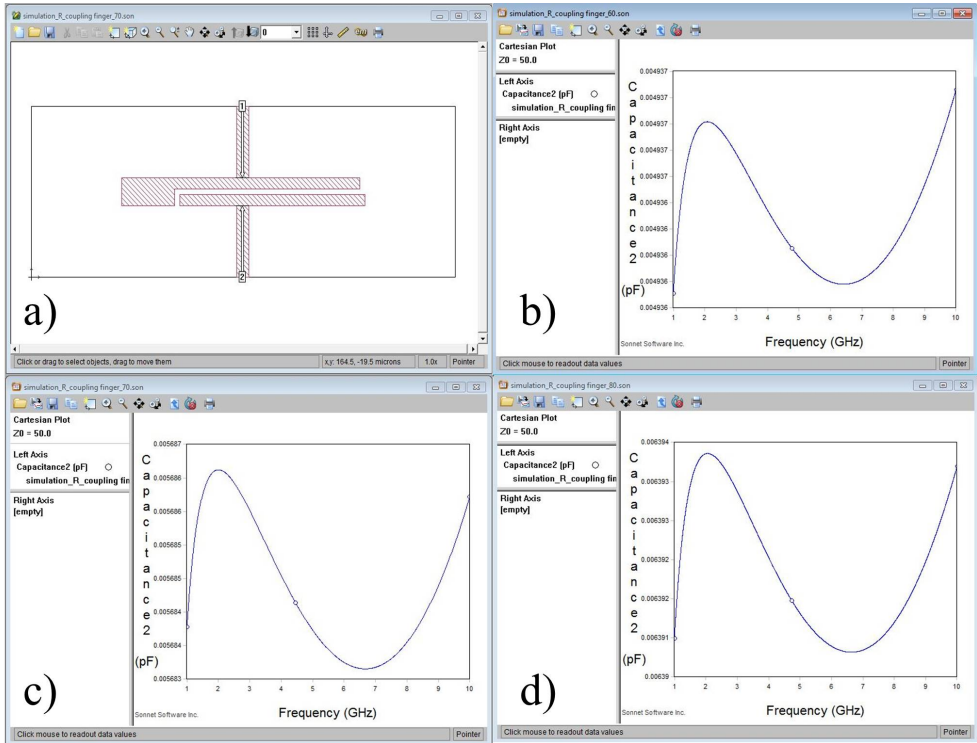
Figure 3.3: (Color online)The Sonnet project which simulates the capacitance C_κ. (a) The project that 2 ports are placed on the wall and linked to the 2 coupling fingers.(b)-(d) give the result of coupling finger length of 60 μm, 70 μm and 80 μm respectively. In the response viewer, adding the equation curve to the graph named "Capacitance2" which gives the capacitance between any pair of ports, the capacitance is obtained. Although the curve looks undulant, actually the range is rather tiny (within the range of ± 0.002 fF). The longer the fingers, the larger the coupling to the input/output ports. According to the result, finger length of 70 μm suits the target the best.

incident and reflected waves of voltage of the network is related by the scattering matrix

$$\begin{pmatrix} V_1^- \\ V_2^- \end{pmatrix} = \begin{pmatrix} S_{11} & S_{12} \\ S_{21} & S_{22} \end{pmatrix} \begin{pmatrix} V_1^+ \\ V_2^+ \end{pmatrix}, \tag{3.2}$$

where V_1^+ is the incident voltage wave into port 1 of the network, while V_1^- is the reflected voltage wave. S_{12} is the wave generated by port 1 of the VNA which received by port 2 of the VNA, S_{11} is the wave generated by port 1 of the VNA which received by itself.
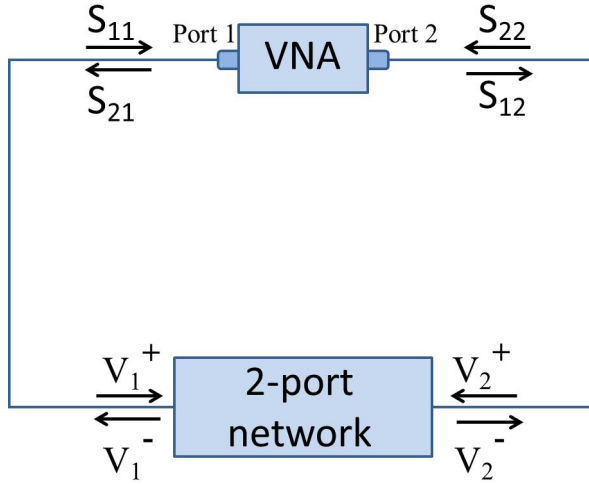
Figure 3.4: (Color online)Two-port network measured by a vector network analyzer (VNA). Microwave signal is usually generated by port 1 of the VNA. the incident and reflected voltage wave of both ports of the 2-port network is measured. The scattering characters are illustrated by the scattering matrix.

For a usual measurement, microwave generated from one port of the VNA is enough, normally port 1 is chosen. So that the scattering matrix in Eq. 3.2 reduces to

$$\begin{pmatrix} V_1^- \\ V_2^- \end{pmatrix} = \begin{pmatrix} S_{11} V_1^+ \\ S_{21} V_1^+ \end{pmatrix}. \tag{3.3}$$

Q factor

By observing S_{21} (or S_{11}), one obtains the transmitted (or reflected) signal by the 2-port network (namely the resonator). The transmission amplitude spectrum $|S_{21}|$ of CPW resonator is typically a peak occurring at its resonant frequency f_0, because only around the resonance of the resonator, the microwave signal coming in form one port is permitted to transmit to the other side.

The bandwidth of the peak is decided by the quality factor of the resonator. As shown in Fig. 3.5) the bandwidth b_L which corresponds to the loaded quality factor Q_L could be measured at $\sqrt{2}$ times (or $3\,dB$ when converting the linear scale to dB scale which is used in Fig. 3.5) above the baseline of the transmitted amplitude,
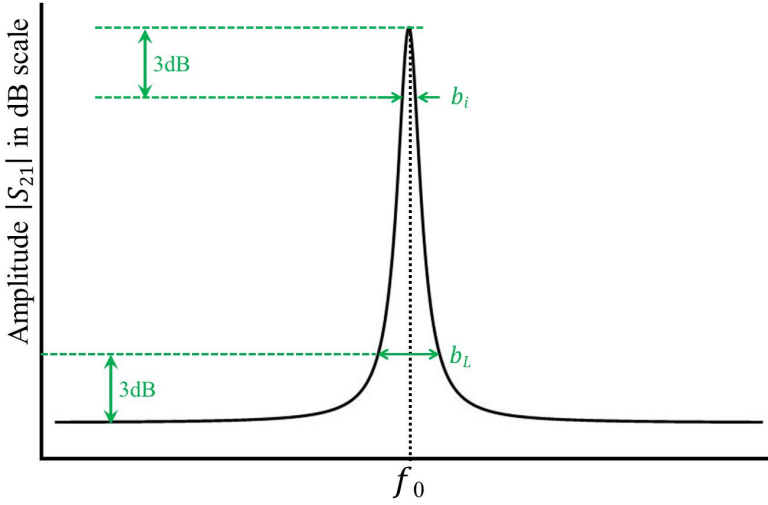
Figure 3.5: (Color online) Typical transmitted amplitude $|S_{21}|$ of CPW resonator. a peak occurs at its resonant frequency f_0, because only around the resonance of the resonator, the microwave signal coming in form one port is permitted to transmit to the other side. The loaded quality factor Q_L could be measured at 3 dB above the baseline of the transmitted amplitude, while the internal quality factor Q_i could be measured at 3 dB below the maximum of $|S_{21}|$. b_L and b_i are the bandwidths corresponding to Q_L and Q_i respectively.

while b_i could be measured at $\sqrt{2}$ times (3 dB) below the maximum of $|S_{21}|$ [Poz09]. Thus, the quality factors are calculated by

$$Q_L = \frac{f_0}{b_L},$$
$$Q_i = \frac{f_0}{b_i}. \tag{3.4}$$

In simulation, the ideal transmitted amplitude of a CPW resonator can be obtained by a Sonnet project shown in Fig. 3.6(a). Two ports on the box wall are attached through the coupling fingers to both ends of the CPW resonator to perform the network analysis. The $|S_{21}|$ spectrum could be seen in the response viewer shown in Fig. 3.6(b) by adding the "$DB[S21]$" curve. Actually, our design of the resonator is symmetrical, $|S_{21}|$ is identical to $|S_{12}|$. The type of metal material is chosen to be lossless, so that Q_i is infinite large, according to Eq. 2.18, one derives

$$Q_c = Q_L. \tag{3.5}$$

So that the coupling quality factor could be calculated by measuring the bandwidth 3 dB above the baseline of the transmission.

27
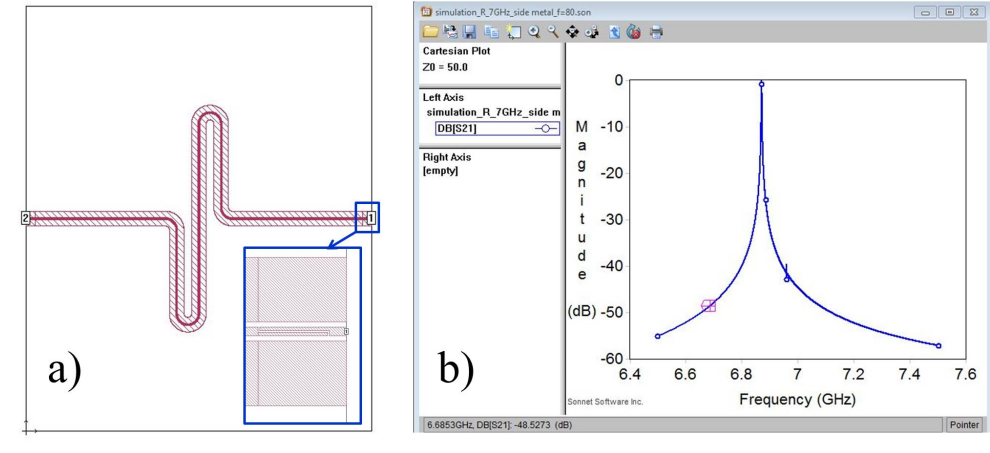
Figure 3.6: (Color online) Simulation about the quality factor of the CPW resonator. (a) The Sonnet project with two ports on the box wall attached through the coupling fingers to both ends of the CPW resonator to perform the network analysis. (b) The $|S_{21}|$ spectrum in the response viewer. The type of metal material is chosen to be lossless, namely Q_i is infinite large. Thus $Q_c = Q_L$ is obtained by measuring the bandwidth 3 dB above the baseline of the transmission.

3.2 Design of the transmon qubit

Although the theoretical model of the transmon qubit is clearly discussed in chapter 2.3, designing such a qubit is still not as straightforward as designing the CPW resonator. Not only because it has more parameters which relate to each other, but also the coupling to the read-out resonator and the flux bias loop should be taken into account. In this section, I discuss about how the parameters are calculated and how to make good compromise to obtain the desired values.

3.2.1 Characteristic parameters of the transmon

The major specialty of the transmon qubit is its relatively high E_J/E_C ratio compared to charge qubit. A target value between 50-100 is appropriate to ensure a good insensitivity to charge noise while maintaining a sufficient anharmonicity of the energy level. The Josephson energy and charging energy are defined by

$$E_J = \frac{\Phi_0}{2\pi} 2I_c \cos(\frac{\Phi}{\Phi_0}), \tag{3.6}$$

$$E_C = \frac{e^2}{2C_\Sigma}. \tag{3.7}$$

Here I_c is the critical current of the Josephson junction, it is doubled because the SQUID loop employed in this work contains a pair of identical Josephson junctions. Φ is the external flux which is assumed to be zero in the calculation, so that E_J reaches its maximum. C_Σ is the total capacitance of the transmon. Obviously, to manipulate the E_J/E_C ratio, the key parameters are I_c and C_Σ.

The critical current

I_c could be simply independently varied by the fabrication procedure. According to Ref. [KMM95], the product of the room-temperature resistance R_n and area A of a tunnel junction is a constant decided by the oxidation pressure and time of the tunnel barrier

$$R_n A = F(pressure \times time)^{0.9}, \tag{3.8}$$

with F, a constant factor differs for individual equipment, and calculated to be 346 in our case. For a junction oxidized for 25 minutes at 0.0148 mbar, $R_n A = 141.7 \ \Omega\mu m^2$ Given the junction area of 100 $nm \times 100 \ nm$, the resistance of the junction at room temperature should be $R_n = 14.17 \ k\Omega$. According to Ambegaokar-Baratoff formula,the critical current I_C is related to R_n in the form of

$$I_c = \frac{\pi\Delta}{2e} \tanh\left(\frac{\Delta}{2k_B T}\right)\frac{1}{R_n}, \tag{3.9}$$

where Δ is the superconducting gap of aluminum, and T is the temperature estimated to be 15 mK at which the sample is measured. As a result, the target critical current should be $I_c = 25 \ nA$. Plugging in the numbers in Eq. 3.6, I get

$$\frac{E_J}{h} = 24.8 \ GHz, \tag{3.10}$$

The geometric capacitance

On the other hand, C_Σ is a crucial parameter decided by the geometry of the transmon and the surrounding structures (the resonator, the ground panel, the substrate and etc.). It restricts not only E_C, but also the coupling strength between the resonator and the transmon.

The layout of the transmon qubit is illustrated in Fig. 3.7 by the violet structures. In the middle, there is a symmetric SQUID loop with 2 Josephson junctions. The interdigital fingers parallel to the junctions are the inter digital capacitors between the two arms of the transmon which crate the large shutting capacitance as discussed in Sec. 2.2. The long arms close to the center conductor of the resonator and the
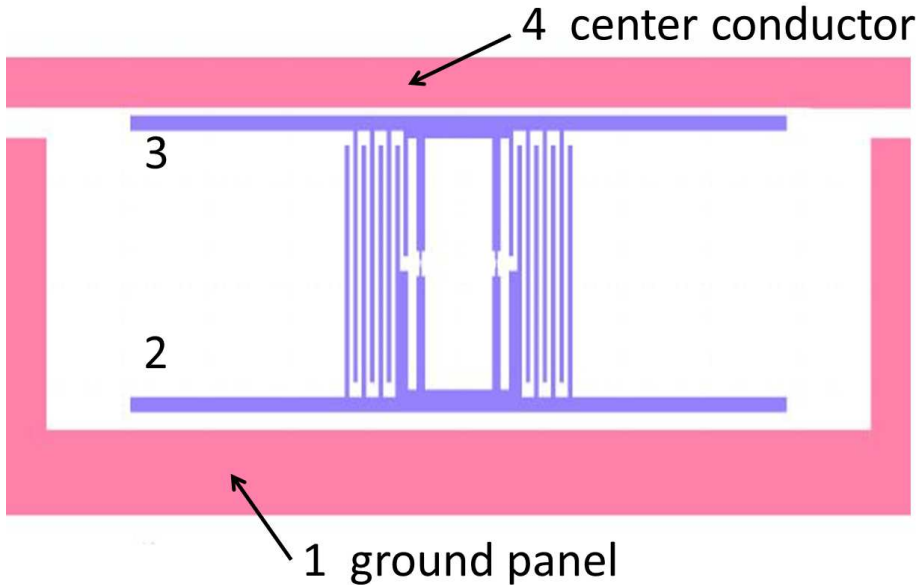
Figure 3.7: (Color online) Layout of the transmon qubit. (a) The geometry of the transmon (violet) and the surrounding structures. The interdigital fingers parallel to the junctions are the inter digital capacitors between the two arms of the transmon which crate the large shutting capacitance as discussed in chapter 2. The long arms close to the center conductor of the resonator and the ground are used to increase the coupling strength. (b) Zoom in of the design of Josephson junction.

ground are used to increase the coupling strength. The design of the junction will be discussed separately in the section of fabrication.

There is capacitance among the center conductor, upper and lower arms of the transmon qubit and the ground plate. As labeled by the number 1-4 in Fig. 3.7 (a), the equivalent circuit is represented in Fig. 3.8 (a). C_{23} is the inter digital capacitance of the transmon itself (i.e. the shunting capacitance). This circuit is complicated, it is much straight forward and more physical to simplify the circuit to the one shown in figure (d). C_{23} stays unchanged for the transmon, and all the other capacitances are equivalent to a coupling capacitor C_g.

To achieve the transformation, the voltage drop U_{ab} between point 'a' and 'b' needs to be calculated, and the circuit should be simplified. The first step is to transform

the "$\triangle - shape$" network of capacitors between point 'a', 'b' and 'd' into a "$Y - shape$" network of impedance shown by Fig. 3.8 (b). According to the transformation law,

$$
\begin{cases}
Z_a = \dfrac{Z_{34}Z_{23}}{Z_{34} + Z_{23} + Z_{24}}, \\[2mm]
Z_b = \dfrac{Z_{23}Z_{24}}{Z_{34} + Z_{23} + Z_{24}}, \\[2mm]
Z_d = \dfrac{Z_{34}Z_{24}}{Z_{34} + Z_{23} + Z_{24}},
\end{cases}
\tag{3.11}
$$

with

$$
Z_{ij} = \frac{1}{i\omega C_{ij}}.
\tag{3.12}
$$

plug the new network in and change all element to their impedance, one derives the circuit in Fig. 3.8 (c). With this circuit, it is easy to deduce the voltage U_{ab}.

$$
\begin{aligned}
U_{ac} &= \frac{Z_{13}}{Z_{13} + Z_a} U_{mc} \\[2mm]
&= \frac{Z_{13}}{Z_{13} + Z_a} \frac{Z_{mc}}{Z_{mc} + Z_d} V.
\end{aligned}
\tag{3.13}
$$

$$
\begin{aligned}
U_{bc} &= \frac{Z_{12}}{Z_{12} + Z_b} U_{mc} \\[2mm]
&= \frac{Z_{12}}{Z_{12} + Z_b} \frac{Z_{mc}}{Z_{mc} + Z_d} V,
\end{aligned}
\tag{3.14}
$$

where

$$
Z_{mc} = \left(\frac{1}{Z_a + Z_{13}} + \frac{1}{Z_b + Z_{12}} \right)^{-1}.
\tag{3.15}
$$

Thus,

$$
\begin{aligned}
U_{ab} &= U_{ac} - U_{bc} \\[2mm]
&= \left(\frac{Z_{13}}{Z_{13} + Z_a} - \frac{Z_{12}}{Z_{12} + Z_b} \right) U_{mc} \\[2mm]
&= \left(\frac{Z_{13}}{Z_{13} + Z_a} - \frac{Z_{12}}{Z_{12} + Z_b} \right) \frac{Z_{mc}}{Z_{mc} + Z_d} V.
\end{aligned}
\tag{3.16}
$$

With the result of Eq. 3.16, the voltage applied on the equivalent coupling capacitor in Fig. 3.8 (d) is simply

$$
\begin{aligned}
U_g &= V - U_{ab} \\[2mm]
&= \left[1 - \left(\frac{Z_{13}}{Z_{13} + Z_a} - \frac{Z_{12}}{Z_{12} + Z_b} \right) \frac{Z_{mc}}{Z_{mc} + Z_d} \right] V.
\end{aligned}
\tag{3.17}
$$

The last step is to calculate C_g based on the interdigital capacitor C_{23} of the transmon qubit directly by this relation

$$C_g = \frac{U_{ab}}{U_g} C_{23}$$

$$= C_{23} \frac{\left(\frac{Z_{13}}{Z_{13}+Z_a} - \frac{Z_{12}}{Z_{12}+Z_b}\right) \frac{Z_{mc}}{Z_{mc}+Z_d}}{1 - \left(\frac{Z_{13}}{Z_{13}+Z_a} - \frac{Z_{12}}{Z_{12}+Z_b}\right) \frac{Z_{mc}}{Z_{mc}+Z_d}}. \tag{3.18}$$

The total capacitance C_Σ is therefore

$$C_\Sigma = C_g + C_{23}. \tag{3.19}$$

The targeted C_{23} is 38 fF. To simulate the capacitance of the designed paten is the same as what is done for C_κ of the resonator. In the same way, I get all the geometric capacitances listed in Table. 3.1. By submitting all the numbers to Eq. 3.18,one gets $C_g = 4.67$ fF, and as a result,

$$\frac{E_C}{h} = 461.5 \; MHz. \tag{3.20}$$

Together with Eq. 3.10, one obtains

$$\frac{E_J}{E_C} = 53.8. \tag{3.21}$$

capacitor	C_{12}	C_{13}	C_{24}	C_{34}	C_{23}
value (fF)	17.0	7.4	3.8	15.4	37.3

Table 3.1: The geometric capacitances of the transmon qubit and its surrounding environment obtained from the simulation done by Sonnet project. The subscript numbers correspond to the labeling in Fig. 3.7 (a).

Substituting the numbers in Eq. 2.27, and Eq. 2.28, the transition frequencies from the ground state to the first excited state and from the first excited state to the second excited state of the transmon should be

$$f_{01} = 9.11 \; GHz$$
$$f_{21} = 8.65 \; GHz. \tag{3.22}$$
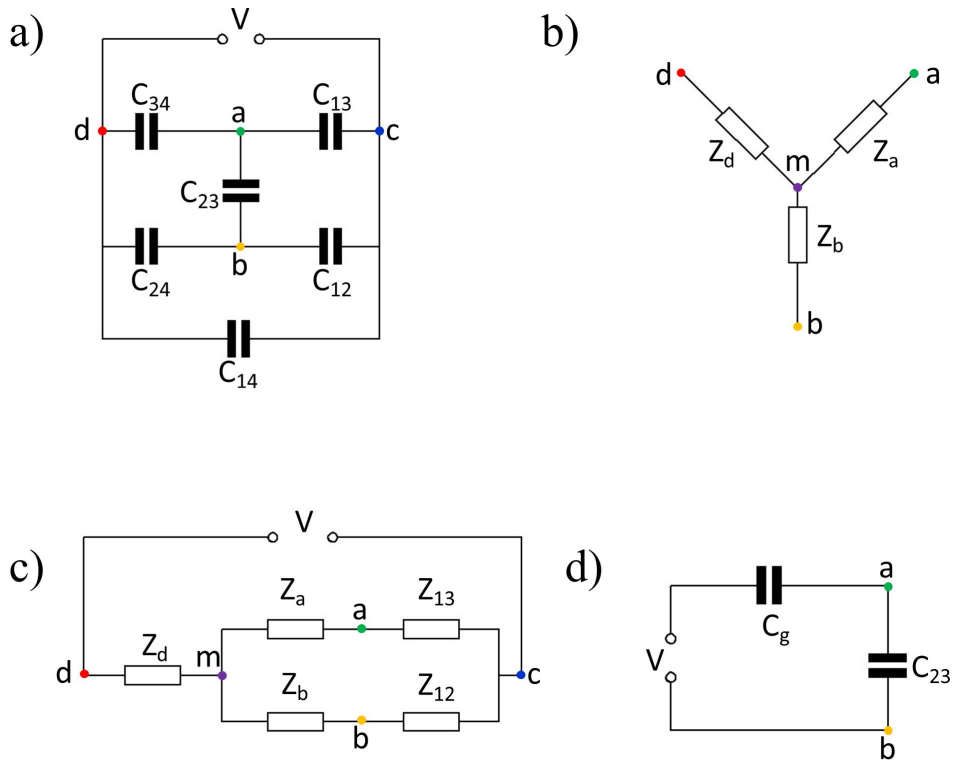
Figure 3.8: (Color online) Circuit of the geometric capacitance. (a) The full circuit of the capacitance among the center conductor, upper and lower arms of the transmon qubit and the ground. The numbers 1-4 correspond to the labeling in Fig. 3.7 (a). (b) The transformation of the "△-shape" network of capacitors between point 'a', 'b' and 'd' into a "Y-shape" network of impedance. (c) The simplified circuit after the transformation. (d) The final equivalent circuit in which C_{23} stays unchanged for the transmon, and all the other capacitances are equivalent to a coupling capacitor C_g.

3.2.2 Coupling to the resonator

As discussed above, the transmon qubit is coupled capacitively to the resonator and the ground (through the upper and lower arms as shown in Fig. 3.7). And it can be read out by the dispersive shift of coupled CPW resonator. The coupling strength between the qubit and the resonator is the most important parameter, which should approximate 100 MHz in our design, so that the coupling is neither too small which makes the dispersive shift invisible, nor too large which makes the qubit decaying fast. As defined by Eq. 2.41, the coupling between the resonator and basic transition of the transmon from ground state to the first excited state [Koc+07] is

$$
\begin{aligned}
g_{01} &= \frac{2eV_{rms}^0}{\hbar}\beta\langle 1|\hat{n}|0\rangle \\
&= \frac{eV_{rms}^0}{2\hbar}\beta\left(\frac{E_J}{8E_C}\right)^{1/4}.
\end{aligned}
$$

(3.23)

Because both $\beta = C_g/C_\Sigma$ and E_C are decided by the geometric capacitance, one is able to control the coupling strength by varying C_g. However, it is not straightforward, the coupling strength is related to all the relevant capacitance defined in Eq. 3.18. But eventually, by increasing the capacitance C_{12} and C_{34}, which means making the 2 horizontal arms longer, the coupling capacitor could be increased distinctly. substitute all the value of capacitors listed in Table. 3.1 and parameter calculated before, one obtains the coupling strength of the resonator for the basic transition frequency of the qubit:

$$
g_{01} = 113.0 \; MHz.
$$

(3.24)

The dispersive shift of the resonator is used to readout the status of the qubit. Deducing from Eq. 2.46, the shift of the resonator corresponding to the fundamental transition of the qubit is

$$
\chi_{01} = \frac{g_{01}^2}{\omega_{01} - \omega_r} = -1.7 \; MHz
$$

(3.25)

3.2.3 Coupling to the flux bias loop

As illustrated in Eq. 3.6, the Josephson energy of the SQUID is tunable by changing the external flux trapped in the loop, which enables the tunability of the transition frequency of the transmon qubit. To change the external flux threading the SQUID loop, a "U-shape" wire is placed close enough to it (see Fig. 3.9). With a DC current I_{DC} running in the wire, through the mutual inductance M_{bias} between them, an external flux is trapped in the SQUID loop. The dimensions are annotated in Fig. 3.9

and the origin of coordinates is chosen to calculate the mutual inductance. The mutual inductance created by the left and right vertical parts of the flux bias wire cancel with each other due to the symmetry. Thus only the horizontal part of the flux bias is taken into account to the total mutual inductance. Performing the integration around the full loop of the SQUID, one obtains the mutual inductance

$$
\begin{aligned}
M_{bias} =& \frac{\mu_0}{4\pi} \int_0^{2l} dx_1 \int_{l-\frac{a}{2}}^{l+\frac{a}{2}} \frac{1}{\sqrt{(x_1-x_2)^2+h^2}} dx_2 \\
& - \frac{\mu_0}{4\pi} \int_0^{2l} dx_1 \int_{l-\frac{a}{2}}^{l+\frac{a}{2}} \frac{1}{\sqrt{(x_1-x_2)^2+(h+b)^2}} dx_2 \\
=& \frac{\mu_0}{4\pi} \int_0^{2l} dx_1 \ln \frac{[x_1-(l+\frac{a}{2})]^2 + \sqrt{h^2+[x_1-(l+\frac{a}{2})]^2}}{[x_1-(l-\frac{a}{2})]^2 + \sqrt{h^2+[x_1-(l-\frac{a}{2})]^2}} \\
& - \frac{\mu_0}{4\pi} \int_0^{2l} dx_1 \ln \frac{[x_1-(l+\frac{a}{2})]^2 + \sqrt{(h+b)^2+[x_1-(l+\frac{a}{2})]^2}}{[x_1-(l-\frac{a}{2})]^2 + \sqrt{(h+b)^2+[x_1-(l-\frac{a}{2})]^2}}.
\end{aligned}
\tag{3.26}
$$

Substituting the designed dimensions ($l = 60\ \mu m$, $h = 65\ \mu m$, $a = 16\ \mu m$, and $b = 50\ \mu m$) into Eq. 3.26, the mutual inductance M_{bias} is calculated, thus, the DC current needed for one flux quanta is

$$
\begin{aligned}
I_{bias} =& \frac{\Phi_0}{M_{bias}} \\
=& 1.99\ mA.
\end{aligned}
\tag{3.27}
$$

3.3 Fabrication of the sample

The samples correlated to this work are all produced by ourselves at KIT (Karlsruhe Institute of Technology), in the clean room of CFN (Center for Functional Nanostructures), and we also fabricate superconducting qubits for our collaborators (for example the sample measured in the work Ref. [Shu+17]). Generally, there are two ways of lithography for this type of sample: optical lithography [WDR97] and electron-beam lithography [Vie+00]. Optical lithography is proper for structures larger than 1 μm (such as the CPW resonator, the flux bias lines, the ground plate and etc.) with simple processing steps which is straightforward and easily done by ourselves. The electron-beam lithography is employed for fine structures (for example the Josephson junctions) with more accuracy, and is more complicated naturally.
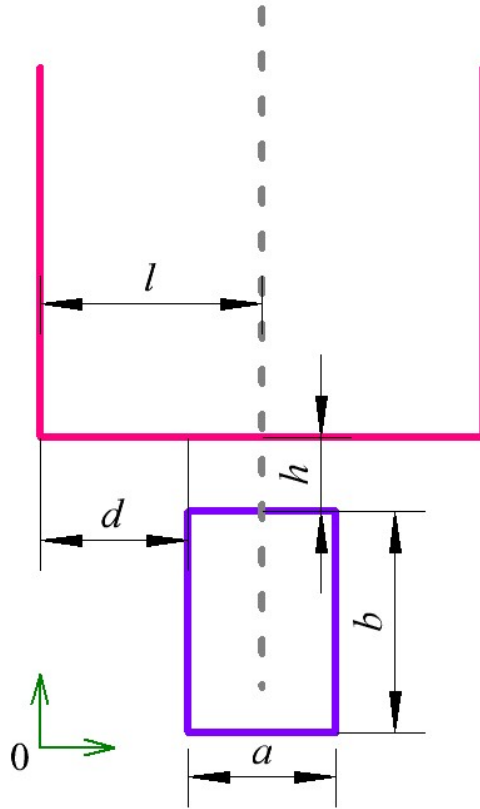
Figure 3.9: (Color online) Schematic diagram of the SQUID loop (violet) and its flux bias line (pink). A DC current is applied to the "U-shape" wire, and through the mutual inductance M_{bias} between them, an external flux is trapped in the SQUID loop. The dimensions are annotate and the origin of coordinates is chosen to calculate the mutual inductance.

Thanks to the teamwork in our group, the technique of fabrication is developing and several standard recipes are built. Usually, the recipe which combines the optical lithography and electron-beam lithography is chosen for such resonator-qubit sample. This strategy separates the fabrication of the qubits from all the other structures, which allows one to print large ground panel that makes the grounding of the resonator better, and makes it easy to change or test the resonator individually. But I give up these advantages, and decide to produce all structures by one turn of electron-beam lithography. The reason is that, with this simplified strategy, the misalignment between the two lithography is avoided. More importantly, this strategy avoids unevenness on top of the substrate surface caused by residual chemicals and deposited aluminum. It makes the Josephson junctions more reliable and reproducible, which in turn insures the property of the transmon qubits.

In this section I talk about the procedure of the electron-beam lithography employed for our fabrication. The Josephson junctions are the most subtle and crucial components, the fabrication technique employed in our work for the junctions is called Niemeyer–Dolan technique [Nie74; NK76; Dol77].

3.3.1 Resist coating and pattern writing

The material of the substrate is ultra-pure intrinsic silicon with the thickness of 350 μm. With a surface size of $2\ cm \times 2\ cm$. The dimension of each chip is $0.5\ cm \times 0.5\ cm$, which allows us to fabricate 9 chips on one piece of substrate at the same time. The substrate is cleaned with the stripper named NMP at the beginning to remove the protecting photoresist.

Resist coating

To finally produce the elements shown in Fig. 3.2 with aluminum film, the first step is to make a mask out of photoresist on the surface of the substrate with the designed pattern. To apply the resist, the equipment called spin-coater is employed (Fig. 3.10 a) using a 2-step program. The first step is with low spinning speed (300 round/minute) for 10 seconds, to make sure the drops of resist cover the complete substrate homogenously. In the second step, the spin-coater rotates with a high spinning speed (3000-6000 round/minute) for 60 seconds, in this way to get the desired thickness of the resist. As shown in Fig. 3.10 (b), the first layer is LOR (lift off resist) with thickness of 500 nm, and the second one is PMMA with thickness of 100 nm. At the end of the coating of each layer, it is important to let the resist reflow by itself for 30 seconds and get baked, in order to make sure each layer of the resists is flat and robust.
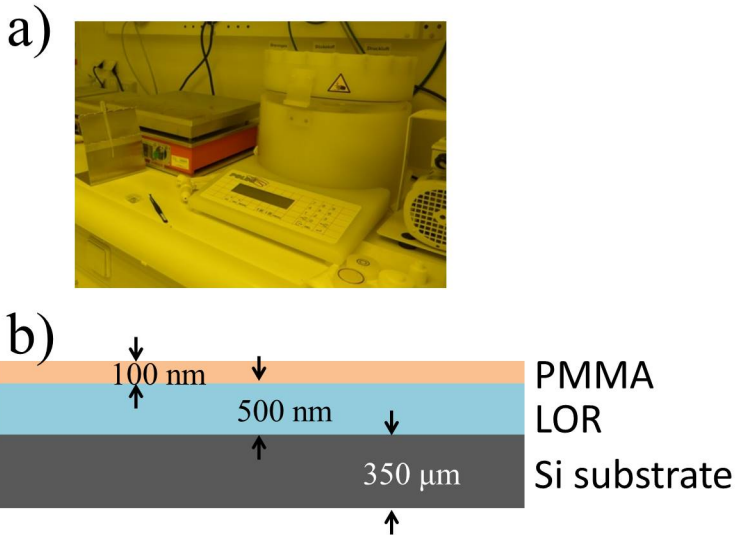
Figure 3.10: (Color online)Spin-coating of the resist. (a) The spin-coater that is employed using a 2-step program. The first step is with low spinning speed (300 round/minute) for 10 seconds, to make sure the drops of resist cover the complete substrate homogenously. In the second step, the spin-coater rotates with a high spinning speed (3000-6000 round/minute) for 60 seconds, in this way to get the desired thickness of the resist. (b) The cross-section of the sample. The first layer of the resists is LOR (lift off resist) with thickness of 500 nm, and the second one is PMMA with thickness of 100 nm. The thickness of the silicon substrate is 350 μm.

Electron beam exposure

The procedure of electron-beam exposure according to the pattern of the design is done by the e-beam writer JEOL JBX-5500FS/50 keV (shown in Fig. 3.11 a). In this step, electron beam is perpendicularly shot on the chip line by line at the targeted area (Fig. 3.11 b). The higher the current, the faster the writing speed, but the less the accuracy. The maximum of the current (6 nA) is used to write the μm-scale structures, a much lower current (100 pA) is chosen for the transmon geometry as well as the junction area. The base dose of the exposure is 300 $\mu C/cm^2$, all structures is written with 100% of this dose. Except for the bridge, which is written by only 20% of the base dose. With this low value, only the LOR gets exposed. On this account, it is clean under the bridge after the development. Due to the difference in sensitivity to the exposure and reflection by the substrate, the layer of LOR gets more exposed by the e-beam compared with PMMA.

a)
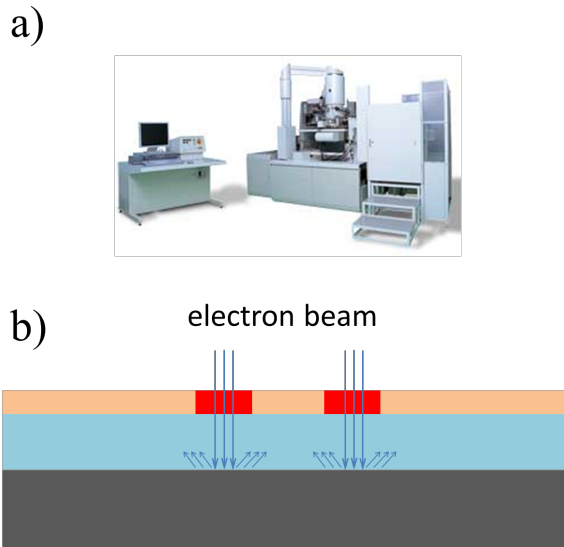
b) electron beam

Figure 3.11: (Color online)Electron-beam exposure of the resist. (a) The e-beam writer: JEOL JBX-5500FS/50 keV. (b) The illustration of the writing process that the electron beam is perpendicularly shot on the chip line by line at the targeted area. The higher the current, the faster the writing speed, but the less the accuracy.

Development of the resists

After exposure, the resists are ready to be developed. The first step is to develop the PMMA (Fig. 3.12 a) using the mixture of MIBK and isopropanol with the ration of 1:3 for 65 seconds. One could see the exact pattern under the microscope already after that. The next is to develop the LOR which is a particularly crucial step, as it forms the Niemeyer–Dolan bridge [Nie74; Dol77] for producing the Josephson junction. Since LOR is exposed more than the PMMA, during raising the chip in the developer made by MIF726 and water (with the ratio 3:2) for 120 seconds, more LOR is dissolved in the developer. Thus a undercut is formed by the LOR under the PMMA layer (Fig. 3.12 b). With this undercut, the Niemeyer–Dolan bridge (3D illustration in Fig. 3.12 c)is built for the Josephson junction area, which enables one to perform the shadow-evaporation in the next step. It is very important to stick to the development time in the recipe. One second less will leave residue under the bridge, on the other hand, one second more makes the undercut over-sized which makes the bridge fragile and easy to fall apart.
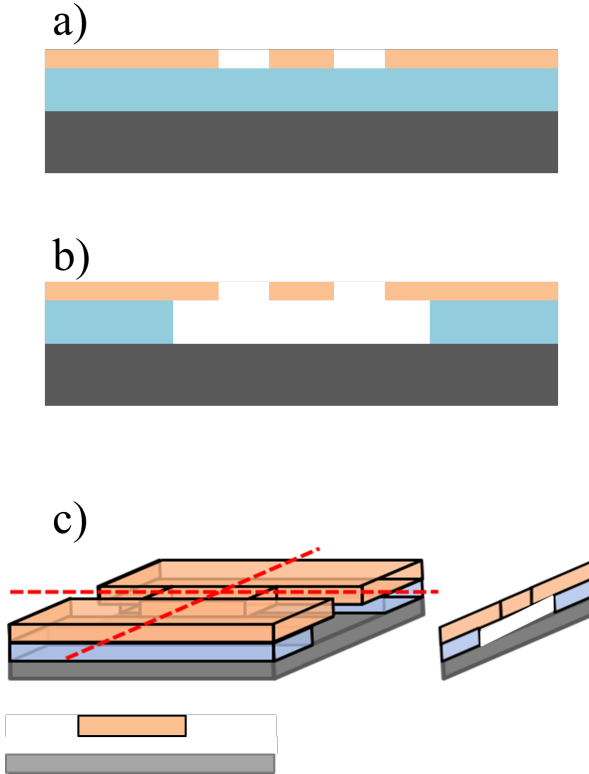
Figure 3.12: (Color online)Development of the resist. (a) The result of developing PMMA. (b) The illustration after development of LOR. Since LOR is exposed more than the PMMA, during raising the chip in the developer, more LOR is dissolved in the developer. Thus a undercut is formed by the LOR under the PMMA layer. (c) 3D illustration of the Niemeyer–Dolan bridge [Nie74; Dol77], which is formed by the undercut of LOR, and enables one to perform the shadow-evaporation for the Josephson junction. The figures beneath and on the right are the cross-sections corresponding to the red dashed lines.

3.3.2 Josephson junction fabrication with shadow-evaporation technique

The Josephson junctions as well as all other elements are deposited by a sputtering equipment (Fig. 3.13 a) provided by the company PLASSYS. All parameters can be seen and controlled by the computer, all of the fabricating projects can be stored and executed by the computer as well. The schemata of the sputtering machine is shown in Fig. 3.13 (b). The substrate is mounted to the sample holder in the load lock. the holder could be rotated horizontally and turned vertically by any degree. The box of high purity aluminum is placed at the bottom of the main chamber, with a proper magnetic field, an electron beam is shot at the aluminum target, and the aluminum is sputtered uniformly in the hermetic space.

The substrate with developed resists is installed to the sample holder upturned. First, the load lock as well as the main chamber are pumped over a weekend to reach a vacuum environment. After that, titanium is sputtered for a few seconds with the shutter between the load lock and the main chamber closed, so that the pressure is further reduced, and one reaches 1.7×10^{-8} *mbar* of the main chamber and 2.4×10^{-8} *mbar* of the load lock.

Performing argon cleaning is helpful before sputtering the aluminum on chip, because it improves the quality of the Josephson junction if the junction lies on a clean substrate. As shown in Fig. 3.13 (b), the sample is turned to the left, thereby, the gas of argon ions with a flow rate of 4 standard cubic centimeter per minute(*sccm*) accompanied with 0.5 *sccm* of O_2 gas is shot onto the sample and takes away the organic residual.

Only after cleaning, the shadow-evaporation (illustrated in Fig. 3.14) starts. There are 3 steps in this procedure. First of all, the sample is turned downwards, but with a 8 degree angle to the left of the horizontal position. The shutter between the load lock and the main chamber is open. And the aluminum is sputtered with a rate of 0.2 *nm/s* on-chip and stopped at the thickness of 30 *nm*. The next step is to oxidize the surface of the aluminum film. For that, the shutter is closed, and dynamic oxidation is employed for 25 minutes, which means the oxygen gas is flowing through the load lock with a half-closed butterfly valve. The last step is tuning the sample to 8 degree angle to the right of the horizontal position, and perform a deposition of the second layer of aluminum film with the rate of 0.2 *nm/s*, and finally reaches the thickness of 50 *nm*. With these 3 steps, a superconductor-insulator-superconductor structure is formed under the Niemeyer–Dolan bridge, and the Josephson junction with targeted parameters is obtained.
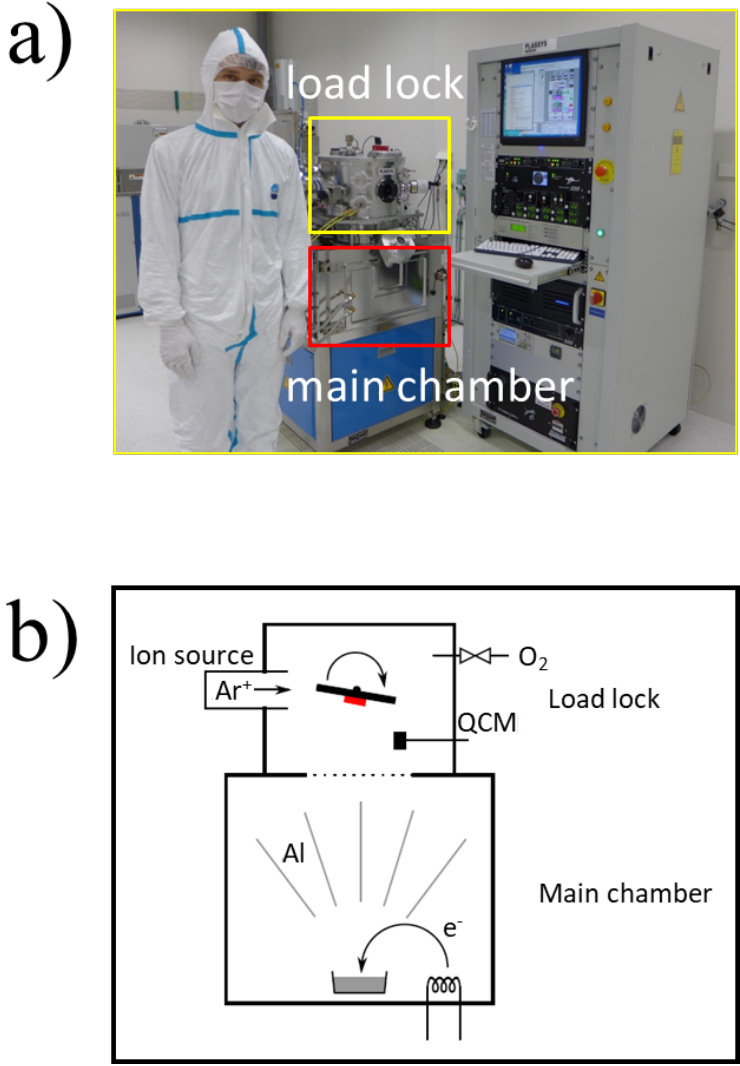
Figure 3.13: (Color online)The Shadow-evaporation equipment PLASSYS. (a) A picture taken in the clean room of CFN. On the left side is the load lock with the main chamber under it. On the right side is the controlling system. (b) The schematic of the metal deposition and oxidation.
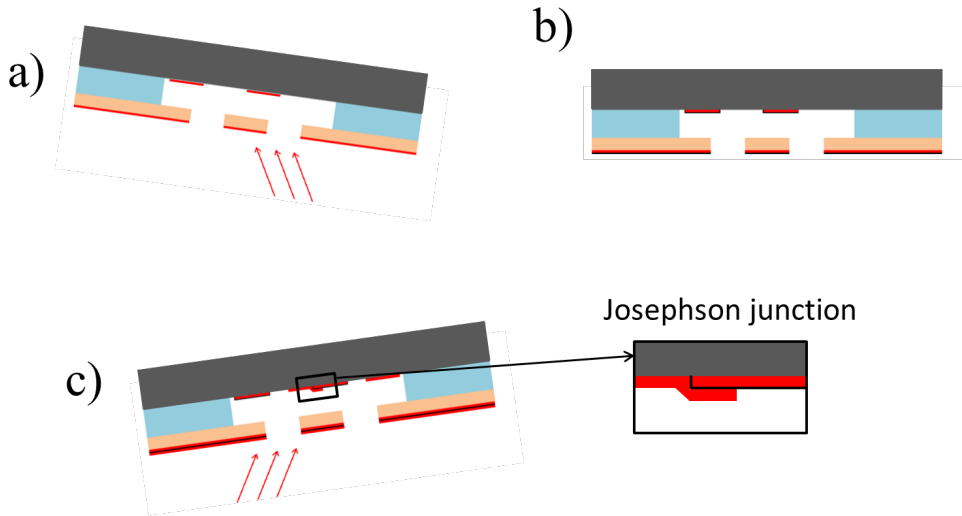
Figure 3.14: (Color online)Illustration of shadow-evaporation technique of the Josephson junction. (a) The first step of the shadow-evaporation. The sample is turned downwards, but with a 8 degree angle to the left of the horizontal position. The shutter between the load lock and the main chamber is open. And the aluminum is sputtered with a rate of 0.2 nm/s on-chip and stopped at 30 nm thick. (b) The oxidation of the surface of the aluminum film which forms the insulator for the Josephson junction. For that, the shutter is closed, and dynamic oxidation is employed for 25 minutes, which means the oxygen gas is flowing (with a rate of 12 $sccm$)through the load lock with a half-closed butterfly valve. (c) The deposition of the second layer of aluminum, with the rate of 0.2 nm/s, and finally reaches the thickness of 50 nm.

There are two crucial challenges in the fabrication process. The first one is to build the Niemeyer–Dolan bridge as explained above. The second one is the dynamic oxidation process which forms the insulating barrier for the junction. On the basis of Eq. 3.8 and Eq. 3.9, the critical current of a Josephson junction is determined by the oxidation pressure and time. It is easy to control the time, but, the pressure is decided by the flow rate of the oxygen gas, and follows a linear relation

$$p(flow) = A \frac{mbar}{sccm} \cdot flow - B \, mbar, \tag{3.28}$$

here A and B are ideally two constants, however, they drift after several weeks or so. What's more, the pre-factor F in Eq. 3.8 is also a constant, but may deviate after several weeks.
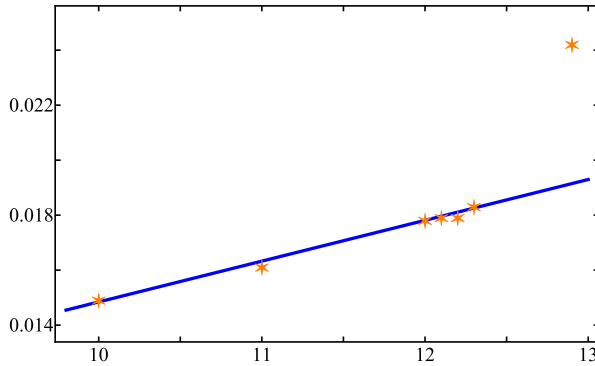
Figure 3.15: (Color online)Linear data fit for Table 3.2. High flow rate bigger than 12.5 *sccm* does not obey the linear relation. Even though the targeted flow is 12.8 *sccm*, a flow of 12.0 *sccm* is chosen.

Thus, it is important to test the relation between oxygen flow and pressure, before mounting the sample in. The test result is listed in Table 3.2. By Running a linear fit, the constants in Eq. 3.29 should be

$$A = 0.00148432, B = -9.87 \times 10^{-16}. \tag{3.29}$$

The data and linear fit are shown in Fig. 3.15. According to the test, although the targeted flow is 12.8 *sccm*, a flow rate of 12 *sccm* of oxygen in the dynamic oxidation procedure is chosen. Because 12.8 is close to the upper limit of the flow rate, and the real pressure is not predictable.

flow rate	10 *sccm*	11 *sccm*	12 *sccm*	12.3 *sccm*	12.9 *sccm*
start pressure (*mbar*)	0.0153	0.0166	0.0181	0.0186	0.0246
stable pressure (*mbar*)	0.0149	0.0162	0.0178	0.0183	0.0242

Table 3.2: The oxygen pressure test using different flow rate before mounting the sample into the PLASSYS.

The last procedure of fabrication is to strip off all the resist along with the aluminum deposited on top of them. The sample is dipped in NEP in a small beaker which allows the chip to lean on the cup wall with face down. Only in this way, the aluminum deposited on the resist will not fall down to the substrate when removing the resist. The remover is heated to 80 degree for a few minutes, and then the beaker

is put in an ultrasonic bath with power level 1 for 10 seconds to shake off the solved pieces. These two steps need to be alternated with patience, the whole procedure takes hours.

The pictures of the finished sample is shown in Fig. 3.16. Figure a) shows the whole chip pictured by a combination of digital camera and microscope in the clean room which has yellow light. The zoomed-in view of a qubit and its bias "U" noted by the green frame in Fig. 3.16 a) is shown in figure b). Figure c) is a picture of one Josephson junction of the test junctions after the property testing. It is not achievable to take a picture of the transmon qubits that I want to measure, because the Scanning Electron Microscope destroys the junctions during scanning.

3.3.3 Junction property testing

It is easy to tell the quality of the structure of the fabricated sample by observing the elements under the microscope. But only a clear and clean structure does not mean it is a successful sample. The most crucial and fragile elements are the nano-scale Josephson junctions of the transmon qubits, which could not be tested directly. They are evaluated by the testing junctions depicted in Fig. 3.2 (a). The test junctions are designed to have the same length and different width to test how the oxidation process works.

A Four-point probe station is required to measure the room-temperature resistance of the test junctions. The scheme is illustrated by Fig. 3.17. A current source is attached to two metal pads for the junction. In parallel to the junction, a variable resistor is employed to protect the junction. A current source is used to apply the DC current on the junction. In order to obtain the I-V curve, the voltage drop across the junction is monitored together with the voltage corresponding to the DC current by the XY-mode of an oscilloscope. It is easy to make contact to the pads of the test junction with 4 probing needles of the station. However, one has to pay attention to setting the variable resistance to a small value before operating, such that accidental destroy of the junction by a high current is avoided. The result of the measurement is list in Table 3.3 for 3 different junction sizes. According to the result, the prefactor F in Eq. 3.8 should be 225.
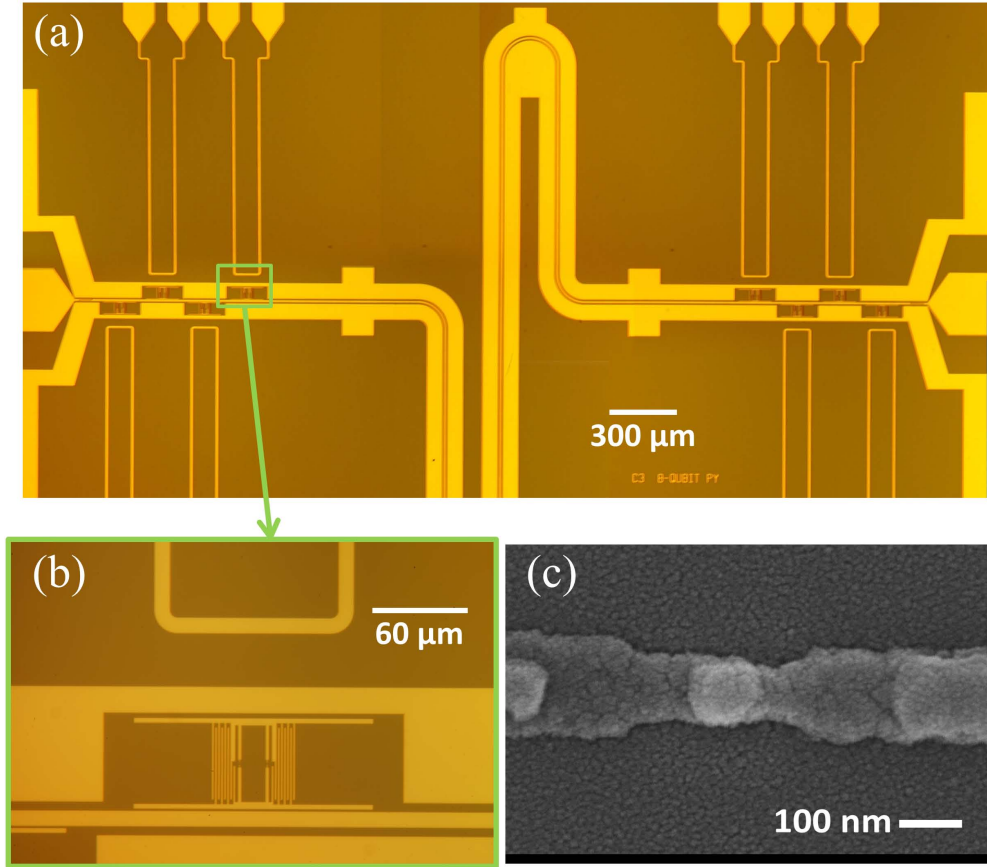
Figure 3.16: (Color online)The picture of the fabricated 8-qubit sample. (a) The whole chip pictured by a combination of digital camera and microscope in the clean room which has yellow light. (b) Zoomed-in view of a qubit and its bias "U". (c) A picture of one Josephson junction of the test junctions after the property testing. Because the Scanning Electron Microscope destroys the junction during viewing the junction with electron beam.

junction area A ($nm \times nm$)	measured resistance ($k\Omega$)	$\bar{R}$ ($k\Omega$)	$\bar{R} \times A$ ($\Omega \cdot \mu m^2$)
150×100	7.0/7.0/6.8/6.4/7.0/7.4/7.6/6.8/6.6/7.4/6.8	7.0	104.7
200×100	5.4/5.6/5.0/6.0/5.6/5.8/5.6/6.2/5.8/5.0/5.4/5.4/5.6	5.6	111.4
300×100	3.8/3.5/3.3/3.2/4.1/3.7/3.4/3.8/4.0/3.4/3.7/3.0	3.6	107.3

Table 3.3: Measured data of the room-temperature resistance of the testing junctions. The 4-point probe station and a oscilloscope is employed to obtain the I-V curve.
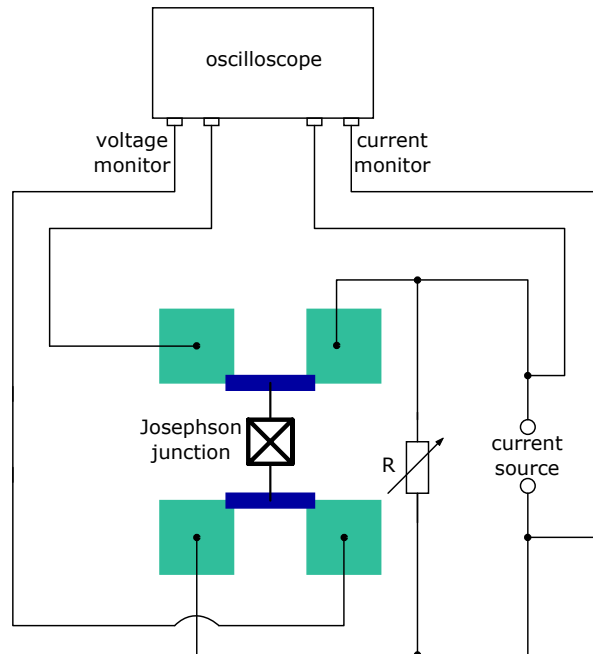
Figure 3.17: (Color online) Illustration of the measurement of the room-temperature resistance for the testing junctions. A current source is attached to two meal pads for the junction. In parallel to the junction, a variable resistor is employed to protect the junctions from damage due to high current. In order to obtain the I-V curve, the voltage across the junction is monitored together with the voltage corresponding to the driving current by the XY-mode of an oscilloscope.

4 Experimental result of the single-qubit chip and 8-qubit chip

In this chapter, I explain the experimental setup for cryogenic measurement, show the data of the single-qubit measurement, and explain the result of experiment on multi-qubit chips. Performing a measurement on the single-qubit chip is necessary for examination of the resonator and qubit properties. The result I obtained shows good agreement between experimental data and the designed values.

Of course, the system formed by multiple qubits coupling to a mutual cavity bus is more attractive not only as a toy model for quantum many-body physics but also for computational applications. It moves from the well-known Jaynes-Cummings [JC63] to the intriguing complicated Tavis-Cummings [TC68] model.

In our experiments on the 8-qubit chip, the microwave transmitted through a superconducting CPW resonator coupled to multiple superconducting transmon qubits shows a Fano resonance whose hallmark is the asymmetric line-shape caused by the interference between the resonator and the background [Fan61]. The spectra is explained by considering an effective microwave background which has dissipative and reactive elements that can depict the energy levels of the Tavis-Cummings model [Lep+]. For N qubits degenerated with a mutual harmonic oscillator, the total effective coupling strength for the ensemble scales with $\sqrt{N}$, which leads to an expected level crossing of $2g\sqrt{N}$ in experimental data [Fin+09].

Obviously, adding more qubits increases the complexity of circuit control. Although I have 8 fully tunable qubits, I finally achieved 6 fully-controllable transmon qubits which could be tuned individually in resonance with the resonator.

4.1 Experimental setup

4.1.1 Cryogenic environment for experiments

Cryogenic environment is required for the experiments because of two reasons. On one hand, the principle of the Josephson junction which is the critical element of the transmon qubit is based on superconducting material. The superconductor employed in our work is aluminium with high purity of which the critical temperature is roughly 1.2 K [MGC63]. On the other hand, a much lower temperature than the critical temperature is needed to reduce the effect induced by quasi particles and thermal excitation of the resonator and the qubits.

The dilution refrigerator [DOT65] showed in Fig. 4.2 is a commonly used equipment to reach mK temperature. The working principle of dilution refrigerator is illustrated in Fig. 4.1. The main idea is to generate the cooling power from the energy needed to break the attractive force when helium-3 dilutes into super-fluid helium-4. The liquids depicted in yellow, green and blue are liquid helium-4, liquid helium-3, and their mixture respectively. The base temperature of the dilution refrigerator is around 10 mK at the stage called mixing chamber, where the samples are mounted to. There are several stages with different temperatures which realize the circulation of the mixture in a sealed loop. At the top is the room-temperature stages where all microwave cables and control-unit are connected to the fridge. There is 77 K stage (not shown) that attached to the liquid nitrogen bath, and 4 K stage which is contacted to the liquid helium bath. The 1.5 K stage is where the 1 K pot is placed. The 1 K pot sucks liquid helium form the helium bath, and generates cooling power with evaporating the liquid helium. It is winded by the thin capillary of the condenser which condenses the helium-3 gas into liquid. The temperature of the stage where the still sits is around 600 mK. It is heated with external heater and pumps pure He-3 gas form the liquid mixture, because He-3 and He-4 has different evaporating pressure. Between the stages of the still and the mixing chamber there is 2 more stage with temperature around 50 mK, where the heat exchangers are installed to further cool down the mixture. The mixing chamber is placed on the lowest stage and reaches the base temperature because of He-3 diluting in super-fluid He-4.

As shown in Fig. 4.2, the dilution refrigerator used in this work has a large operation space. With a 2-port switch and a 4-port switch, it enables us to measure 9 samples in one run. However, cooling down such a giant refrigerator is not as simple as the small ones, that's why the pre-cooler is installed to pre-cool the setup with liquid nitrogen and liquid He-4. The time needed for cooling down the refrigerator is three and half days.
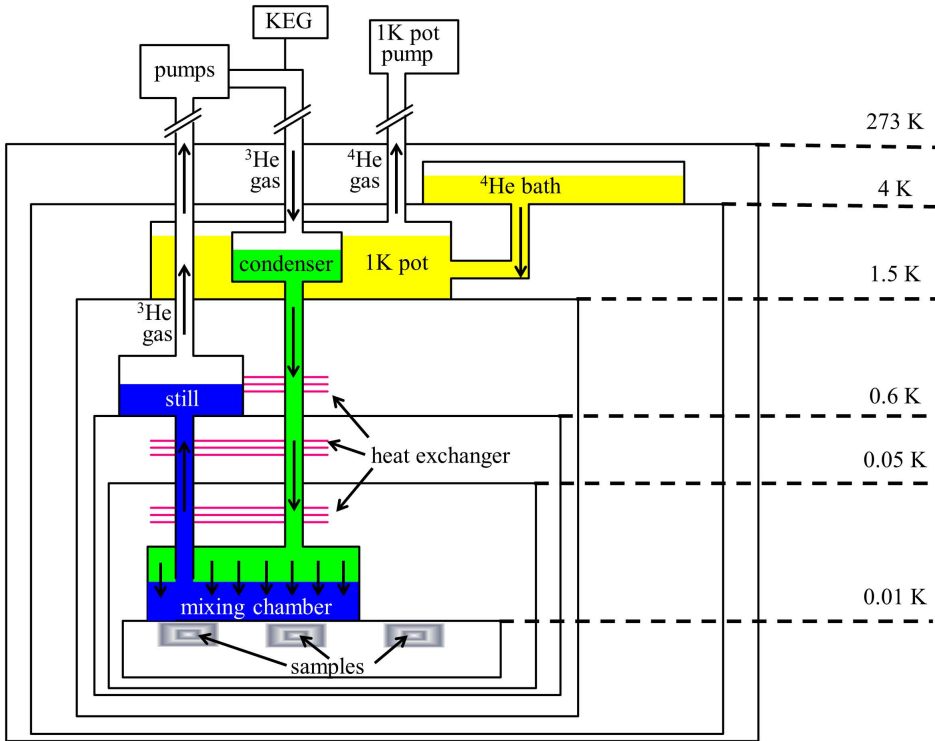
Figure 4.1: (Color online) The working principle of dilution refrigerator. There are several stages with different temperatures which realize the circulation of the mixture in a sealed loop. At the top is the room-temperature stages where all microwave cables and control-unit are connected to the fridge. There is 77 *K* stage (not shown) that attached to the liquid nitrogen bath, and 4 *K* stage which is contacted to the liquid helium bath. The 1.5 *K* stage is where the 1 *K* pot is placed. The 1 *K* pot sucks liquid helium form the helium bath, and generates cooling power with evaporating the liquid helium. It is winded by the thin capillary of the condenser which condenses the helium-3 gas into liquid. The temperature of the stage where the still sits is around 600 *mK*. It is heated with external heater and pumps pure He-3 gas form the liquid mixture, because He-3 and He-4 has different evaporating pressure. Between the stages of the still and the mixing chamber there is 2 more stage with temperature around 50 *mK*, where the heat exchangers are installed to further cool down the mixture. The mixing chamber is placed on the lowest stage and reaches the base temperature because of He-3 diluting in super-fluid He-4.

Figure 4.2: (Color online) The dilution refrigerator used in this work. It supplies enough space to measure 6 qubit-samples in one run, plus additional 3 resonator-samples. Cooling down such a giant refrigerator is not as simple as the small ones, that's why the pre-cooler is installed to pre-cool the setup with liquid nitrogen and liquid He-4 in order to reduce the time for cooling down to three and half days.
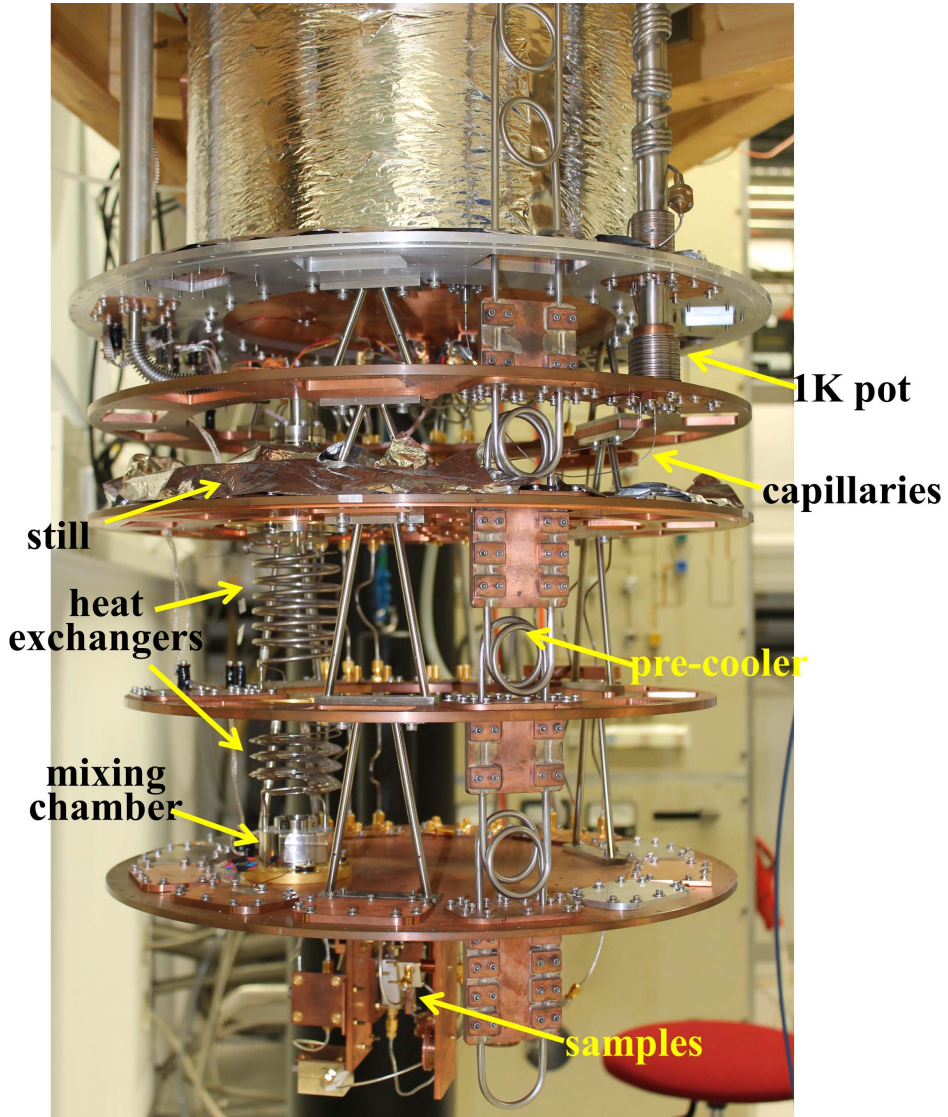
4.1.2 Equipment for measurement

Wiring inside the refrigerator

The wiring inside the dilution refrigerator is illustrated in Fig. 4.3. There are 3 attenuators in every incoming lines (with -20 dB attenuation each), in order to insure single-photon level of power on the chip. They are mounted on the 4-K plate, 0.6-K plate and the base plate respectively. The sample is attached to one brunch of the 2-port switch. Because of the circulator after the sample, one is able to perform measurement on both transmission (switch at position $SW1$) and reflection (switch at position $SW2$). The second circulator is employed to reduce the noise from the outgoing line to the sample. The signal is amplified by a cryogenic high-electron-mobility transistor (HEMT), which is mounted to the 4 K stage and supplies about $+40\,dB$ amplification.

Equipment at room temperature

The equipment used to spectroscopically measure the sample is shown in Fig. 4.5 a). The VNA (vector network analyzer) is the device to do the 2-port network measurement. The microwave coming out of the VNA is attenuated by an adjustable attenuator, and then combined with the signal from the microwave generator with a directional coupler. The coupler gives an additional $-20\,dB$ attenuation for the signal form the VNA, but no attenuation for the microwave generator. And the mixed microwave is sent from port 1 into the dilution refrigerator as shown in Fig. 4.3. The signal coming out of the fridge is sent into port 2 of the VNA through 2 room-temperature amplifiers which should have $+20\,dB$ amplifying factor. The microwave generator is switched off during the measurement on the resonator, it is used to drive the qubits.

The current sent through the "U"-shape bias lines on the chip is generated by the current source made by the workshop of our institute. The current source is powered by the voltage from a digital-to-analog converter (DAC) which is controlled by the measurement computer. Before going to the sample, the current generated from the current source goes through a current divider which is illustrated in Fig. 4.4. $R_{sam} \approx 500\,\Omega$ is the resistance of the wire from 4 K stage till the grounding of the sample. $R_{div} = 50\,\Omega$ is the resistor of the current divider which is installed and grounded on the 4 K stage. As a result, the DC current I_{sou} generated form the current source mainly goes through the current divider and is roughly 10 time reduced when I_{sam} gets to the sample. It benefits the experiment because the noise from the current source is also reduced by a factor of 10.
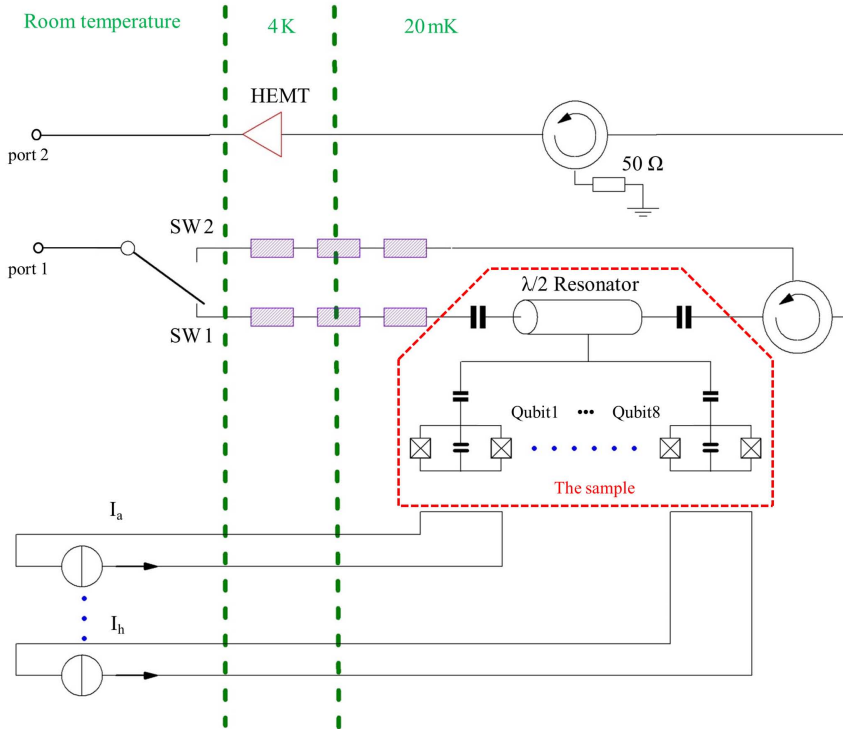
Figure 4.3: (Color online) The wiring inside the dilution refrigerator. 3 attenuators are installed in each of the incoming lines, with -20 dB attenuation each. They are placed on the 4-K plate, 0.6-K plate and the base plate respectively. The sample is attached to one brunch of the 2-port switch. Due to the circulator after the sample, one is able to perform measurement on both on transmission (switch at position $SW1$) and reflection (switch at position $SW2$). The second circulator is employed to reduce the noise from the outgoing line to the sample. The signal is amplified by a cryogenic high-electron-mobility transistor (HEMT), which is mounted to the 4 K stage and supplies about $+40$ dB amplification.
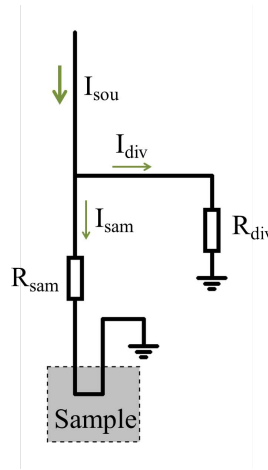
Figure 4.4: (Color online) The circuit of the current divider. $R_{sam} \approx 500\ \Omega$ is the resistance of the wire from 4 K stage till the grounding of the sample. $R_{div} = 50\ \Omega$ is the resistance of the current divider which installed and grounded on the 4 K stage. As a result, the DC current I_{sou} generated form the current source mainly goes through the current divider and is roughly 10 time reduced when I_{sam} gets to the sample. As a result, it benefits the experiment, because the noise from the current source is also reduced by a factor of 10 too.

The time-domain setup shown in Fig. 4.5 b) is more complicated than the spectroscopy setup. But the main idea is to drive and measure the qubit with a single pulse rather than a continuous microwave that used in the spectroscopical measurement. Instead of the VNA, the readout devices are two I-Q mixers having a mutual local oscillator and connected to a pair of DACs and ADCs separately.

4.2 Single qubit measurement

Of course, as discussed before, the 8-qubit is the most attractive and I indeed devote more effort to it. However, performing the measurement on the single-qubit chip is a necessary step. Due to its simplicity, it is completely predicable and explained very well by the Jaynes-Cummings model. Thus, I am able to exam the quality of the resonator, and all parameters of the qubit. Since the single-qubit chip has identical resonator and qubit design with the 8-qubit chip, and they are fabricated at the same time, the result of the measured single-qubit chip provides trustworthy reference to the experiments on 8-qubit chip. In our experiment, single-tone measurement is performed to identify the resonator, while the two-tone measurement identifies the property of the qubit. Time-domain measurement is done on this sample too.
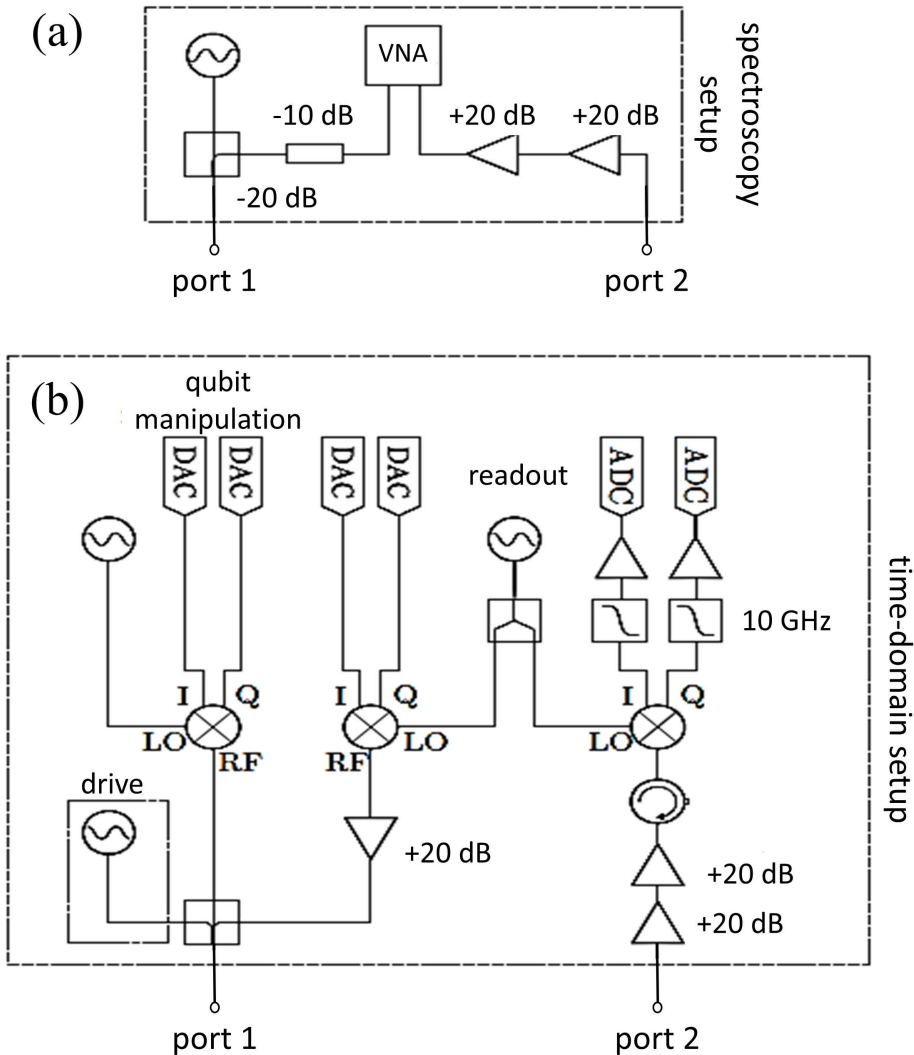
Figure 4.5: (Color online) Wiring and equipment employed in the measurement at room-temperature. (a) The spectroscopical setup. The VNA is used to do the 2-port network measurement. The microwave coming out of the VNA is attenuated by a $-10\ dB$ attenuator, and then combined with the signal from the microwave generator with a directional coupler. The coupler gives additional $-20\ dB$ attenuation for the signal form the VNA. The signal coming out of the fridge is sent into port 2 of the VNA through 2 room-temperature amplifiers which should have $+20\ dB$ magnifying factor. The microwave generator is switched off during the measurement on the resonator, its function is to drive the qubit when probing the transition frequency of the qubit. (b) The time-domain setup. The main idea is to drive and measure the qubit with a single pulse rather than a continuous microwave that used in the spectroscopical measurement. The scheme is explained in Fig. 4.5 b. Instead of the VNA, the readout tool is now two mixers having a mutual local microwave reference and connected to a pair of DACs and ADCs separately.

4.2.1 Single-tone experiment

The system of a resonator coupling to a single qubit is fully described by the Jaynes-Cummings model with the Hamiltonian in Eq. 2.29. Consider the multiple attenuations in the wiring showed in the previous section, the total attenuation is -120 dB. The lowest power reaching the sample is reduced to -140 dBm. The equation for calculating the average photon number is

$$\langle n \rangle = \frac{4P_{in}}{\hbar \omega_r^2} \cdot \frac{Q_L^2}{Q_c}. \tag{4.1}$$

According to this equation, the average photon number is 0.2, namely only the single excitation ($n = 1$) is considered for this system. Thus the eigen energy levels are written as

$$E_{\pm} = \hbar \omega_r + \hbar \omega_{01} \pm \frac{\hbar}{2} \sqrt{4g_{01}^2 + \Delta^2}, \tag{4.2}$$

where $\Delta = \omega_{01} - \omega_r$, is the detuning between the first two levels of the qubit and the resonator. The transition frequency of the first two levels of the transmon qubit is calculated by Eq. 2.27. Consider the Josephson energy is controlled by the external flux as $E_J = E_{J_{max}} |\cos(\pi \Phi / \Phi_0)|$, the frequency of the qubit is in the following form:

$$f_{01}(\Phi) = \frac{\sqrt{8E_{J_{max}} |\cos(\pi \Phi / \Phi_0)| E_C} - E_C}{2\pi \hbar}. \tag{4.3}$$

The external phase Φ in our work is controlled by the biasing current, thus, replace the phase terms with current items in Eq. 4.3 and substitute it into Eq. 4.2, one gets the dependence of the frequencies of the dressed system on the bias current

$$f_{\pm}(I_{bias}) = f_r + \frac{1}{4\pi\hbar} \sqrt{8E_{J_{max}} E_C \left| \cos\left(\pi \frac{I_{bias}}{I_{period}} - \theta_{off}\right) \right|} - \frac{E_c}{2\pi\hbar}$$

$$\pm \sqrt{4g_{01}^2 + \left(\frac{1}{4\pi\hbar} \sqrt{8E_{J_{max}} E_C \left| \cos\left(\pi \frac{I_{bias}}{I_{period}} - \theta_{off}\right) \right|} - \frac{E_c}{2\pi\hbar} - f_r\right)^2}. \tag{4.4}$$

Here I_{period} is the period of the bias current corresponding to a flux quantum. θ_{off} corresponds to the offset per period. Fig. 4.6 shows the plotting of the two eigen frequencies of Eq. 4.4 based on the theoretical parameters in Table 4.1. The maximum of f_+ equals to the maximum frequency of the qubit $f_{01_{max}}$ which is decided by $E_{J_{max}}$ and E_C. The minimum splitting between the two frequencies is decided by the coupling strength by $2g_{01}$.

In order to observe the anti-crossing of the coupled system, a spectroscopic single-tone experiment is done on this single-qubit chip employing the VNA as the driving
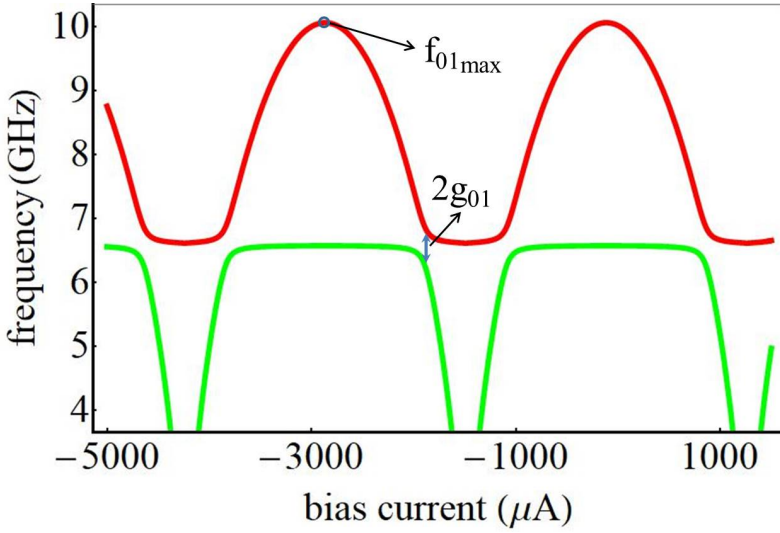
Figure 4.6: (Color online)Plot of $f_\pm$ in Eq. 4.4. The maximum of f_+ equals to the maximum frequency of the qubit f_{01max} which is decided by E_{Jmax} and E_C. The minimum splitting between the two frequencies is related to the coupling strength by $2g_{01}$.

and probing device. The measured data of observing the frequency window around the basic model of the resonator while tuning the bias current is shown in Fig. 4.7 a. The data is fitted by Eq. 4.4 with the colored lines as in Fig. 4.6, and the parameters are presented in Table 4.1. In order to see more period within short measurement time, frequency range of this figure is only 70 MHz, as a result the gradient lines look like vertical. The anti-crossing is clearly measured in Fig. 4.7 b which zooms in at the anti-crossing window while scans a wider frequency range of 250 MHz. The other parameters extracted from the fitting are the same, except for that the offset is a little bit different. It is reasonable because the mixture of the dilution union needs to be recondensed about every 14 days during experiments. The offset may change as the temperature increases and reduces during this procedure.

	f_r (GHz)	f_{01max} (GHz)	g_{01} (GHz)	$E_{Jmax}/2\pi\hbar$ (GHz)	$E_C/2\pi\hbar$ (GHz)	I_{period} (μA)	θ_{off}
theory	6.600	10.031	0.300	34	0.4	2750	3.010
Fig. 4.7 a	6.629	10.031	0.115	34	0.4	2730	3.010
Fig. 4.7 b	6.629	10.031	0.115	34	0.4	2730	2.995

Table 4.1: Parameters of the single qubit chip .
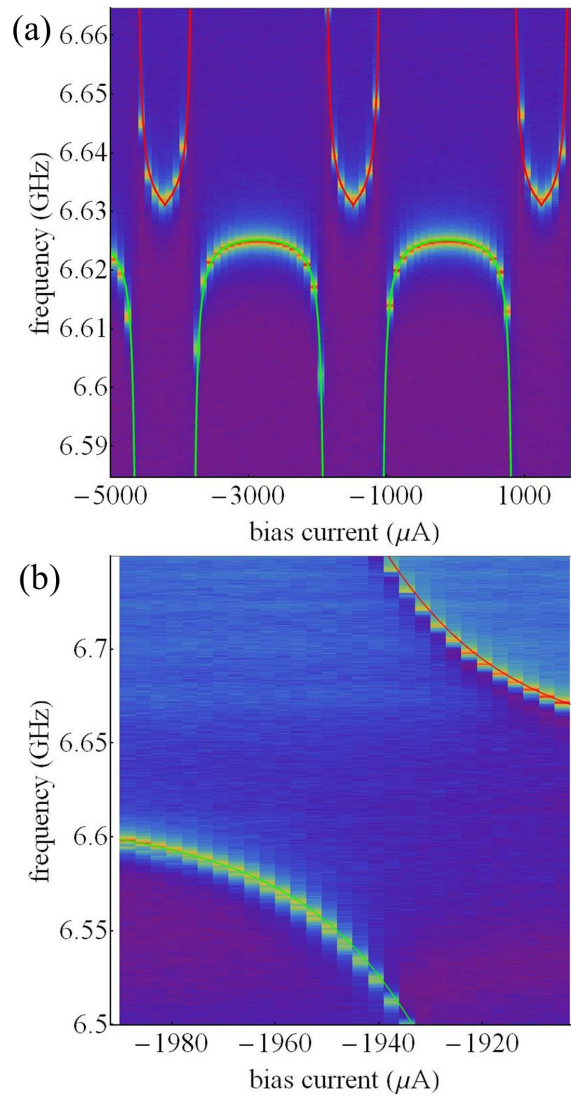
Figure 4.7: (Color online) The measured data of observing the frequency window around the basic model of the resonator while tuning the bias current. (a) The data with a frequency window of 70 *MHz* around the resonator frequency, to see more period with fewer data points. (b) The data of measurement on one single anti-crossing with 250 *MHz* frequency window. The parameters extracted from fitting of both pictures are listed in Table. 4.1

4.2.2 Two-tone experiment

Readout of the qubit is realized by working in the dispersive regime as discussed in Sec. 2.4.3. In experiment, I tune the bias current to the value corresponding to half a flux quantum, i.e. the sweet spot of the qubit. So that the qubit has the least sensitivity to flux noise and is far detuned from the resonator. Thus the resonator is employed as the readout tool of the qubit working in the dispersive regime.

The system is then probed by the VNA with a second tone (namely the microwave generator shown in Fig. 4.5 a) driving the qubit. As discussed in Sec. 2.4.3, according to the interaction of the resonator and the qubit in the dispersive limit, the resonator has a frequency of $\omega_r + \chi_{01} - \chi_{12}$ when the qubit is not excited. Once the driving microwave hits the transition frequency of ground stat to the first excited state of the qubit, the qubit gets excited, and the frequency of the resonator shifts to $\omega_r - \chi_{01}$. Picking out the most sensitive point of the Lorentz-shaped resonator as the measure point, and drive the qubit with proper power, the fundamental transition of the qubit from ground state to the first excited state is detected.

Fig. 4.8 a) shows the curve of the fundamental transition frequency of the qubit with respect to the current, employing the parameters obtained from the fitting in Fig. 4.7 a) (only the offset is different). Fig. 4.8 b) shows a plot of the measured qubit frequency for different bias current values within the measurement window illustrated by the green frame in figure a). The red squares are the measured values. The black dashed line is the same as in figure a. Here the power of the driving microwave is set to low value to ensure the single-photon driving. The maximum of f_{01} is measured to be 10.030 GHz when bias current is -150 μA.

According to Ref. [Bra+15], since the transmon qubit has limited anharmonicity, the higher levels could also be excited by multiple photon transition. Fig. 4.9 b) illustrate the process of multi-photon transition. 2 photons with the frequency of $\omega_{02}/2$ will drive the qubit from ground state to the second excited state, and similarly the higher levels are reached. Of course the higher the level, the larger the shift of the resonator is. By keeping the qubit around its maximum frequency and scanning over the driving microwave frequency of the qubit while increasing the power of the microwave source, one observes the result shown in Fig. 4.9 a). Higher transitions start to show up when the power goes up. It is worth noticing that the value of the power here is the power of the microwave source. The power reaches the chip is much lower because of the attenuation (-105 dB) of the wiring showed in the measurement setup. This measurement is important. It tells us up to which driving power only the basic transition is excited, i.e. the qubit is treated as a 2-level system. What's more, the anharmonicity of the transmon qubit could be calculated based on the high power measurement.
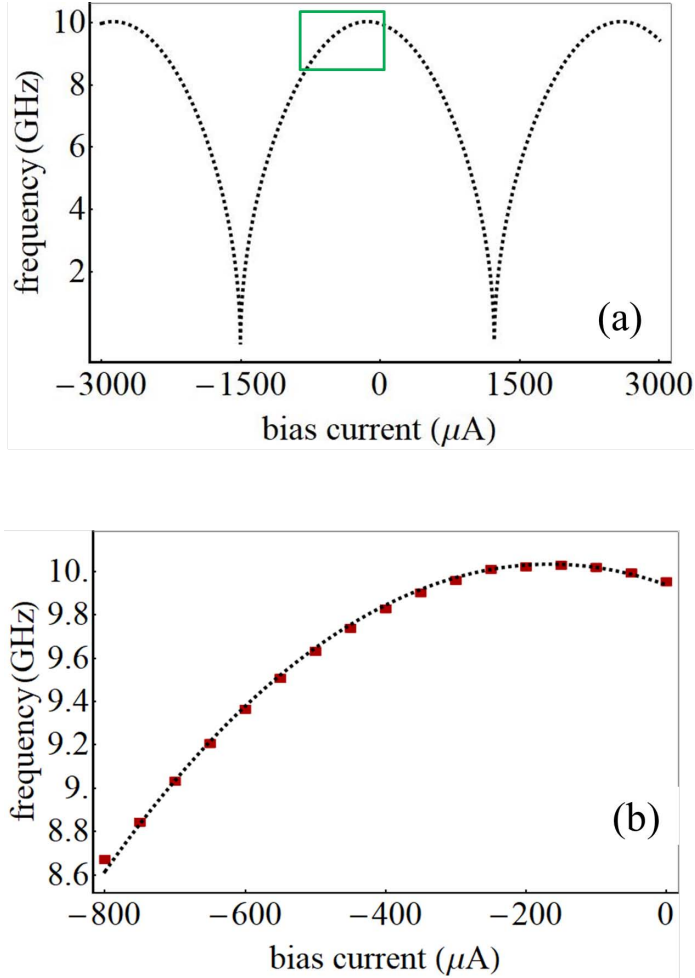
Figure 4.8: (Color online) Qubit frequency predication and measurement. (a) The curve of the fundamental transition frequency of the qubit with respect to the current employing the parameters obtained from the fitting in Fig. 4.7. Only the offset is changed to 2.98. (b) A plot of experiment of the qubit frequency for different bias current values within the measurement window illustrated by the green frame in figure a. The red squares are the measured qubit frequencies. The black dashed line is the same as in figure a. Here the power of the driving microwave is set to low value to ensure the single-photon driving. The maximum of f_{01} is measured to be 10.030 GHz when bias current is -150 μA.
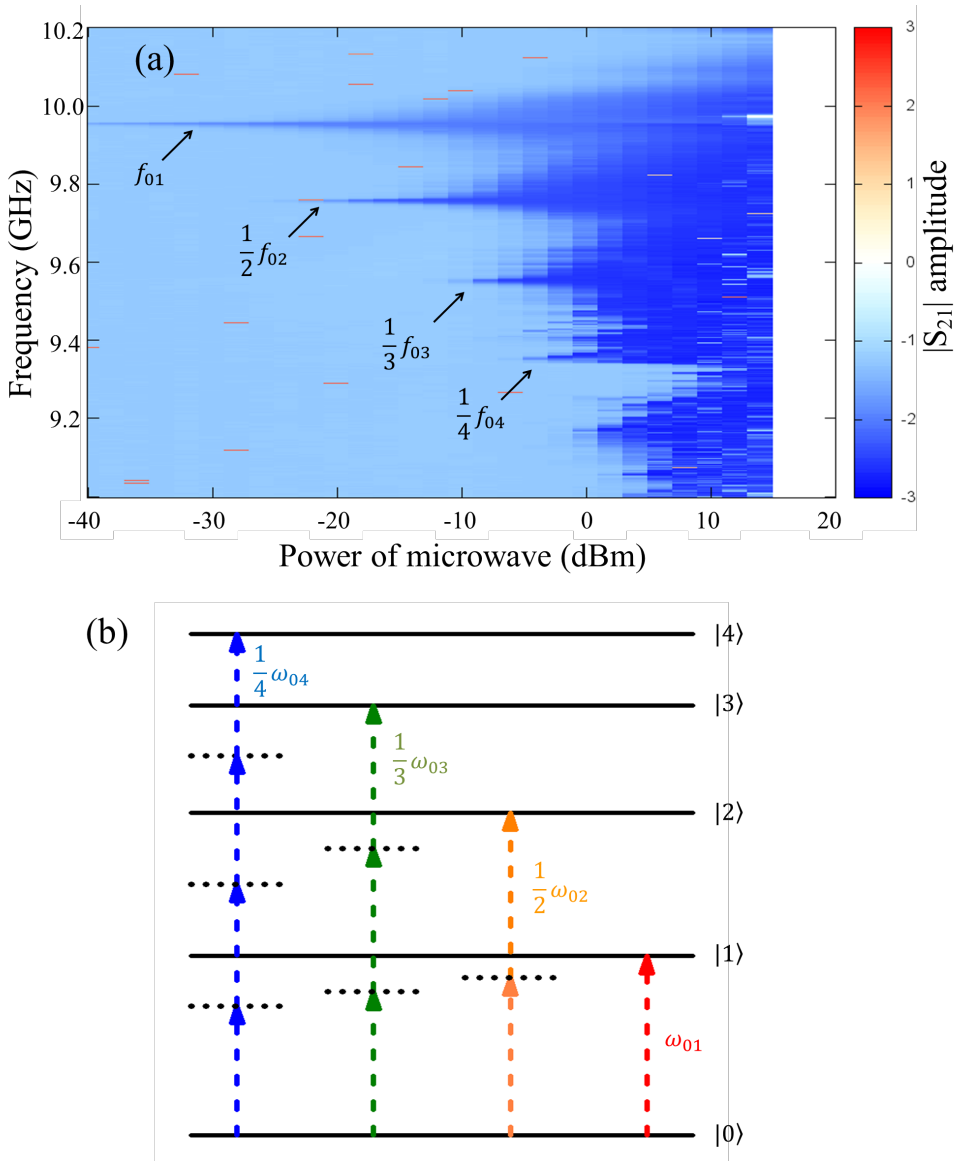
Figure 4.9: (Color online) Multiple photon transition. (a) Keeping the qubit around its maximum frequency and scanning over the driving microwave frequency of the qubit while increasing the power of the microwave source, one observes multi-photon transition experimentally. (b) The process of multi-photon transition on the level-ladder of transmon qubit.
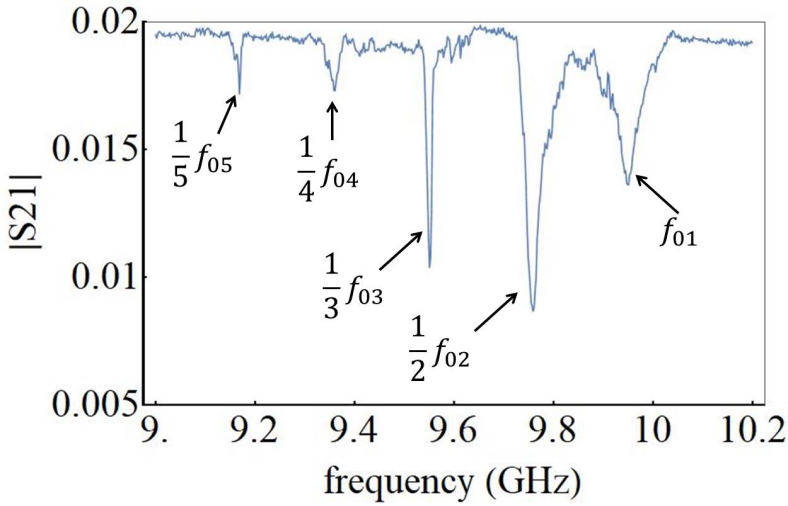
Figure 4.10: (Color online) Measurement on the qubit frequency with high microwave source power. 5 transitions are visible. The transition frequencies of each neighboring levels are calculated. The mean anharmonicity is 386 *MHz*.

Fig. 4.10 is the measurement of qubit transition frequencies done with the power of the microwave source at -10 *dBm*. Since it is only a single trace, taking smaller step-length of the microwave frequencies for a better resolution is achievable. The transition frequencies obtained from this measurement are listed in Table 4.2. The transition frequencies of each neighboring levels are calculated. The mean anharmonicity is 386 *MHz*.

f_{01} (GHz)	f_{02} (GHz)	f_{03} (GHz)	f_{04} (GHz)	f_{05} (GHz)
9.948	19.514	28.653	37.436	45.84
	f_{12} (GHz)	f_{23} (GHz)	f_{34} (GHz)	f_{45} (GHz)
	9.566	9.139	8.783	8.404

Table 4.2: Parameters of the single qubit chip .

4.2.3 Time-domain measurement

In order to measure the life time (T_1) of the qubit, the time-domain setup shown in Fig. 4.5 b is employed. The first thing to do is to find the correct microwave pulse corresponding to a π pulse which rotates the qubit from stat $|0\rangle$ to $|1\rangle$ on the Bloch sphere. Fig. 4.11 (a) shows this process. A sequence of microwave pulses
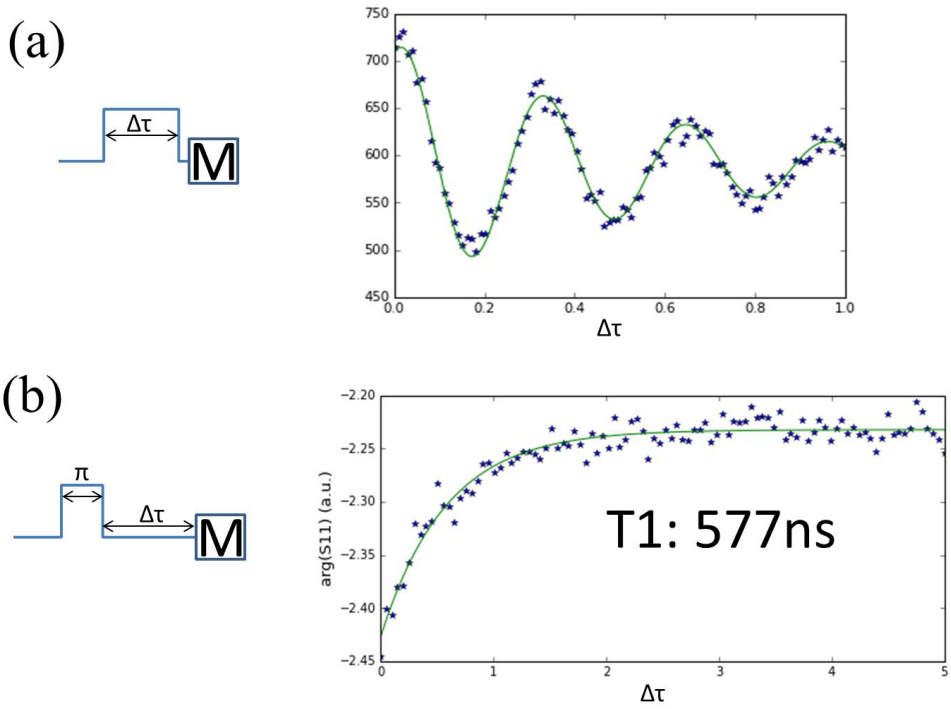
Figure 4.11: (Color online) Illustration of time-domain measurement. (a) How the π pulse is defined. A sequence of microwave pulses with different durations is applied on the qubit, right after each pulse the qubit is measured and has enough relaxing time before the next pulse. A damped Rabi oscillation between the ground state and the first excited state is observed. From the period of the oscillation, the π pulse is determined to be 155.7 *ns*. (b) The measurement of the life time of the qubit. π pulse is applied to the qubit, and the waiting time before measurement $\Delta\tau$ is extended for each measuring sequence, an exponential decay is observed. From this result, the life time of the qubit is obtained to be 577 *ns*.

with different durations is applied on the qubit, right after each pulse is measured and has enough relaxing time before the next pulse. A damped Rabi oscillation between the ground state and the first excited state is observed. From the period of the oscillation, the π pulse is determined to be 155.7 *ns*.

When the qubit is at the ground state, apply the π pulse on it, and measure directly after the pulse, the qubit is found to be at the excited. Give it enough time to relax to the ground state and extend the waiting time $\Delta\tau$ before measurement for each measuring sequence, the exponential decay is observed. From this result, the life time of the qubit is obtained to be 577 *ns*.
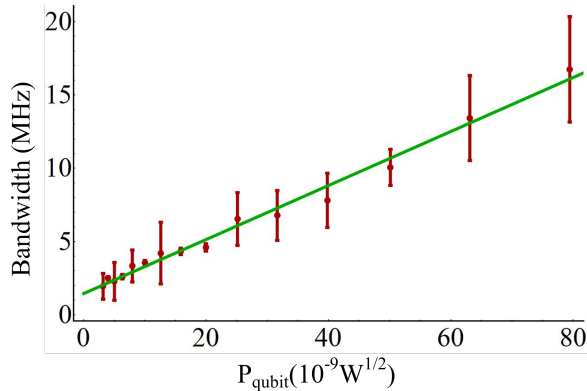
Figure 4.12: (Color online) Bandwidth of the dip for the qubit transition frequency, which is extracted by fitting the dip with Lorentz function. The data points are fitted to a linear function. T_2 is calculated according to the bandwidth at zero power.

As shown in Fig. 4.10, the measured qubit frequency shows a Lorentz-shaped dip, which broadens if the driving power P_{qubit} of the qubit is increased [Lis08]. According to Ref. [Abr61], the bandwidth σ depends linearly on $\sqrt{P_{qubit}}$. The data of f_{01} for different driving power shown in Fig. 4.9 a) is fitted with a linear function, and the result is shown in Fig. 4.12.

According to the linear fitting, the bandwidth at zero power is obtained $\sigma_0 = 1.450$ MHz. It corresponds to the dephasing time of the qubit

$$T_2 = \frac{1}{\pi \sigma_0} = 220 ns. \tag{4.5}$$

4.3 Fano-shaped resonator

The microwave resonator is very important, since it is commonly used to probe and readout the superconducting qubits dispersively coupled to it. Based on the wiring of our measurement setup, transmission and reflection data could be taken during the same cooldown of the dilution refrigerator. Theoretically, through such an in-line CPW resonator, the transmission is supposed to be peaked in the vicinity of the resonance [Göp+08] for any photon numbers. However, in our experiments I experimentally observe an arbitrary Fano-shaped resonance in the transmitted amplitude of the resonator as a function of frequency. The shape of the Fano resonance can be tuned substantially with DC biasing of control lines, and shows a

smooth transition between peak and dip while scanning over the current. In most cases, a dip is observed, rather than a peak.

For the purpose of understanding the observed effects physically, with the help of Dr. Juha Leppäkangas, a theoretical model [Lep+] is established on the basis of microwave propagation in open transmission lines with boundary conditions which represent the microwave resonator and its coupling to the background. Within this model, an interference effect is explained with a transmission of microwave in parallel and the dynamics of the multiple qubits.

The benefit of simplified feature is that the complete system of the resonator and multiple qubits has a changeless equation of motion, so that the Fano interference could be solved straightforwardly employing a solution for the cavity obtained beforehand. Such as the solution based on the simulation of the master equation and an additional linear boundary conditions accounting for the presence of the background. I study further in details the form of the Fano resonance and the information it can carry in several considerations, such as dissipation, heating, and system nonlinearity.

A drastic variation of the shape for the transmission spectra is observed when the decoherence of the qubits is enhanced because of the incoherent hopping of the qubit states or decay of the cavity. Such kind of decoherence in our system is caused by the local heating originating from the DC current running through the bias lines next to the qubits. Due to the design, the coupling strength between the bias line and the center conductor of the resonator is not negligible, because it needs to be so close to the qubit, so that to realize effective control of the qubit with small current, which in turn reduces the heating effect. As a result, the feeble background dissipation of the resonator transmits through the bias lines due to the cross talk. However, even with a strong noise which comparable with the bandwidth of the resonator, the microwave CPW resonator is still able work as the readout tool. No matter the shape of the resonator is a peak or a dip, the Jaynes-Cummings energy levels can be detected from its position, despite the Fano resonance [Lep+] changes with temperature and the decoherence strength. The results basically show it is important to consider the cross talk in such kind of superconducting microwave circuit and the Fano resonance can be employed to probe the system.

4.3.1 Theoretical model of the system

In this part I introduce the classical and the quantum models respectively for the system for multiple qubit coupled to a mutual cavity bus. For starters, I introduce a classical model in which the microwave scatters in a parallel channel (background).

Secondly, the model is quantized without the parallel transport. I demonstrate afterwards how to include the parallel transmission in the quantized model, i.e. by adding corresponding terms in the boundary conditions of the microwave.

Model of linear scattering

For the classical model of microwave scattering, microwave radiation in a pair of semi-infinite transmission lines connected by the same boundary is considered. It can be described by lumped circuit elements. The equivalent circuit is shown in Fig. 4.13. This model could include the superconducting qubits, under the condition that they interact with the resonator only linearly, so that they could be treated as classic harmonic oscillators. The superiority of this strategy is all elements of the circuit could be represented by impedance. This means once the general solution is obtained, the investigation of different type of effective lumped-element circuit is straightforward. This strategy is also used to exam the reduced model later, which considers non-linear qubits, and shows correct results in the linear limit.

The scattering properties are derived by requiring that at the end of the transmission lines, the voltages and currents match the relation between them which is implied by the impedances of the system. The first thing to do is to identify the total voltage and current considering the in and out propagating fields at the both ends of the cavity as shown in Fig. 4.13. For the voltage and current, according to Ref. [Poz09], one obtains

$$\begin{cases} V^L = V_{in}^L + V_{out}^L, \\ V^R = V_{in}^R + V_{out}^R, \\ I^L = \dfrac{V_{in}^L - V_{out}^L}{Z_0}, \\ I^R = -\dfrac{V_{in}^R - V_{out}^R}{Z_0}. \end{cases} \tag{4.6}$$

The variables here are the Fourier components of the total propagating field (for example, $V^L = V^L(\omega)$). The opposite sing of the two equations for current is due to the difference in definition of propagating direction on the two sides. The out-fields can then be solved as a function of in-fields by using Kirchhoff rules of the cavity with two sides.

In order to illustrate our approach, a good start is to consider the case of bare parallel impedance, i.e. C_{c1} and C_{c2} are both zero. Two boundary conditions must be

a)

b)
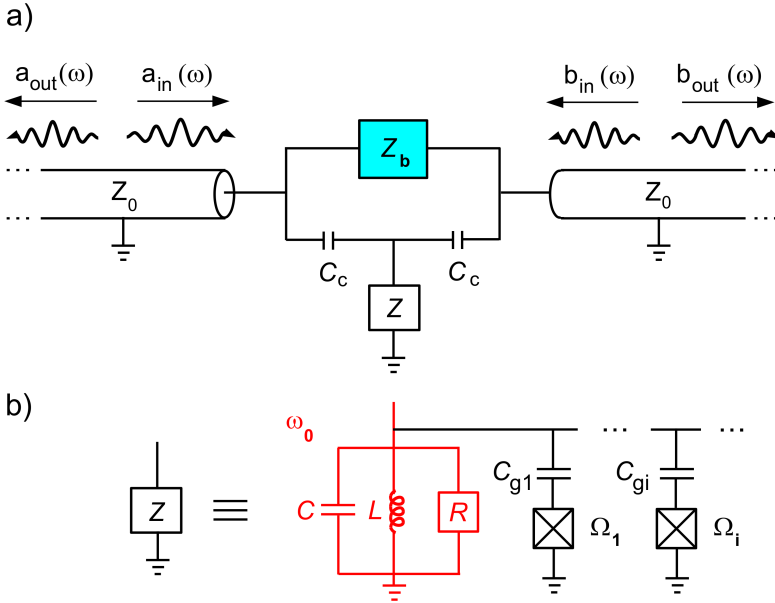
Figure 4.13: (Color online) The equivalent circuit [Lep+]. (a) The incoming and outgoing microwave fields propagating in the semi-infinite transmission lines (impedance Z_0) on two sides of the resonator. The propagating fields couple with the cavity field through capacitors C_{c1}, C_{c2} and directly to each other through impedance Z_p. (b) The cavity is modeled as a parallel LC resonator [Göp+08] and its internal dissipation can be included by resistor R. (c) The cavity is coupled through a capacitor C_g to a superconducting qubit (crossed box), or similarly to a set of superconducting qubits (through capacitances C_{gi}).

satisfied [Lep+], which means the current conserves and the voltage drops across the impedance Z_p,

$$\begin{cases} \dfrac{V_{in}^L - V_{out}^L}{Z_0} = -\dfrac{V_{in}^R - V_{out}^R}{Z_0}, \\[2mm] Z_p \dfrac{V_{in}^L - V_{out}^L}{Z_0} = (V_{in}^L + V_{out}^L) - (V_{in}^R + V_{out}^R). \end{cases} \tag{4.7}$$

It simplifies the equations to assign $V_{in}^R = 0$, because in real experiment there is microwave input into one end (the left side in our case) of the resonator, no matter it is transmission or reflection measurement. Thus the solution is derived to be [Lep+]

$$\begin{cases} V_{out}^L = \dfrac{1}{1 + 2Z_0/Z_p} V_{in}, \\[2mm] V_{out}^R = \dfrac{2Z_0/Z_p}{1 + 2Z_0/Z_p} V_{in}^L. \end{cases} \tag{4.8}$$

Analogously, under the condition that Z_{c1} and Z_{c2} are not zero but arbitrary impedances with the form $Z_{c1} = (i\omega C_{c1})^{-1}$ and $Z_{c2} = (i\omega C_{c2})^{-1}$, the boundary conditions could be constructed. Considering the Kirchhoff equations for the input and output fields and the voltage on the island between C_{c1} and C_{c2}, it is straightforward to calculate the solution. With the same assumption that $V_{in}^R = 0$, the equation set is

$$
\begin{pmatrix}
\frac{1}{Z_0} + \frac{1}{Z_{c1}(\omega)} + \frac{1}{Z_p(\omega)} & -\frac{1}{Z_{c1}(\omega)} & -\frac{1}{Z_p(\omega)} \\
-\frac{1}{Z_{c1}(\omega)} & \frac{1}{Z(\omega)} + \frac{1}{Z_{c1}(\omega)} + \frac{1}{Z_{c2}(\omega)} & -\frac{1}{Z_{c2}(\omega)} \\
\frac{1}{Z_p(\omega)} & \frac{1}{Z_{c2}(\omega)} & -\frac{1}{Z_0} - \frac{1}{Z_{c2}(\omega)} - \frac{1}{Z_p(\omega)}
\end{pmatrix}
\begin{pmatrix}
V_{out}^L \\
V_{out}^R
\end{pmatrix} =
$$

$$
\begin{pmatrix}
\frac{1}{Z_0} - \frac{1}{Z_{c1}(\omega)} - \frac{1}{Z_p(\omega)} \\
\frac{1}{Z_{c1}(\omega)} \\
-\frac{1}{Z_p(\omega)}
\end{pmatrix} V_{in}^L.
$$

(4.9)

The output fields and the voltage on the island between C_{c1} and C_{c2}, as a function of the input (V_{in}^L), could easily be calculated by inverting the matrix. Assuming the coupling on the ends of the resonator is symmetric, i.e. $C_{c1} = C_{c2} = C_c$, one obtains the analytical solution [Lep+]

$$
\begin{cases}
\dfrac{V_{out}^L}{V_{in}^L} = \dfrac{2Z_0[Z_c^2 + Z(2Z_c + Z_p)]}{(2Z + Z_0 + Z_c)[Z_0(2Z_c + Z_p) + Z_c Z_p]}, \\
\dfrac{V_{out}^R}{V_{in}^L} = \dfrac{Z_c Z_p(2Z + Z_c) - Z_0^2(2Z_c + Z_p)}{(2Z + Z_0 + Z_c)[Z_0(2Z_c + Z_p) + Z_c Z_p]}.
\end{cases}
$$

(4.10)

As defined in the 2-port network analyze, the reflection (S_{11}) and the transmission (S_{21}) are the ration between the output and input field, namely

$$
S_{11}^* = \frac{V_{out}^L}{V_{in}^L},
$$

$$
S_{21}^* = \frac{V_{out}^R}{V_{in}^L},
$$

(4.11)

I tacitly approve that there is no input from the right side of the resonator.

Quantization of the model

It is systematical to start with a Lagrangian approach when quantizing various open microwave circuits. In this part, I summarize the results of the Lagrangian approach applied to our system. To start with, I consider the case that the cavity is driven in the

absence of parallel transmission ($Z_p \rightarrow \infty$). Different from the impedance approach that is talked about above, the model discussed now also includes non-classical interaction among the cavity and superconducting 2-level systems.

The basic idea is to deal with the coupled system(the resonator and the artificial atoms coupled to it) and the transmission line separately, while consider their interaction by adding linear boundary conditions. This approach is proved to be valid for high quality-factor (high-Q) cavities and usual cavity-qubit coupling (below ultra-strong coupling regime). Thus, the cavity is treated separately, and described by the Hamiltonian of an harmonic oscillator,

$$\hat{H}_0 = \hbar \omega_0 \hat{a}^\dagger \hat{a}, \tag{4.12}$$

where $\hat{a}$ and $\hat{a}^\dagger$ are the annihilation and creation operators. The coupling normalized resonance frequency is

$$\omega_0 = \frac{1}{\sqrt{L(C + 2C_c)}}, \tag{4.13}$$

where C_c is the capacitance of each end of the symmetric resonator, namely $C_{c1} = C_{c2} = C_c$.

Considering the boundary conditions at both sides of the resonator [WM08], the interaction between the resonator and the semi-infinite transmission lines is obtained. On the left side,

$$\hat{a}_{out}(t) = \sqrt{\gamma} \hat{a}(t) - \hat{a}_{in}(t). \tag{4.14}$$

And on the right side,

$$\hat{b}_{out}(t) = \sqrt{\gamma} \hat{a}(t) - \hat{b}_{in}(t). \tag{4.15}$$

The operators in these two equations are time-dependent because it is in the Heisenberg picture. The operator $\hat{a}_{in}(t)$ ($\hat{a}_{out}(t)$) annihilates an incoming (outgoing) photon at the left side at time t. The definitions are similar for the operators $\hat{a}_{in}(t)$ and $\hat{a}_{out}(t)$ of the right hand side. These four operators have the commutation relations

$$\left[\hat{a}_{in}(t), \hat{a}_{in}^\dagger(t') = \delta(t - t') \right],$$
$$\left[\hat{b}_{in}(t), \hat{b}_{in}^\dagger(t') = \delta(t - t') \right]. \tag{4.16}$$

The same relations ought to be valid for the output field (which is solved as a function of input field). According to Ref. [PS95], the decay rate is described by the following equation

$$\gamma = \left(\frac{C_c}{C + 2C_c} \right)^2 \frac{Z_0}{Z_{LC}} \omega_0, \tag{4.17}$$

here $Z_{LC} = \sqrt{L/(C + 2C_c)}$ is the characteristic impedance of the resonator. For a common condition that Z_{LC} is comparable with Z_0, aiming for a quality factor much larger than 1 leads to $C \gg C_c$. Finally, the operators of the cavity field satisfy the following Heisenberg equation of motion [WM08]

$$\dot{\hat{a}}(t) = \frac{i}{\hbar} \left[\hat{H}_0, \hat{a}(t) \right] - \gamma \hat{a}(t) + \sqrt{\gamma} \left[\hat{a}_{in}(t) + \hat{b}_{in}(t) \right] \qquad (4.18)$$

Under the similar assumption that there is a coherent input from the left side of the resonator with frequency ω while there is no input at all from the right side, the function of reflection and transmission having the following form should be solved [Lep+]

$$\begin{aligned} S_{11} &= \frac{\langle \hat{a}_{out}^L \rangle}{\langle \hat{a}_{in}^L \rangle}, \\ S_{21} &= \frac{\langle \hat{b}_{out}^R \rangle}{\langle \hat{a}_{in}^L \rangle}. \end{aligned} \qquad (4.19)$$

The way to solve these equations is to solve the output field as a function of input field under the boundary conditions described by Eq. 4.14 and Eq. 4.15, as well as the Heisenberg equation of motion shown in Eq. 4.18. A straightforward comparison between this approach and the impedance approach concerning the scattering properties is shown in Fig a direct comparison to the scattering properties obtained by the impedance approach can be done, and is shown in Fig 4.14

Employing the single-mode treatment, one is able to consider the interaction between the microwave cavity and the qubits as well. The cavity interacts with the qubit through C_{gi} as illustrated in Fig. 4.13 c. For an isolated cavity interacting with n-qubits, the system is described by the Tavis-Cummings Hamiltonian discussed before

$$\hat{H}_0 = \hbar \omega_0 \hat{a}^\dagger \hat{a} + \sum_{i=1}^{n} \frac{\Omega_i}{2} \hat{\sigma}_z^i + g_i \sum_{i=1}^{n} (\hat{a}^\dagger \hat{\sigma}_-^i + \hat{a} \hat{\sigma}_+^i). \qquad (4.20)$$

And the boundary conditions and Heisenberg equations of motion have the same form as before (under the assumption of $g_i \ll \omega_i$). By representing the qubit a parallel inductor L_i and capacitor C_i, the strength of interaction is approximated to be

$$g_i = \sqrt{\omega_0 \Omega_i} \frac{C_g}{\sqrt{CC_i}}, \qquad (4.21)$$

where $\Omega_i = 1/\sqrt{L_i(C_i + C_{gi})}$. Here it is assumed $C_g, C_c \ll C, C_i$. The energy of the oscillator is renormalized to $\omega_0 = 1/\sqrt{L(C + 2C_c + \sum_i C_{gi})}$.
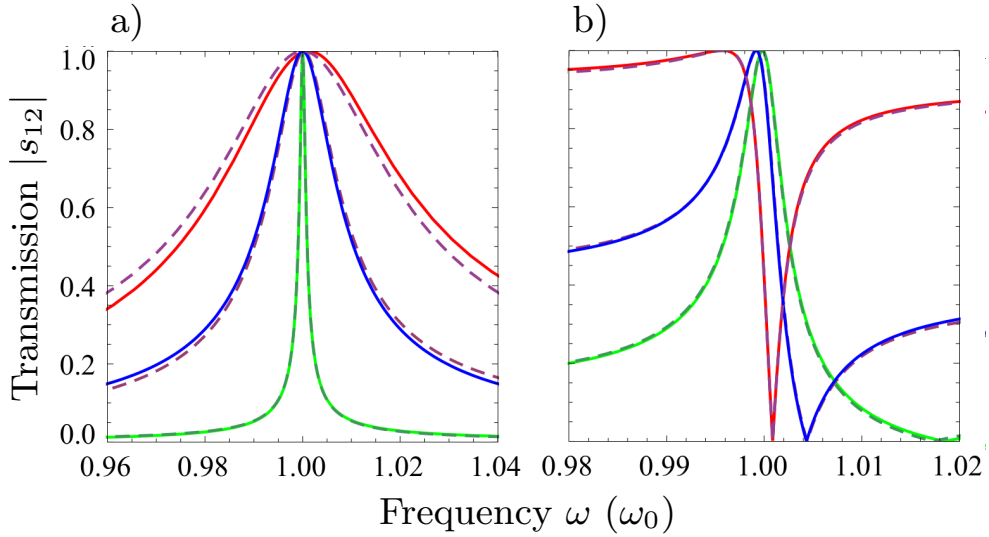
Figure 4.14: (Color online) S_{21} amplitude transmitted through a linear resonator [Lep+]. The results of impedance approach (dashed lines) and the single-mode approach (solid lines) are compared. The resonator is represented by a LC oscillator as shown in Fig. 4.13. (a) The transmission without the background transmission, with $C_c/C = 0.05, 0.2, 0.4$ respectively for the impedance approach, namely the off-resonance transport increases simultaneously. In the single-mode treatment it corresponds to $\gamma/\omega_0 \times 10^3 = 0.5, 8, 32$. The comparison proves that the single-mode treatment is a good approximation and becomes more accurate if C_c gets much smaller than C. (b) The transmission amplitude with increasing transmission through the background for $C_c/C = 0.1$. $\epsilon = 0.05, 0.2, 1.0$ corresponds to different off-resonance transmission. One notices that the single-mode treatment is a good approximation for all cases. For both figures, it is assumed there is no dissipation in the system.

In the dispersive limit ($g \ll |\Omega - \omega_0|$), the effective Hamiltonian is in the following form

$$\hat{H}_{eff} = \hbar \left(\omega_0 + \frac{g^2}{\Delta} \hat{\sigma}_z \right) \hat{a}^\dagger \hat{a} + \frac{\hbar}{2} \left(\Omega_0 + \frac{g^2}{\Delta} \right) \hat{\sigma}_z, \tag{4.22}$$

where $\Delta = \Omega - \omega_0$ is the detuning between the resonator and the qubit. The system now behaves as a harmonic oscillator, and the resonance frequency is decided by the state of the qubit.

Consider the background

The model discussed above is generalized to the case considering a parallel transition (explicitly a parallel inductor) in this part. The parallel capacitor is not important as it only changes the sign of the obtained reactive term. By introducing an imaginary

part of this term, the corresponding boundary conditions shown in Eq. 4.14 and Eq. 4.15 are generalized using a Lagrangian approach [Lep+]

$$\hat{a}_{out}(t) = \sqrt{\gamma}\hat{a}(t) - \frac{1}{1+2i\epsilon}\hat{a}_{in}(t) - \frac{2i\epsilon}{1+2i\epsilon}\hat{b}_{in}(t),$$

$$\hat{b}_{out}(t) = \sqrt{\gamma}\hat{a}(t) - \frac{1}{1+2i\epsilon}\hat{b}_{in}(t) - \frac{2i\epsilon}{1+2i\epsilon}\hat{a}_{in}(t), \tag{4.23}$$

where a parameter which describes the reactive response of the parallel channel is introduced $\epsilon = Z_0/\omega_0 L_p = Z_0/|Z_p(\omega_0)|$. In the limit of $\epsilon \to 0$, one obtains the same equations as Eq. 4.14 and Eq. 4.15. What's more, a combination of $\gamma \to 0$ and $\hat{b}_{in} = 0$ gives the boundary conditions equivalent to Eq. 4.8. The Heisenberg equation of motion stays the same and is valid for all ϵ and γ which is much smaller than ω_0. The interference of the output field is calculated using Eq. 4.23. The result proves that the previous work for driven cavities [Bis+09] is achievable to be modified to describe the case of parallel transportation by applying the modified boundary conditions.

For linear cavities, the output field could be solved as a function of the input field by a Fourier transformation [WM08]. The solution is valid for a system consists of a cavity and a qubit which works in the dispersive limit, i.e. there is no transition of the qubit state, or the transition is so slow that can be represented by a statistical average over the frequencies of the resonator. Employing the Fourier transformation of the operator $\hat{a}(\omega) \equiv (1/\sqrt{2\pi}) \int \hat{a}(t)dt$,

$$\begin{pmatrix} \hat{a}_{out}(\omega) \\ \hat{b}_{out}(\omega) \end{pmatrix} = \frac{1}{(1+2i\epsilon)(1-2if)} \begin{pmatrix} 4\epsilon f - 1 & -2i(\epsilon+f) \\ -2i(\epsilon+f) & 4\epsilon f - 1 \end{pmatrix} \begin{pmatrix} \hat{a}_{in}(\omega) \\ \hat{b}_{in}(\omega) \end{pmatrix}, \tag{4.24}$$

where $f = f\omega = \gamma/2(\omega_0 - \omega)$. The amplitude of transmission and reflection are

$$S_{21} = \frac{\gamma + 2\epsilon(\omega_0 - \omega)}{(1+2i\epsilon)[\gamma + i(\omega_0 - \omega)]},$$

$$S_{11} = \frac{2\gamma\epsilon + \omega - \omega_0)}{(-i+2\epsilon)[\gamma + i(\omega_0 - \omega)]}. \tag{4.25}$$

When $\epsilon = 0$ (or $\gamma = 0$), it corresponds to the situation that the parallel transportation (or the resonator) has no contribution [Lep+]. A comparison of this model and the impedance approach is shown in Fig. 4.14 b. One notices that the reduced model works for all strengths of parallel transportation.

Introducing dissipation and master equation

The next thing to do is to introduce the dissipation of the resonator, the qubit and the parallel transmission lines, and the fluctuation caused by finite temperature. By

adding a negative imaginary term to ϵ (i.e. $i\epsilon$ changed into $i\epsilon + \epsilon_r$), one introduces phenomenologically a finite resistivity of the background. This approach is similar to how to introduce the dissipation in the impedance approach: by changing $Z_p(\omega)$ from $i\omega L_p\omega$ to $i\omega L_p\omega + Rp$, where R_p is a series resistor larger than zero. In order to add the dissipation of the resonator, it is similar that an imaginary term should be added to the resonance frequency. On the contrary, to consider the effect of finite temperature, formulate a master equation is more convenient. It is worth noticing that the finite temperature affects the field averagely. It should be considered only in nonlinear system (for example system that have qubits), because for linear system (for example the harmonic oscillator) the contribution averages out. Analogously, the thermal radiation emitted through the parallel transmission lines averages out when only the average field amplitude is considered.

By the assumption of a coherent input from the transmission line on the left side, our model can be described by a Lindblad master equation that includes the finite temperature in the transition of the system [WM08],

$$\dot{\rho} = \frac{i}{\hbar}[\hat{\rho}, \hat{H}] + \mathcal{L}_a[\hat{\rho}] + \mathcal{L}_b[\hat{\rho}] + \mathcal{L}_{int}[\hat{\rho}] + \sum_{i=1}^{n} \mathcal{L}_{qi}[\hat{\rho}], \tag{4.26}$$

where $\hat{\rho}$ is the reduced density matrix of the resonator-qubit system. The coherent Hamiltonian of the coupled system is

$$\hat{H} = \hat{H}_0 + \hat{H}_d, \tag{4.27}$$

where $\hat{H}_d = i\hbar\sqrt{\gamma_a}A(t)\hat{a}^\dagger + H.c.$ is the term for the incoming radiation from side a. $A(t) = \langle \hat{a}_{in}(t) \rangle$ and $\langle \hat{b}_{in}(t) \rangle = 0$. Consider the system in the rotating frame with respect to the drive frequency ω, one gets a Hamiltonian for the dispersive limit,

$$\hat{H} = \hbar\left(\omega_0 - \omega + \frac{g^2}{\Delta}\hat{\sigma}_z\right)\hat{a}^\dagger\hat{a} + \frac{\hbar}{2}\left(\Omega_0 + \frac{g^2}{\Delta}\right)\hat{\sigma}_z + \frac{\alpha}{2}(\hat{a}^\dagger + \hat{a}), \tag{4.28}$$

where $\alpha = 2i\hbar\sqrt{\gamma}A(t)e^{i\omega t}$ is a constant real number. The Lindblad super-operator $\mathcal{L}_a$ describes cavity transitions due to interaction with the transmission line on the left,

$$\mathcal{L}_a[\hat{\rho}] = \frac{\gamma_a^-}{2}(2\hat{a}\rho\hat{a}^\dagger - \hat{a}^\dagger\hat{a}\rho - \rho\hat{a}^\dagger\hat{a}) + \frac{\gamma_a^+}{2}(2\hat{a}^\dagger\rho\hat{a} - \hat{a}\hat{a}^\dagger\rho - \rho\hat{a}\hat{a}^\dagger). \tag{4.29}$$

Here the decay rate to the left side transmission line satisfies in thermal equilibrium [WM08] $\gamma_a^- = \gamma \times exp(\frac{\hbar\omega_0}{k_B t})/[exp(\frac{\hbar\omega_0}{k_B t}) - 1]$, and the corresponding thermal excitation rate $\gamma_a^+ = \gamma/[exp(\frac{\hbar\omega_0}{k_B t}) - 1]$. Similarly one gets $\mathcal{L}_b$ describing the interaction with the transmission line b ($\gamma_b^\pm = \gamma_a^\pm$). $\mathcal{L}_{int}$ describes the internal decoherence of the resonator, and the decoherence of the ith qubit is described by

$$\mathcal{L}_{qi}[\hat{\rho}] = \frac{\gamma_{qi}^-}{2}(2\hat{\sigma}_-^i\rho\hat{\sigma}_+^i - \hat{\sigma}_+^i\hat{\sigma}_-^i\rho - \rho\hat{\sigma}_+^i\hat{\sigma}_-^i) + \frac{\gamma_{qi}^+}{2}(2\hat{\sigma}_+^i\rho\hat{\sigma}_-^i - \hat{\sigma}_-^i\hat{\sigma}_+^i\rho - \rho\hat{\sigma}_-^i\hat{\sigma}_+^i). \tag{4.30}$$

For the internal decoherence of the resonator and qubit decoherence, the excitation and decay rates are in thermal equilibrium in the following form

$$\gamma^{\pm} = \frac{\mp J(\omega_0)}{1 - exp(pm\frac{\hbar\omega_0}{k_B t})},$$

(4.31)

with $J(\omega_0)$ the spectral density of the relevant dissipative environment.

The output (and the possible interference) could be solved by calculating $\langle \hat{a}(t) \rangle$, employing the master equation, and then applying Eq. 4.23, with Eq. 4.23.

4.3.2 Fano resonance

In this part, different forms of Fano resonances [Fan61] for microwave transmission are discussed theoretically considering a two-ended resonator with a parallel channel and the decoherence of the system is also included. The spectral form of a resonant system for a typical Fano resonance is asymmetric around the resonance frequency because of the interference of two scattering amplitudes. One is through a resonant system with a discrete energy-levels, the other one is through a background with a constant density of states. It is possible to characterize the Fano interference by the parameter q under the assumption that the scattering spectrum as a function of the drive frequency is in the following form

$$|S| \sim \frac{|q + \eta|}{\sqrt{1 + \eta^2}}, |s|^2 \sim \frac{(q + \eta)^2}{1 + \eta^2},$$

(4.32)

where $\eta = (\omega_0 - \omega)/(\gamma/2)$ is the broadening-normalized frequency. The response, (for example the amplitude of the transmitted microwave) is proportional to this (or a similar) equation. There are two important limits in this description, one is $q \rightarrow \infty$ which gives a Lorentzian shaped peak, while the other on is $q = 0$ which gives a Lorentzian shaped dip.

System without dissipation

For free resonator, which could be represented by a Jaynes- or Tavis-Cummings oscillator in the dispersive limit, the solution of S_{21} in Eq. 4.25 is employed to study the interference. The parameters ω_0 and ϵ are assumed to be positive real numbers(i.e. internal dissipation is not considered), so that the transmission probability is obtained [Lep+]

$$|s_{21}|^2 = \frac{1}{q^2 + 4} \frac{(q + \eta)^2}{1 + \frac{\eta^2}{4}} \propto \frac{(q + \eta)^2}{1 + \frac{\eta^2}{4}}$$

(4.33)

where $q = 1/\epsilon$. For the limit that $q \to \infty$ (i.e.$|Z_p(\omega_0)| \to \infty$), a Lorentzian shaped peak for the transmission is observed, which means there is no interference. On the other hand, for a finite q(i.e. finite parallel coupling), the interference plays a role. When $q = -\epsilon$, there is no transmission, because of perfect destruction. When q reaches the other limit which goes to zero, the response changes to a Lorentzian shaped dip. In the case of dissipation free system, a very strong parallel transportation is needed for this form of peak. All these limits could be seen in Fig. 4.14 b.

The direction of the tilt (namely the minimum location of the resonance frequency) in our case is always rightwards. And it depends generally on two elements. The first is the change of the phase from the input to output through the resonator. The second is the nature of the parallel coupling, whether it is coupled capacitively or inductively. The practical example is the CPW $\lambda/2$-resonator employed in our research, the phase of which at resonance is in the form of $V_{out}^R/V_{in}^L = (-1)^{n+1}$ for modes $n = 1, 2, ...$. Which means the first mode keeps the sign while the second mode switches the sign. What's more, the model based on a parallel resonator (see Fig. 4.13 b), inverts the sign at the resonance and equals to $n = 2, 4, ...$. However, the model based on a parallel resonator could describe odd modes as well, if inductive and capacitive parallel coupling are switched.

Dissipation through the resonator and the background

Till now, I prove that for a dissipation-free system with a weak parallel transportation, the transmission is always a tilted Lorentzian peak. Then I discuss about a resonator having a finite internal quality factor with dissipation through the parallel channel, which changes the form of the Fano resonance to a dip. Firstly, I study a linear resonator with no qubit hopping (working in the dispersive limit). The solution of Eq. 4.25 is valid. What's more, a finite internal quality factor could be included by adding a imaginary part to the frequency of the resonator $\omega_0 \to \omega_0 - i\omega_r$, a finite resistivity in the parallel channel could also be added a imaginary part to ϵ as $\epsilon - i\epsilon_r$

For starters I add only the cavity dissipation. The result obtained from the solution of Eq. 4.25 is shown in Fig. 4.15. As expected, the effect of the internal dissipation is reducing the transmission and 'straightens' the structure of the interference. The reflection dip changes similarly as shown in Fig. 4.16 a. Obviously, due to the radiation dissipated through the resonator, the reflection and transmission in total is smaller than the input.

Afterwards, the dissipation through the parallel channel is added. One notes that it is not achievable to obtain the asymmetric Fano shape without the reactive part in the parallel channel. Also, the resistivity of the parallel channel decreases the resonant
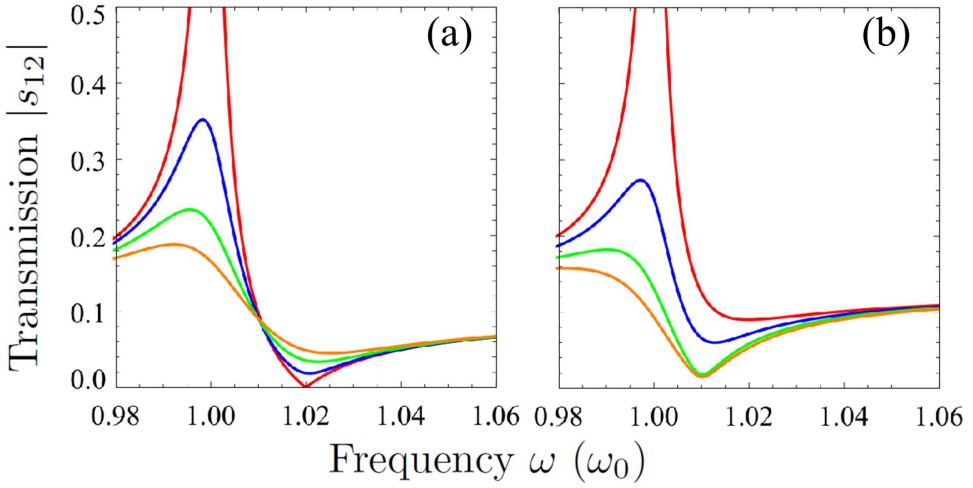
Figure 4.15: (Color online) Transmission through the resonator [Lep+]. (a) The effect of increasing internal cavity dissipation without dissipation through the background ($\epsilon = 0.05$). Only the linear cavity is taken into consideration as the qubit is in the dispersive limit. $\gamma = 2 \times 10^{-3}$ and an imaginary part $-2n\gamma i$ is added to the cavity frequency, with $n = 0, 1, 2, 3$. The internal dissipation reduces transmission and 'straightens' the interference structure. (b) The same model as figure a, only with fixed dissipative background ($\epsilon = 0.05 + 0.05i$). In this case, the transmission changes to a dip, even though there is only a weak parallel transportation.

transport. However, the two factors do not simply add up, on the contrary, under the assumption that the parallel-coupling dissipation is fixed, and the dissipation through the cavity is increased, I observe an interesting phenomenon that the minimum value of the dip decreases (Fig. 4.15 b). One deduces from Eq. 4.25 a zero point of the transmission under the condition $Im[\omega_0] = \gamma Im[\epsilon]/2|\epsilon|^2$. This zero transmission is at $\omega - \omega_0 = Re[\epsilon] Im[\omega_0]/Im[\epsilon]$. What's more, when $\epsilon \lesssim \epsilon_r$, the function of transmission is in the following form

$$|s_{21}| \approx \frac{\epsilon_r}{1 + 2\epsilon_r} \frac{\left| \frac{\epsilon}{\epsilon_r^2} + \eta \right|}{\sqrt{\left(1 + \frac{1}{2\epsilon_r}\right)^2 + \frac{\eta^2}{4}}} \tag{4.34}$$

For weak parallel transmission, ϵ and ϵ_r are much smaller than 1, compare with the Fano function, $q \gg 1$ is obtained. Under this condition, the transmission amplitude is an asymmetric dip even though the parallel transportation is rather weak. However, the reflection is always a dip (Fig. 4.16).
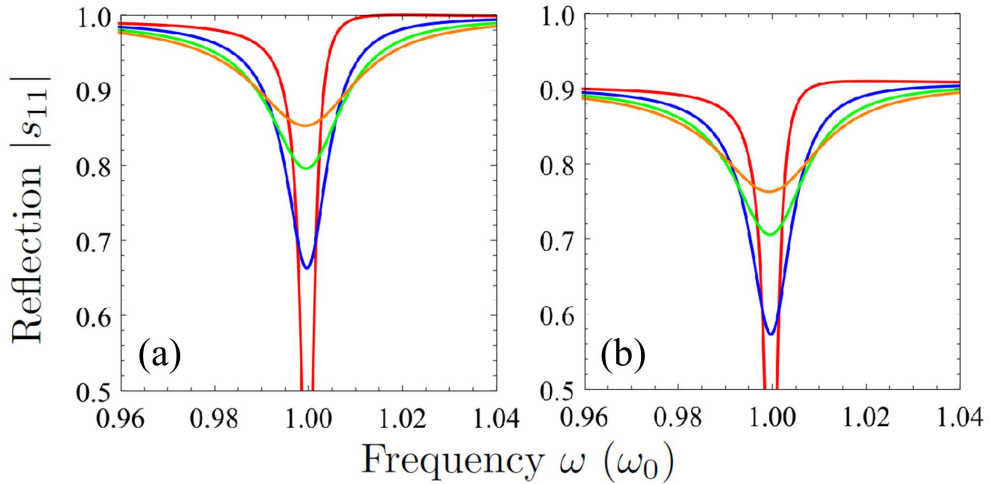
Figure 4.16: (Color online) Reflection by the resonator [Lep+]. (a) The effect of increasing cavity dissipation on the reflection amplitude without dissipation through the background of Fig. 4.15 a. The internal dissipation again 'straightens' the interference structure. (b) Similar result as figure a, while dissipation in the parallel channel is taken into account. The reflection shows a dip all the time, even though the shape of transmission under the same condition is also a dip.

Oscillator in Jaynes-Cummings model

Now I introduce the qubits to the system which origins the non-linear phenomenon, so that the complete system could not be presented as a linear resonator. The hopping between the qubit states in the dispersive limit because of on-chip heating is investigated. Afterwards, the heating effect on the resonator in the photon-blockade limit (i.e. it is only allowed to populate two-photon state of the resonator) is studied.

The effective Hamiltonian of the Jaynes-Cummings model in the dispersive limit is shown by Eq. 4.28. The steady state expectation value (i.e. $\langle \hat{a} \rangle$) is solved numerically for weak driving employing a Lindblad mater equation, under the assumption that the qubit is at finite temperature with a dissipative environment. I find several interesting limits: first of all, if the excitation rate and the decay rate are much smaller than the dynamics of the resonator (rate γ), the solution is a classical average of two results for the transmission, which correspond to the two dispersively shifted resonance frequencies of the resonator; secondly, if the excitation rate and the decay rate dominate γ and the dispersive shift, I see a dynamic averaging. But the alternating is very fast, so that only a averaged value is detected as a peak in the transmission spectrum. Plotting of the transmission under these two limits is shown in Fig. 4.17 a. What's more, if I consider a weak transportation with dissipation
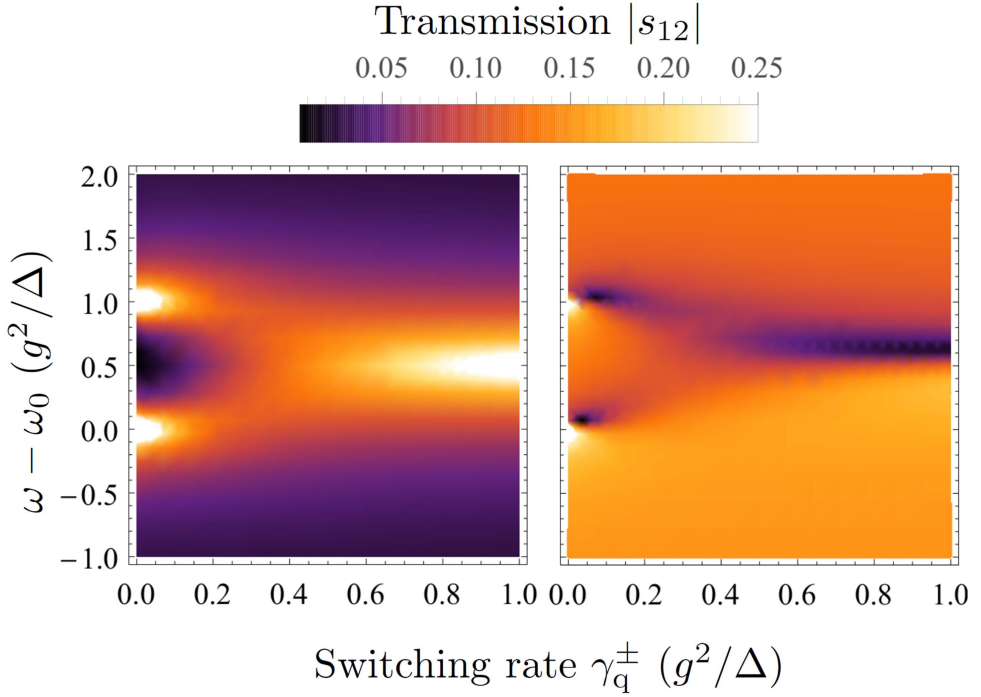
Figure 4.17: (Color online) Transmission through the Jaynes-Cummings oscillator (with $\gamma = 5 \times 10^{-4}\omega_0$) [Lep+]. The dispersive shift alternates between two values separated by g^2/Δ. The difference between the two figures is that the left one includes a weak dissipative transportation through the parallel channel, while the right one does not. The alternating between the two values is assumed to be the same for both of the qubit excitation and relaxation, and the dispersive shift is assumed to be much larger than the decay rate of the resonator (a factor of 40 is used). Thus, with a weak alternating rate and no transportation through the parallel channel, a statistical averaging of transmission for two possible cavity frequencies is observed. By increasing the alternating rate, the two peaks merge into an averaged single resonance peak. By introducing the weak dissipative transportation through the parallel channel (figure on the right), the transmission is Fano-shaped, evolving from two tilted Lorentzian-peaks to dips, and finally to a single averaged dip. At very high switching rates a tilted peak is recovered (not plotted).

through the parallel channel, a peak changing to a dip is observed in different limits (shown in Fig. 4.17 b).

The third interesting limit is when there is a strong asymmetry between excitation and decay rates and $g^2/\Delta > \gamma_q^-$ (here γ_q^- is the zero-temperature qubit decay rate). The qubit is normally at its ground state at cryogenic temperature, but incoherent short-time hopping to its excited state is achievable because of thermal excitation, but of course it decays fast. Such phenomenon is expected to result in dephasing
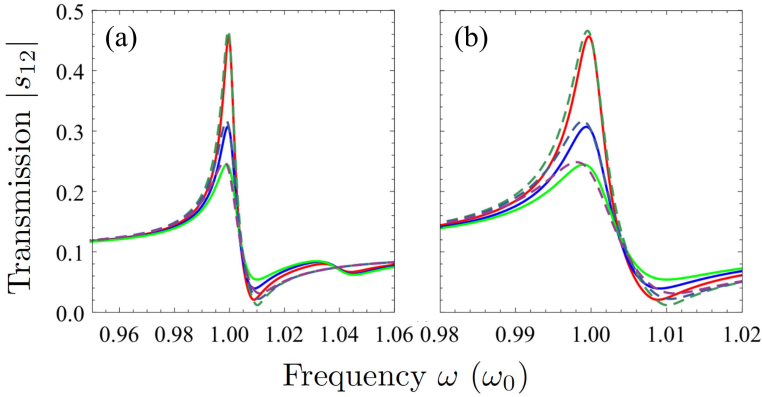
Figure 4.18: (Color online) Transmission through the Jaynes-Cummings oscillator with $\gamma_q- \gg \gamma_q^+$, $\gamma = 1 \times 10^{-3}\omega_0$, and $\epsilon = 0.05$ (i.e. dissipation-free background) [Lep+]. figure (b) zooms in at figure (a) around the resonance frequency. Here the dispersive shift $g^2/\Delta = 80\gamma$ and the decay rate $\gamma_q^- = 5\gamma$ at zero temperature. The excitation (as well as the equivalent induced relaxation) increases for different curves by rates $n\gamma$ ($n = 1, 2, 3$). The fit for linear model with growing internal dissipation (dashed lines) is done with an imaginary part for the resonance frequency $\gamma_{dephasing} = 1.2n\gamma$ ($n = 1, 2, 3$). While the excitation rate is increased, a weak disturbance shows up at the position of the upper frequency of the cavity, at $\omega = 1.04\omega_0$.

of the cavity, because of the 'diagonal' noise in its frequency. The transmission in such limit is plotted in Fig. 4.18. Such kind of dephasing shows close likeness to increasing resonator dissipation by a rate $\gamma_{dephasing} \approx \gamma_q^+$.

This can be explained by a single jump of the qubit which is enough to dephase the system in this limit. Besides, the functions of dephasing or decay are similar for superpositions of different photon number. The fit for linear model with growing internal dissipation (dashed lines) is done with an imaginary part for the resonance frequency $\gamma_{dephasing} = 1.2n\gamma$ ($n = 1, 2, 3$). While the excitation rate is increased, a weak disturbance shows up at the position of the upper frequency of the cavity, at $\omega = 1.04\omega_0$. However, the weak shift can still be distinguished experimentally.

Consider the case for multiple qubits, at least under the assumption $\gamma_{qi}^- \gg \gamma_{qi}^+$, such phenomenon is expected to sum linearly, i.e. $\gamma_{dephasing} \approx \sum_i \gamma_{qi}^+$. If the internal dissipation of the resonator is considered, including the dissipation through the parallel channel, the situation is achieved that the transmission shows only a dip on resonance (see Fig. 4.15). It differs from the internal dissipation of the resonator in dephasing, as the resonator dose not dissipate energy, only $t\langle a \rangle$ averages out. When the sources of dissipation match ($\gamma_{dephasing} = \gamma Im[\epsilon]/2[\epsilon]^2$), a temperature induced total disappearance of the amplitude of the transmission is observed. It is a
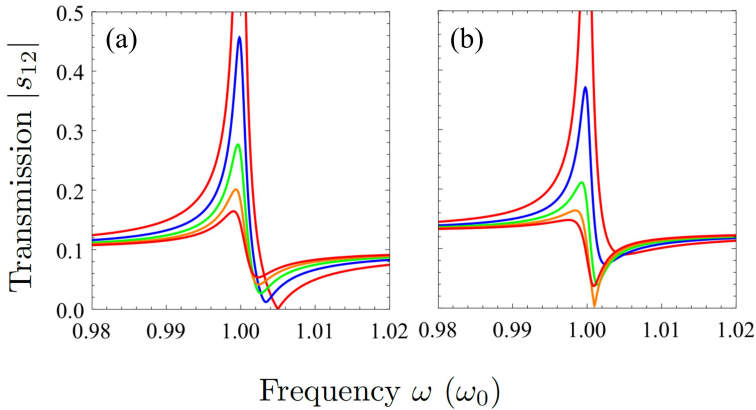
Figure 4.19: (Color online) Transmission through Jaynes-Cummings oscillator in the photon-blockaded regime for $\gamma = 5 \times 10^{-4} \omega_0$ [Lep+]. (a) The result of increasing the temperature for weak driving without dissipation through the background. The temperature induced excitation rate is $n\gamma/2$ ($n = 0, 1, 2, 3, 4$) for different curves. The Fano resonance 'straightens' too, and is narrower than the case of increasing cavity dissipation. (b) The result of increasing temperature with dissipative background in the same model. The skewed Lorentzian evolves into a dip for transmission, while temperature-induced alternating increases.

phenomenon that the dephasing of the resonator incudes signal reduction which makes the total signal to create a perfect destructive interference of transmission.

The case of thermal distribution in the resonator is also considered. For simplicity, the photon-blockaded resonator is investigated, i.e. the non-linearity is large enough to forbid one-to-two photon transition. Only two states of the resonator are included in simulation of the master equation for practical reason. The steady state expectation value $\langle \hat{a} \rangle$ is solved under the condition that the driving is weak while the transition between the two states of the resonator increases because of finite temperature. The result is shown in Fig. 4.19. The shape of the resonance 'straightens' while increase the incoherent hopping. The pure dip appears when including the dissipation through the parallel channel. The shape of the peak of the transmission is narrower compared to the dissipation of the resonator while increasing the temperature. And it could not be fitted simply with an increasing of the resonator dissipation.

4.3.3 Experimental result compared with the theory

The spectroscopic feature of the readout resonator of the 8-qubit chip in transmission is always tilted Fano-shape, with many different forms. With the theories discussed above, it could be explained by the interplay between the decoherence of the coupled

system and the propagation of the microwave field on the chip through mainly two channels: the resonator and the background (probably the DC flux bias lines).

In our analysis, the shape of the Fano resonance is always under weak driving. A general power dependence of the resonance frequency is also measured. For very high powers, the qubits are decoupled to the resonator, so that only the linear resonator contributes. For this sample, I observe all the time a Fano-shaped Lorentzian that is slightly skewed for the resonator. It could be recovered at low powers with reduced total quality factor compared to high-power case. It could be employed to fit the properties of the resonator and the parallel coupling.

For the intermediate powers, a dip corresponding to the power-dependent Stark shift is observed. This is in accordance with the theory, according to which in most cases a dip is observed when the transportation is partly blockaded (see Fig. 4.17 for example).

The Fano-shape could be removed from the experimental data using a background substraction method. Under the boundary conditions defined by Eq. 4.23, with the consideration of a week background coupling (i.e. $|\epsilon| \ll 1$) and no input from side b, the parameter ϵ is known. The field of the cavity is obtained

$$\sqrt{\gamma}\langle \hat{a}(t) \rangle = \langle \hat{b}_{out}(t) \rangle + \frac{2i\epsilon}{1 + 2i\epsilon} \langle \hat{a}_{in}(t) \rangle. \tag{4.35}$$

The equation of motion of the resonator depends now only weakly on ϵ [Lep+]. It follows that this solution is (up to a constant front factor) also the solution for an output without considering the background. The the amplitude of transmission before and after background removing is shown in Fig. 4.20. The resonator frequency shifts when a qubit goes across the resonance area while tuning the bias current.Fig. 4.20 a) shows the original data before background removing. A smooth transition between Fano-peak and dip is observed throughout the full range of the scanned coil current. While figure (b) is the result after background extraction. The Fano resonance is gone and a peak is observed all the time.

Fitting with the linear model

Our experiment is done for the ground mode of the CPW $\lambda/2$ resonator. In order to understand the subtle behavior of the scattered amplitude, the system is modeled as a continuous transmission line which is interrupted by two coupling capacitors C_{c1} and C_{c2} and accompanied by a parallel inductor L_p or equivalently a capacitor (see Fig. 4.13).
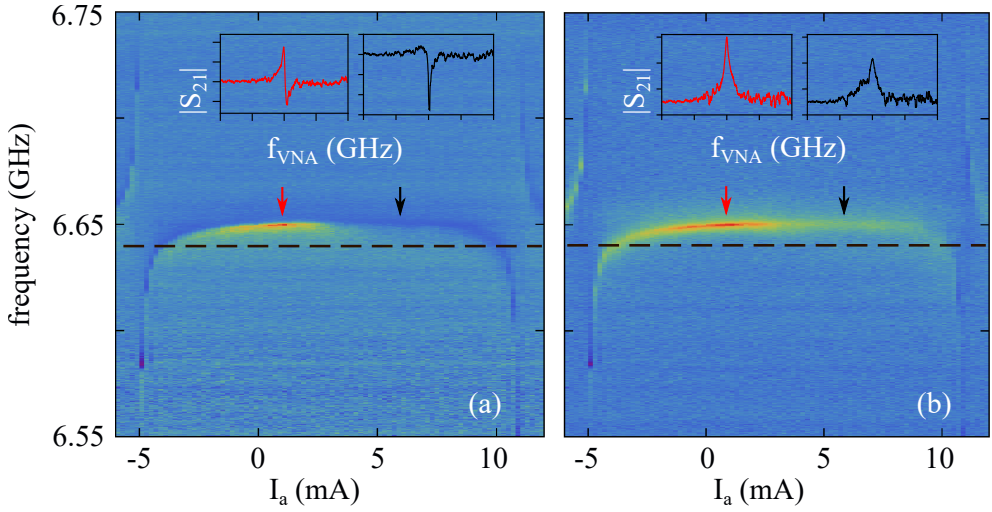
Figure 4.20: (Color online) Measured transmission amplitude as a function of the coil current. The resonator frequency shifts when a qubit goes across the resonance area. (a) The original data before background removing. A smooth transition between Fano-peak and dip is observed throughout the full range of the scanned coil current. The two insets show the shape of the resonator when the current is 1 mA and 6 mA respectively. (b) The data after background removing using the original data shown in figure a). The two insets show the shape of the resonator when the current is 1 mA and 6 mA respectively.

By employing the parallel inductor, a similar Fano shape is recovered as observed in the high-power and low-power ranges. As discussed above, the parallel inductor in the theoretical model equals to a parallel capacitor experimentally (the real system). It is also found that only a pure reactive response of the background is not enough to quantitatively explain the observation in the experiment, but the dissipation through the parallel coupling also needs to be taken into account.

The fittings to the linear model of the measured data of Fig. 4.20 are shown in Fig. 4.21 b and d. The following impedances is employed to describe the CPW resonator and the parallel environment (background) [Lep+]

$$Z_p(\omega) = i\omega L_p + R_p,$$
$$Z_{c1}(\omega) = Z_{c2} = \frac{1}{i\omega C_c},$$
$$Z^{-1}(\omega) = \frac{1}{i\omega C + \frac{1}{i\omega L} + R}.$$
(4.36)

The optimal values for the fitting are $L_p = 1.6\,nH$ (equivalents experimentally to $C_p = 33\,fF$), $R_p = 400\,\Omega$, $C_c = 4\,fF$, and for the resonator $C = 262\,fF$, $L = 2.12\,nH$.
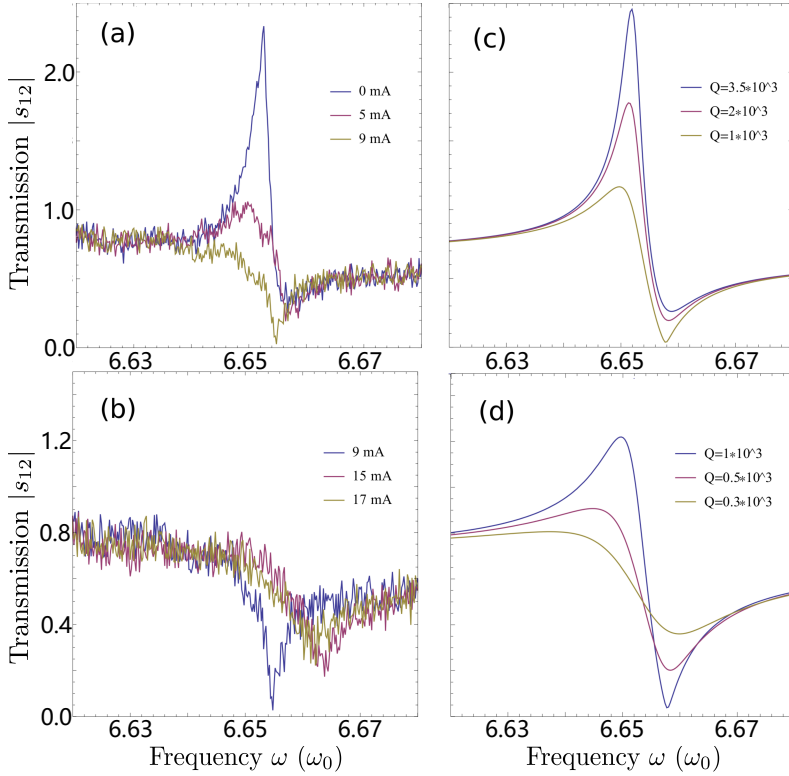
Figure 4.21: (Color online) The analysis [Lep+] of Fig. 4.20. Figures a and b shows the transition between peak and dip for different current values. (a) The maximum and minimum of the peak goes down. (b) The dip starts to rise, and vanishes for large current value. (c) and (d) are the theoretical fitting corresponding to a and b with decreasing the internal quality factor of the resonator.

In order to see the changing between the peak and dip, a change in the internal property of the resonator is introduced: it goes down while more magnetic field is applied (larger current). In fact, the influence due to other decoherence-channels (for example, the thermalization) is very analogous. The change of the Fano-shaped resonance is fitted by changing the internal resistance R of the resonator (from 350 $k\Omega$ to 30 $k\Omega$) which corresponds to the change of the internal quality factor (from 3.5×10^3 to 0.3×10^3).

Fitting with Stark shift

As shown in Fig. 4.22, along with decreasing the transportation, in most data, the thermal excitation induced Stark shift duplicates and is accompanied by 'shadows'.
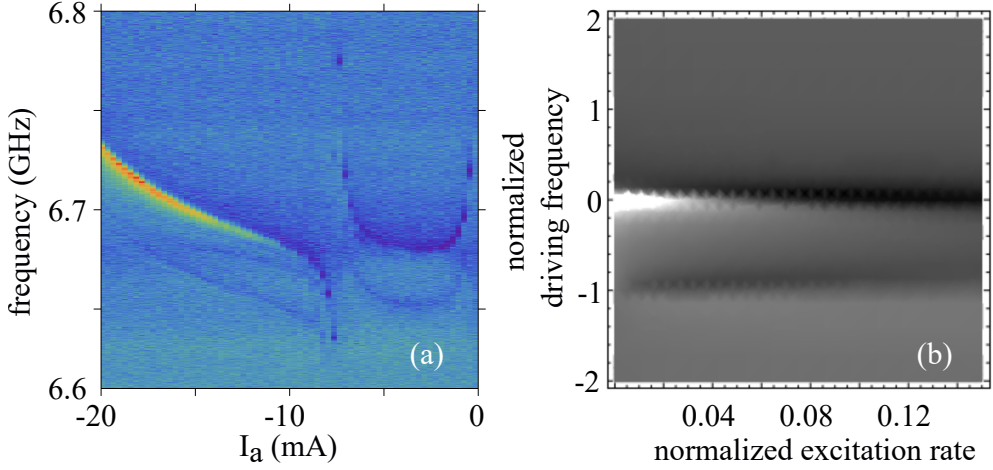
Figure 4.22: (Color online) Change of the line shape of the resonator [Lep+]. (a) The measured data for scanning over a single coil while the currents of other coils are zero. (b) The fitting for the resonance line shape using a cavity shifted dispersively and model described above. The x-axis is the temperature induced excitation rate γ_q^+, while the y-axis is the frequency of the driving, both of which are normalized by the dispersive shift. The zero-temperature decay rate of the qubit is picked to be $\gamma_q^- = 2\gamma$ and the dispersive shift $g^2/\Delta = 40\gamma$. The line shape evolves to a dip roughly when $\gamma_q^+ = 2\gamma_q^-$. The parallel coupling is modeled by an environment with dissipation for $\epsilon = 0.05 - 0.05i$.

This is an evidence of local heating due to the current running through the flux bias lines. The qubit which gets excited is not the reason for the avoided crossing, because the distance between the dominating signal and the shadow is a constant. Such an additional peak in our theoretical model is visible only under the condition that the decay rate of the excited state of the qubit is on the order of the bandwidth of the resonator. In the fitting result shown in Fig. 4.22 b, the decay rate is chosen to be twice of the bandwidth. I observe that the peak changes into a dip roughly when $\gamma_q^- = 2\gamma$ for zero temperature. For the qubit having the frequency of the order or the frequency of the resonator, it requires $T = 0.8\,K$. According to the property of dilution refrigerator, such a high temperature is unreasonable, unless the random alternating of the other 7 qubits are also taken account. Assuming all qubits contribute the same, then a rising of 200 mK of the temperature is necessary. However, for those qubits whose decay rates are much higher than the bandwidth of the resonator, the additional shadows are much less visible. What's more, correspondingly, a much lower effective temperature is required to change the peak into a dip.

Regardless of the Fano shape of the resonator, it still works perfectly as the read-out tool of all the qubits no matter it is a dip or a peak. In the next section I will discuss about the behavior of the qubits.

4.4 8 qubit measurement

Properties of the single-qubit chip are clear observed in experiments and straight-forward to understand. However, when it comes to the 8-qubit sample, several difficulties are encountered experimentally. Since the number of qubits increases, the complexity of the whole coupled system increase exponentially. First of all, the readout tool, i.e. the resonator shows an asymmetric Fano shape in most cases, which is understood well in the last section. Secondly, although the design of the chip ensures negligible direct coupling between the qubits, and tiny cross-talk between qubit and non-adjacent bias lines, it is still very necessary to perform a calculation before manipulating all the qubits. In this section, I report on the fast calibration which isolates the qubits physically, so that precise single-qubit manipulation is realized. What is also interesting is that, even though the system is measured with single-photon-level power and only a single tone which probes the resonator (the VNA), higher level transition of the qubit is still observed. This is due to thermal population caused by the heating effect of the bias current running on the chip.

Because of the uncertainty in fabrication to some extent, and let alone the enormous complexity of the 8 qubits themselves, it is not achievable to identify all the qubits directly at the very beginning by 2-tone measurement on the qubits directly. Our strategy is to perform single-tone measurement by the VNA, observing the vicinity of the frequency of the ground mode for the resonator and record the amplitude of the transmission while scanning over a large range of the current for each flux bias line. With this fast and simple approach, one is able to evaluate the property of each qubit. Afterwards, a calibration is employed experimentally to cancel out the cross-talk between qubits and the uncorresponding flux bias lines, so that each qubit is independently tunable. Only in this way, I am able to manipulate the qubits precisely and bring them one by one into the resonance with the resonator.

4.4.1 Identification of each qubit

The principle of identification for each qubit on the 8-qubit chip is basically the same as for the single-qubit chip as discussed before. The only difference is that for the 8-qubit chip, a rough, large-step scan over each coil is done before scanning them with small steps. The reason is to find a rough range of sweet spot of each qubit, and park all the qubits around their sweet spot. Only after that, the fine scans over each coil are performed. In this case, even there is cross talks, it is not visible in the result. Because the cross talk is designed to be tiny, and the qubits are at the most insensitive position to the flux change.

The multiple anti-crossing scans for all individual qubits is shown in Fig. 4.23, in which the label of the current $a \rightarrow h$ corresponds to the flux control for qubit $1 \rightarrow 8$ respectively. All qubits are tuned to the vicinity of their sweet spots, and each qubit is tuned through resonance with the resonator within a large bias current range. First of all, reasonable periodical appearance of anti-crossings for all coils proves that all qubits are alive and tunable. More over, a fitting with the energy-levels of the coupled system like what is done in Fig. 4.7 a) gives a precise evaluation of the transition frequencies of the qubits. The results of the fitting is not shown in Fig. 4.23, but listed in Table. 4.3.

No. qubit	I_{period} (mA)	$E_{J_{max}}$ (GHz)	E_C (GHz)	$f_{01_{max}}$ (GHz)
qubit 1	25	21.5	0.4	7.895
qubit 2	23.8	19.8	0.4	7.560
qubit 3	23.8	20.8	0.4	7.758
qubit 4	24.8	43	0.4	11.330
qubit 5	22.3	34.8	0.4	10.153
qubit 6	22.5	30.5	0.4	9.479
qubit 7	23.5	35.1	0.4	10.198
qubit 8	23.5	42	0.48	12.220

Table 4.3: Parameters of the 8-qubit chip .

In the case of a single qubit interacts with the resonator, the system could be studied by the J-C Hamiltonian (Eq. 2.29). The matrix for the Hamiltonian is diagonal-blocked, with eigenenergies shown in Eq. 2.30 for each block [Chi+10]. Consider only the basic transition from ground state to the first excited state of the qubit, and the single-photon condition, when the qubit is tuned closer to the resonator and is finally exactly in resonance with the resonator ($\Delta = 0$), the energy difference E_R is given by the vacuum Rabi splitting $E_+ - E_-$, namely $E_R = 2g$. Thus, the coupling strength between each qubit and the resonator is obtained by fitting the split in the single qubit tuning measurement. In order to get the coupling strength between the qubits and the resonator, a fine scan is done around one anti-crossing area for each qubit. The measured data and the corresponding fitting is plotted in Fig. 4.24 while the result of the fitting is listed in Table 4.4. Except for the ratio between E_J and E_c , the coupling strength is determined by the capacitances on-chip which depend on the geometry of the design. The good agreement between observed value and designed values means the model used to simulate the geometric capacitance on-chip is correct and the fabrication is accurate.
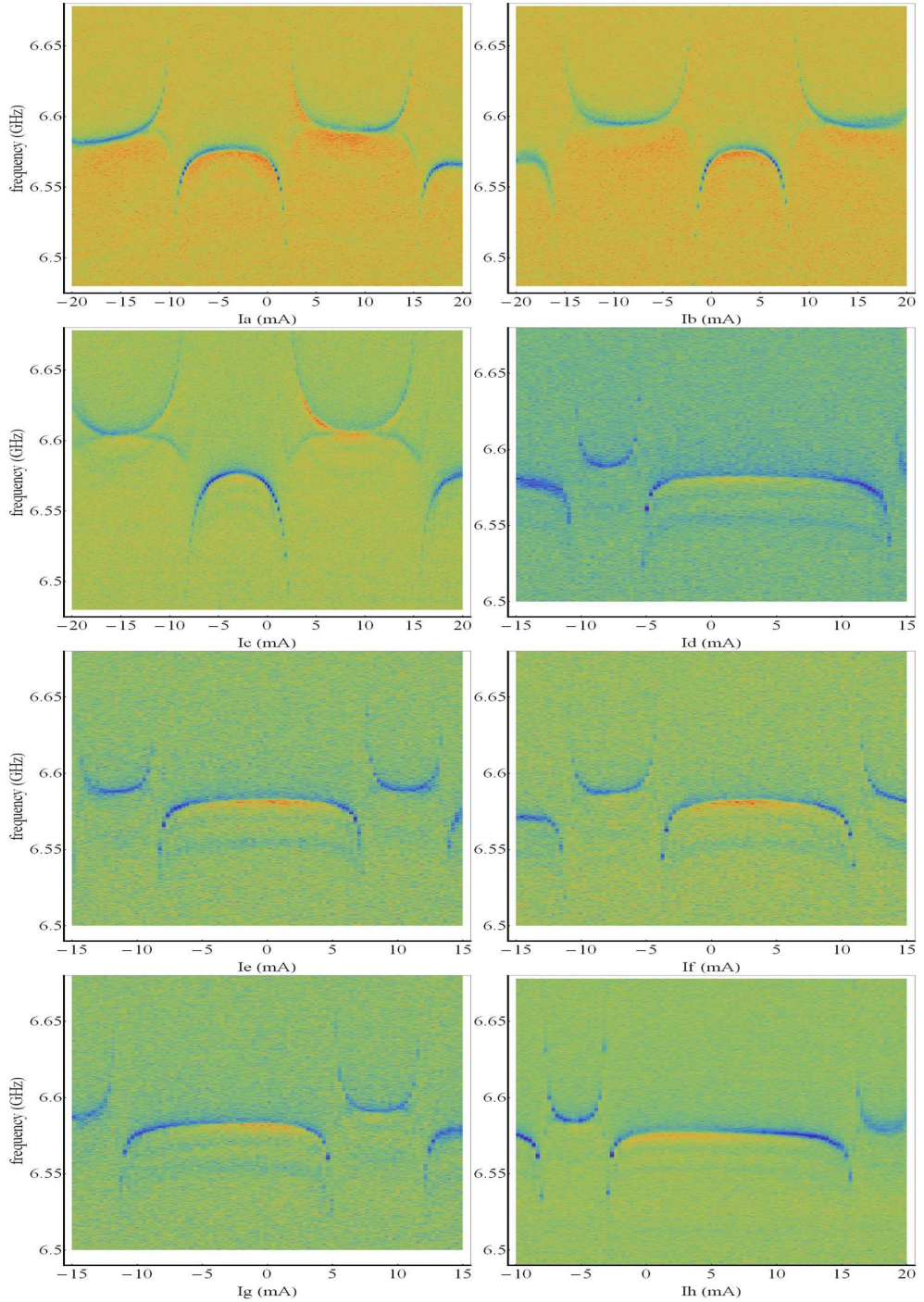
Figure 4.23: (Color online) The multiple anti-crossing scans for all individual qubits. The labelling of the current $a \rightarrow h$ corresponding to the flux control for qubit $1 \rightarrow 8$ respectively.
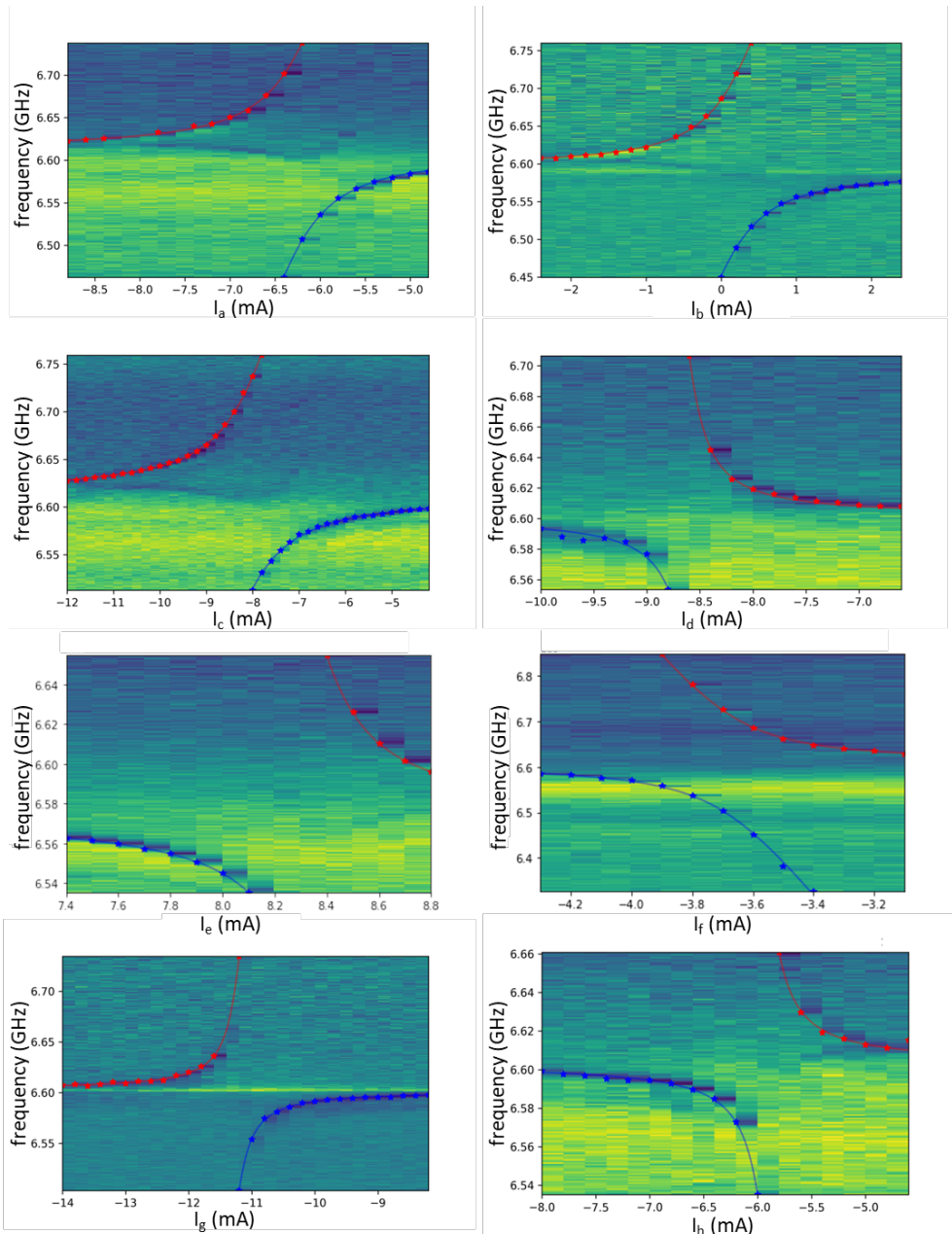
Figure 4.24: (Color online) The measured coupling strength to the resonator of each qubit. The colored stars are the extracted data points and the solid lines are the results of fitting.

	designed	qubit 1	qubit 2	qubit 3
Coupling (MHz)	113.0	114.8 ± 0.2	114.3 ± 0.4	113.4 ± 0.6
qubit 4	qubit 5	qubit 6	qubit 7	qubit 8
124 ± 4	107.5 ± 1.0	110.4 ± 1.2	114.4 ± 0.6	109.3 ± 3.7

Table 4.4: $g^{1,0}/h$ (MHz) between the resonator and each qubit. Qubit 1 to qubit 6 are used for the multi-qubit in resonance experiments. Qubit 7 and 8 are used for the higher-level transition measurement.

4.4.2 Calibration of crosstalk between coils

According to the explanation in Chap. 3.2.3, the flux bias control lines are expected to have influence on the corresponding qubit locally, which means the cross-talk between the flux control lines and non-corresponding qubits should be rather tiny. However, the cross-talk is still not negligible according to the measurement about qubit identification showed above. It is because of several practical reasons. First of all, the distance between the elements on the chip is finite, there is supposed to be small interference among them. Secondly, the sample is mounted to the dilution refrigerator, the wiring for the DC currents which goes to the chip are carried by different type of wires mounted between different stages of the fridge, let alone the effect of the current divider for the DC current which grounds all DC wires to the 4K-plate. Last but not least, the current sources employed in our experiment are the ones made by the workshop of our institute, there is cross-talk inside the equipment.

Thus, making calibration on the flux bias lines is a crucial step for later experiments [Yan+18]. It benefits us with practically perfect isolation of all qubits. The calibration is done according to the idea of automatic current-compensation strategy and is reproducible, scalable, and fast. Just single-tone measurement like the one shown in qubit-identification part is enough to build the 8×8 matrix of mutual

inductance between all of the flux bias lines and the qubits. The change of magnetic flux through each qubit is in the form of this equation:

$$
\begin{pmatrix}
\Delta\Phi_1 \\
\Delta\Phi_2 \\
\Delta\Phi_3 \\
\Delta\Phi_4 \\
\Delta\Phi_5 \\
\Delta\Phi_6 \\
\Delta\Phi_7 \\
\Delta\Phi_8
\end{pmatrix}
=
\begin{pmatrix}
M_{1a} & M_{1b} & \cdots & M_{1g} & M_{1h} \\
M_{2a} & M_{2b} & \cdots & M_{2g} & M_{2h} \\
 & & & & \\
\vdots & \vdots & \ddots & \vdots & \vdots \\
 & & & & \\
 & & & & \\
M_{7a} & M_{7b} & \cdots & M_{7g} & M_{7h} \\
M_{8a} & M_{8b} & \cdots & M_{8g} & M_{8h}
\end{pmatrix}
\begin{pmatrix}
\Delta I_a \\
\Delta I_b \\
\Delta I_c \\
\Delta I_d \\
\Delta I_e \\
\Delta I_f \\
\Delta I_g \\
\Delta I_h
\end{pmatrix} .
\tag{4.37}
$$

Here the qubits are labeled by numbers and the flux bias circuits are denoted by letters. For instance, Φ_3 is the flux through the 3_{rd} qubit, ΔI_d is the DC current running through the 4_{th} bias line, and M_{5f} is the mutual inductance between the 5_{th} qubit and the 6_{th} flux bias line. With the measurement that scans the periodical anti-crossings, a frequency point could be picked out to do the subsequent measurement for calibration. The measure point should be close to anti-crossing area, so that it is very sensitive to flux change. By recording the change in amplitude of this point while sweeping the corresponding coil together with another coil, the influence on each other of these two flux control coils is obtained (as shown in Fig. 4.25 a, b and c). In principle, the two slops should be reciprocal to each other, thus the ratio between the mutual inductances could be calculated. However, in real experiment, the 2 slops are not necessarily reciprocal. Because there is difference of the resistors employed for the current divider, and the wirings for each coil is not identical. As a result, both slops need to be fitted to get an accurate matrix. In total of 28 measurements cover all combinations of flux lines and build the full matrix of mutual inductance as follows:

$$
\begin{pmatrix}
1 & \frac{M_{1b}}{M_{1a}} & \frac{M_{1c}}{M_{1a}} & \frac{M_{1d}}{M_{1a}} & \frac{M_{1e}}{M_{1a}} & \frac{M_{1f}}{M_{1a}} & \frac{M_{1g}}{M_{1a}} & \frac{M_{1h}}{M_{1a}} \\[4pt]
\frac{M_{2a}}{M_{2b}} & 1 & \frac{M_{2c}}{M_{2b}} & \frac{M_{2d}}{M_{2b}} & \frac{M_{2e}}{M_{2b}} & \frac{M_{2f}}{M_{2b}} & \frac{M_{2g}}{M_{2b}} & \frac{M_{2h}}{M_{2b}} \\[4pt]
\frac{M_{3a}}{M_{3c}} & \frac{M_{3b}}{M_{3c}} & 1 & \frac{M_{3d}}{M_{3c}} & \frac{M_{3e}}{M_{3c}} & \frac{M_{3f}}{M_{3c}} & \frac{M_{3g}}{M_{3c}} & \frac{M_{3h}}{M_{3c}} \\[4pt]
\frac{M_{4a}}{M_{4d}} & \frac{M_{4b}}{M_{4d}} & \frac{M_{4c}}{M_{4d}} & 1 & \frac{M_{4e}}{M_{4d}} & \frac{M_{4f}}{M_{4d}} & \frac{M_{4g}}{M_{4d}} & \frac{M_{4h}}{M_{4d}} \\[4pt]
\frac{M_{5a}}{M_{5e}} & \frac{M_{5b}}{M_{5e}} & \frac{M_{5c}}{M_{5e}} & \frac{M_{5d}}{M_{5e}} & 1 & \frac{M_{5f}}{M_{5e}} & \frac{M_{5g}}{M_{5e}} & \frac{M_{5h}}{M_{5e}} \\[4pt]
\frac{M_{6a}}{M_{6f}} & \frac{M_{6b}}{M_{6f}} & \frac{M_{6c}}{M_{6f}} & \frac{M_{6d}}{M_{6f}} & \frac{M_{6e}}{M_{6f}} & 1 & \frac{M_{6g}}{M_{6f}} & \frac{M_{6h}}{M_{6f}} \\[4pt]
\frac{M_{7a}}{M_{7g}} & \frac{M_{7b}}{M_{7g}} & \frac{M_{7c}}{M_{7g}} & \frac{M_{7d}}{M_{7g}} & \frac{M_{7e}}{M_{7g}} & \frac{M_{7f}}{M_{7g}} & 1 & \frac{M_{7h}}{M_{7g}} \\[4pt]
\frac{M_{8a}}{M_{8h}} & \frac{M_{8b}}{M_{8h}} & \frac{M_{8c}}{M_{8h}} & \frac{M_{8d}}{M_{8h}} & \frac{M_{8e}}{M_{8h}} & \frac{M_{8f}}{M_{8h}} & \frac{M_{8g}}{M_{8h}} & 1
\end{pmatrix} .
\tag{4.38}
$$

Here the self-inductance is not important, only the ratio matters. The final goal is to tune only a single qubit particularly, meanwhile, keep the flux applied on the other

qubits stable. This is realized by solving a 7-variable equation set. Take tuning of qubit 1 as an instance, then the function set below should be solved, in which ΔI_b, ΔI_c, $\cdots$, ΔI_g, ΔI_h are the 7 variables, and ΔI_a is treated as known parameter:

$$
\begin{cases}
\dfrac{M_{2a}}{M_{2b}}\Delta I_a + \Delta I_b + \dfrac{M_{2c}}{M_{2b}}\Delta I_c + \dfrac{M_{2d}}{M_{2b}}\Delta I_d + \dfrac{M_{2e}}{M_{2b}}\Delta I_e + \dfrac{M_{2f}}{M_{2b}}\Delta I_f + \dfrac{M_{2g}}{M_{2b}}\Delta I_g + \dfrac{M_{2h}}{M_{2b}}\Delta I_h = 0 \\[2mm]
\dfrac{M_{3a}}{M_{3c}}\Delta I_a + \dfrac{M_{3b}}{M_{3c}}\Delta I_b + \Delta I_c + \dfrac{M_{3d}}{M_{3c}}\Delta I_d + \dfrac{M_{3e}}{M_{3c}}\Delta I_e + \dfrac{M_{3f}}{M_{3c}}\Delta I_f + \dfrac{M_{3g}}{M_{3c}}\Delta I_g + \dfrac{M_{3h}}{M_{3c}}\Delta I_h = 0 \\[2mm]
\dfrac{M_{4a}}{M_{4d}}\Delta I_a + \dfrac{M_{4b}}{M_{4d}}\Delta I_b + \dfrac{M_{4c}}{M_{4d}}\Delta I_c + \Delta I_d + \dfrac{M_{4e}}{M_{4d}}\Delta I_e + \dfrac{M_{4f}}{M_{4d}}\Delta I_f + \dfrac{M_{4g}}{M_{4d}}\Delta I_g + \dfrac{M_{4h}}{M_{4d}}\Delta I_h = 0 \\[2mm]
\dfrac{M_{5a}}{M_{5e}}\Delta I_a + \dfrac{M_{5b}}{M_{5e}}\Delta I_b + \dfrac{M_{5c}}{M_{5e}}\Delta I_c + \dfrac{M_{5d}}{M_{5e}}\Delta I_d + \Delta I_e + \dfrac{M_{5f}}{M_{5e}}\Delta I_f + \dfrac{M_{5g}}{M_{5e}}\Delta I_g + \dfrac{M_{5h}}{M_{5e}}\Delta I_h = 0 \\[2mm]
\dfrac{M_{6a}}{M_{6f}}\Delta I_a + \dfrac{M_{6b}}{M_{6f}}\Delta I_b + \dfrac{M_{6c}}{M_{6f}}\Delta I_c + \dfrac{M_{6d}}{M_{6f}}\Delta I_d + \dfrac{M_{6e}}{M_{6f}}\Delta I_e + \Delta I_f + \dfrac{M_{6g}}{M_{6f}}\Delta I_g + \dfrac{M_{6h}}{M_{6f}}\Delta I_h = 0 \\[2mm]
\dfrac{M_{7a}}{M_{7g}}\Delta I_a + \dfrac{M_{7b}}{M_{7g}}\Delta I_b + \dfrac{M_{7c}}{M_{7g}}\Delta I_c + \dfrac{M_{7d}}{M_{7g}}\Delta I_d + \dfrac{M_{7e}}{M_{7g}}\Delta I_e + \dfrac{M_{7f}}{M_{7g}}\Delta I_f + \Delta I_g + \dfrac{M_{7h}}{M_{7g}}\Delta I_h = 0 \\[2mm]
\dfrac{M_{8a}}{M_{8h}}\Delta I_a + \dfrac{M_{8b}}{M_{8h}}\Delta I_b + \dfrac{M_{8c}}{M_{8h}}\Delta I_c + \dfrac{M_{8d}}{M_{8h}}\Delta I_d + \dfrac{M_{8e}}{M_{8h}}\Delta I_e + \dfrac{M_{8f}}{M_{8h}}\Delta I_f + \dfrac{M_{8g}}{M_{8h}}\Delta I_g + \Delta I_h = 0
\end{cases}
\tag{4.39}
$$

To solve this equation set means to obtain the dependance of change on the other coils because of changing I_a, so that I know how much to compensate to the other coils while tuning qubit 1. In other words, matrix 4.38 is very crucial for calibrating out the cross-talk between all the coils. After the calibration, the variation in current is used instead of absolute value of the current. Fig. 4.25 d), e), and f) show the result after calibration for figure a), b), and c) correspondingly. The untitled lines prove that the calibration works very well.

4.4.3 6-qubit in resonance

Based on the measurement on the identification of the 8 qubits and calibration approach, I am now able to do the multi-qubit coupling experiments [Fin+09; Yan+18]. The photon number in the resonator is kept in the single-photon regime throughout this experiment, and the qubits is brought on resonance with the resonator one by one. I finally get a ensemble of 2-level system coupling to the first harmonic mode of the resonator. In the case of N qubits coupled to the resonator, the measured vacuum Rabi splitting is defined by [Chi+10]

$$
E_{R_N} = \hbar\sqrt{\Delta^2 + 4Ng^2}
\tag{4.40}
$$

where the coupling between the qubits and the resonator g is assumed to be identical. When N qubits are exactly in resonance with the resonator, the splitting is simply
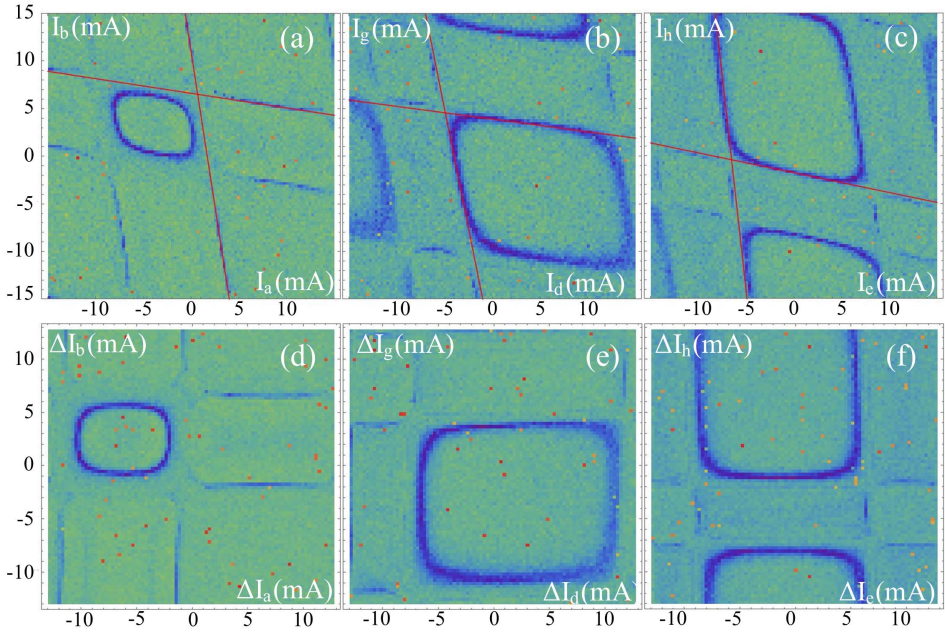
Figure 4.25: (Color online) Plot (a)-(c) show 3 examples for uncalibrated two-coil sweeps. The red solid straight lines are the fitted slops which gives the ratio between 2 mutual inductance. Plot (d)-(f) are the repeated measurement on the pair of coils of (a)-(c) after calibration. Almost no-tilt indicates good isolation between the pair of flux lines.

$\hbar 2g\sqrt{N}$. If one considers that the coupling strength is different (even though the difference is not much as shown in Table 4.4), the Rabi splitting is changed into the following form:

$$E_R = 2\hbar\sqrt{\sum g_i^2} \tag{4.41}$$

To measure this enhanced splitting, firstly, I make one qubit resonant perfectly with the ground mode of the resonator (i.e. $\Delta = 0$). Then the rest 7 qubits are tuned one by one through the resonance with the resonator. The order of qubits does not matter, I tune by the numeration just because it is easy to remember. It is supposed that all 8 qubits can be brought in resonance with the good calibration method. But in fact I am limited up to 6 qubits in experiment, because some qubits have extreme sensitivity to the fluctuation of the bias current. As shown in Table. 4.3, there are 4 qubits which have a maximum frequency around $10\ GHz$, while the frequency of the resonator is much lower ($6.674\ GHz$). Thus the curve of qubit frequency is almost upright in the resonant area, which means even a tiny change of the current changes the frequency of the qubit dramatically. For example, a change of flux $\Delta\Phi = 0.0045\Phi_0$ (corresponding to $0.1004\ mA$) causes a shift of $130\ MHz$ of qubit 5 in the resonant

area. Thus, when I tune the 6_{th} qubit into resonance, a much larger splitting than expected is observed, and the signal gets weaker due to averaging of the fluctuation.

The experimental data is shown in Fig. 4.26. The center of the splitting (marked by rosy star) drifts when adding more qubits, as shown in Fig. 4.27. The drift $\Delta\omega$ of the center of coupling more qubits compared to the center of coupling of one qubit is shown in Fig. 4.27 with red triangles. For 6 qubits, the deviation is much larger, because some qubits are not at the perfect resonance point, which result in a total accumulation in deviation. The transition between the hight level of the coupled system is surprisingly observed during these measurement, which is discussed in details in the next part.

In order to define the coupling strength, the data of up to 6 qubits coupling is fitted with theoretical curve. Consider the J-C model with one two-level qubit and a resonator, the Hamiltonian is the same as Eq. 4.47, which is shown in the next subsection. The eigenvalues of this Hamiltonian are

$$\frac{E_{\pm}}{\hbar} = \frac{\omega_r + \omega_e}{2} \pm \frac{1}{2}\sqrt{4g_{ge}^2 + (\omega_r - \omega_e)^2} \tag{4.42}$$

In the range where the splitting shows up, the relation between qubit transition frequency and the applied flux bias current could be described by a linear function $\omega_e(I) = 2\pi(aI + b)$. Substitute this linear function into Eq. 4.42, the fitting function for one qubit is obtained:

$$f_{\pm}(I) = \frac{f_r + aI + b}{2} \pm \frac{1}{2}\sqrt{4(\frac{g_{ge}}{2\pi})^2 + (f_r - aI - b)^2}. \tag{4.43}$$

For multi-qubit situation, viewing all the qubits as an ensemble, the function for the fitting is the same. However, the effective coupling strength is larger compared to the single-qubit case. In order to get the effective coupling strength for an ensemble, the multiple-qubit anti-crossing is fitted with the following formula:

$$
\begin{aligned}
f(I)_{ens_+} =& \frac{f_r + aI + b}{2} + \frac{1}{2}\sqrt{4(\frac{g_{ge}}{2\pi})^2 + (f_r - aI - b)^2}, \\
f(I)_{ens_-} =& \frac{f_r + a(I + I_{shift}) + b}{2} - f_{shift} \\
& - \frac{1}{2}\sqrt{4(\frac{g_{ge}}{2\pi})^2 + [f_r - a(I + I_{shift}) - b]^2}.
\end{aligned}
\tag{4.44}
$$

Eq. 4.44 is similar to Eq. 4.43. The only difference is that Eq. 4.44 has two more degrees of freedom (I_{shift}, f_{shift}) for the lower branch of the anti-crossing. Their function is to shift its position both in x and y direction compared to the single qubit anti-crossing. The effective coupling strength is extracted by the minimum distance

between these two branches, which means the ensemble and the resonator is on exact resonance:

$$\frac{g_{ens}(I)}{2\pi} = \frac{f(\frac{f_r - b}{a} - \frac{I_{shift}}{2})_{ens_+} - f(\frac{f_r - b}{a} - \frac{I_{shift}}{2})_{ens_-}}{2}. \tag{4.45}$$

The result of fitting is listed in Table 4.5 and shown in Fig. 4.26 with dashed white lines.

	1 qubit	2 qubit	3 qubit	4 qubit	5 qubit	6 qubit
coupling (*MHz*)	114.8 ± 0.2	162.3 ± 10.7	205.3 ± 3.6	241.6 ± 5.3	269.5 ± 4.5	348.7 ± 2.5

Table 4.5: The coupling strength between the resonator and multiple qubits. The numbers are obtained from the fitting of the measured data.

The comparison between theoretical model and the result in experiments for up to 6 qubits resonate with the resonator is shown in Fig. 4.27. The corresponding dispersive shift of the resonator is shown in Fig. 4.28, including the expected values and measured values. The measurement signal strength (see Fig. 4.29) decreases with increasing the number of qubits, indicating a collective loss mechanism of all qubits.) The signal strength $|S_{21}| \propto \kappa_c / (\gamma_{eff} + \kappa_c)$ with ensemble γ_{eff} and coupling linewidth κ_c. This is an important factor which limits the number of qubits. Consider that the qubits will decay to independent environments, the result is that half of broadening is due to the resonator γ_r and the other half is an average over the on-resonance qubits: $\gamma_{eff} = \gamma_r/2 + \sum_{i=1}^{N} \kappa_q^i / 2N$. The qubit linewidth κ_q^i depend on the bias point and their electromagnetic environment at that frequency. As a result, in the experiments, signal strength decreases for $N > 4$.

4.4.4 Higher level transition

One qubit resonant with the resonator

As explained in the part about transmon qubit, this type of qubit could be treated as multi-level system [Bre+18] rather than two-level system due to its limited anharmonicity. Since the higher level transition of the dressed system is observed in the single-tone measurement while tuning multiple qubits in resonance. I now view the transmon qubits as 3-level systems to study the transition in between the main
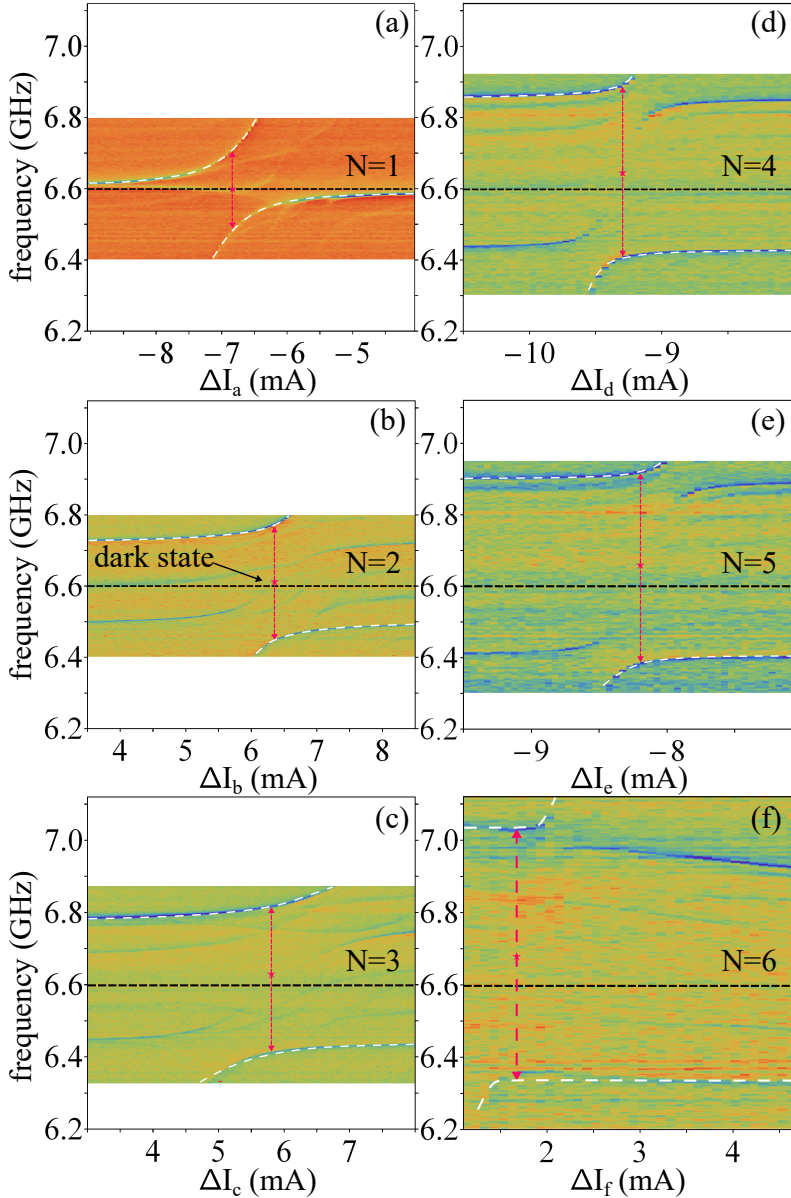
Figure 4.26: (Color online)The result of multiple qubits in resonance with the resonator experiment. Figure a)-f) present one to six qubits in resonance with the resonator respectively. The fitted data is plotted by white-dashed lines, the resonator frequency is marked by a horizontal dashed black lines.
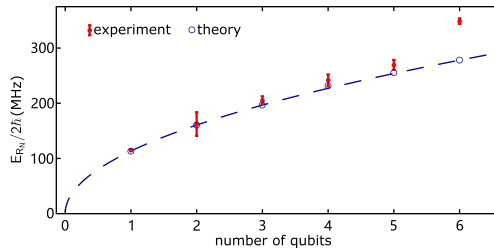
Figure 4.27: (Color online) The red points are result of the experimental data with error message. The blue open circles are the expected coupling strength calculated by the measured single-qubit coupling strength. The blue dotted line is plotted with g_{mean}, which is the mean value of the measured single-qubit g. Up to $N = 5$ experiments agree well with the theory, the $N = 6$ data is from coil-uncalibrated measurement.
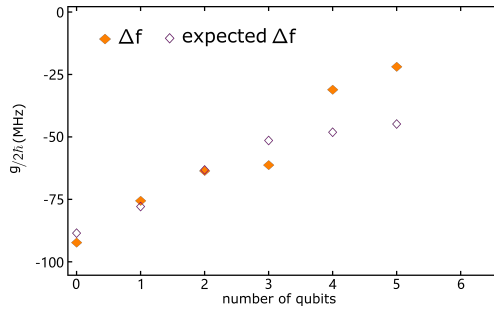
Figure 4.28: (Color online) The orange rhombus correspond to measured collective dispersive shift of the center frequencies Δf. Using the same reference, the purple open rhombus show the expected shift of the center frequencies. The bare resonator frequency is at 0 MHz.
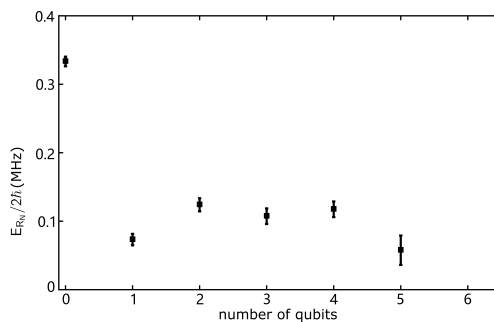
Figure 4.29: (Color online) The measurement signal strength decreases with increasing the number of qubits, indicating a collective loss mechanism of all qubits. Signal strength decreases for $N > 4$

features of the Rabi-splitting. For a single qubit interacting with the resonator, the Hamiltonian of the system could be written as

$$H_{3L1Q} = \hbar\omega_r a^\dagger a + \sum_{j=g,e,f} \omega_j |j\rangle\langle j| + \sum_{i,j=g,e,f} g_{ij}|i\rangle\langle j|(a^\dagger + a), \qquad (4.46)$$

where $|g\rangle$, $|e\rangle$ and $|f\rangle$ denote the first 3 levels of the uncoupled eigenstates of the transmon, and the corresponding eigenenergies are $\omega_g = 0$, ω_e and ω_f. Here only the next-neighbor coupling between the energy-levels of the qubit is taken into consideration and the others are assumed to be zero acquiescently (see Ref. [Koc+07]). Hamiltonian H_{3L} is block diagonal, and each of the blocks is related to a fixed conserved number of general excitation in the coupled system. In the case of zero excitation, $H_{3L} = 0$, with basis vector $|g,0\rangle$. When the total excitation is 1,

$$H_{3L} = \begin{pmatrix} \omega_r & g_{ge} \\ g_{ge} & \omega_e \end{pmatrix}, \qquad (4.47)$$

with basis vectors $\{|e,0\rangle, |g,1\rangle\}$. Consider the total excitation of 2,

$$H_{3L} = \begin{pmatrix} 2\omega_r & \sqrt{2}g_{ge} & 0 \\ \sqrt{2}g_{ge} & \omega_r + \omega_e & g_{ef} \\ 0 & g_{ef} & \omega_f \end{pmatrix}, \qquad (4.48)$$

with basis victors $\{|f,0\rangle, |e,1\rangle, |g,2\rangle\}$.

By diagonalizing the Hamiltonians shown in Eq. 4.47 and Eq. 4.48, the eigenenergies of the first two excitation manifolds of the system are deduced (indicated in Fig. 4.30 b).

Making measurement on a single qubit tuning through the resonance with the resonator with more data points, while keeping the other qubits far away, Fig. 4.30 a is obtained. The dashed lines with different color correspond to different level-transitions illustrated in figure c. The numerical simulation done by QuTiP [JNN12] is shown in Fig. 4.30 b, which shows excellent agreement with the measured data. The transitions are identified in our experiment. Surprisingly, the transitions are not the expected two-photon transitions (as discussed in section about the single-qubit chip), but rather single photon transitions which starts from the first excited manifold. This means the first excited manifold is populated, most likely thermally by the heating effect caused by the on-chip flux bias current elements. This is reasonable because it affects the temperature-dependent Fano-shaped resonator as well. Meanwhile, the 2-photon transition can not be seen in this measurement, because it requires relatively high driving power on the qubit.
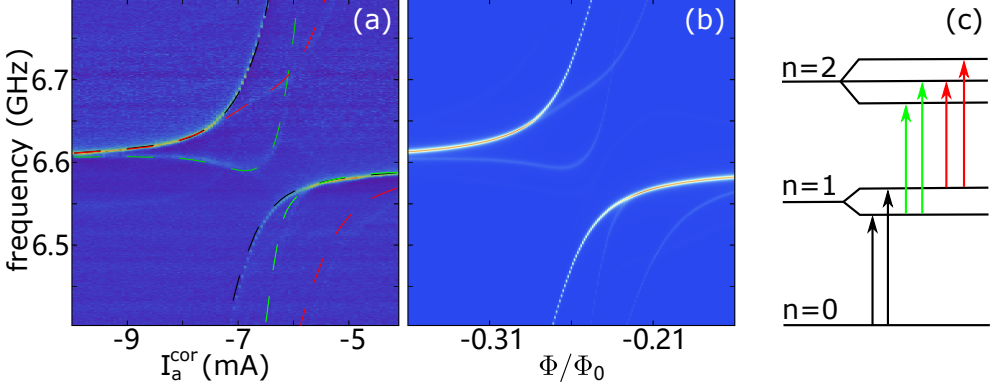
Figure 4.30: (Color online) Comparison between experiments and simulating results of one qubit tuned through the resonator frequency. (a) Experimental data of the anti-crossing where the colored lines correspond to the identified higher level (single photon) transitions shown picture c. (b) Master equation simulation by QuTiP [JNN12] for a three-level qubit interacting with a resonator which has an average thermal photon population of 0.1 photons. (c) Energy-diagram of the first two manifolds of the dressed system.

Two qubit resonant with the resonator

The model for a single qubit can be extended to the case for multiple qubits interacting resonantly with the resonator (Tavis-Cummings model with the qubits treated as 3-level systems). The Hamiltonian for two qubits could be written in the following form:

$$
\begin{aligned}
H_{3L2Q} =& \hbar\omega_r a^\dagger a + \sum_{j=g,e,f} \omega_j^{Q1}|j\rangle\langle j| + \sum_{j=g,e,f} \omega_j^{Q2}|j\rangle\langle j| \\
&+ \sum_{i,j=g,e,f} g_{ij}^{Q1}|i\rangle\langle j|(a^\dagger + a) + \sum_{i,j=g,e,f} g_{ij}^{Q2}|i\rangle\langle j|(a^\dagger + a),
\end{aligned}
\tag{4.49}
$$

with the basis $\{|g\rangle, |e\rangle, |f\rangle\}^{Q1} \otimes \{|g\rangle, |e\rangle, |f\rangle\}^{Q2} \otimes \{|0\rangle, |1\rangle, \ldots, |n\rangle\}$. Similarly, this Hamiltonian is also block-diagonal and each block associates with a fixed conserved number N of the total excitations in the coupled system. In the case of zero excitation, $H_{3L2Q} = 0$, with basis vector $|g, g, 0\rangle$. When the total excitation is 1,

$$
H_{3L2Q} = \begin{pmatrix} 2\omega_r & \sqrt{2}g_{ge} & 0 \\ \sqrt{2}g_{ge} & \omega_r + \omega_e & g_{ef} \\ 0 & g_{ef} & \omega_f \end{pmatrix},
\tag{4.50}
$$

with basisvectors $\{|g,g,1\rangle, |g,e,0\rangle, |e,g,0\rangle\}$. When the total excitation is 2,

$$
H_{3L2Q} = \begin{pmatrix} 2\omega_r & \sqrt{2}g_{ge} & \sqrt{2}g_{ge} & 0 & 0 & 0 \\ \sqrt{2}g_{ge} & \omega_r + \omega_e^{Q2} & 0 & g_{ge} & 0 & g_{ef} \\ \sqrt{2}g_{ge} & 0 & \omega_r + \omega_e^{Q1} & g_{ge} & g_{ef} & 0 \\ 0 & g_{ge} & g_{ge} & \omega_e^{Q1} + \omega_e^{Q2} & 0 & 0 \\ 0 & 0 & g_{ef} & 0 & \omega_f^{Q1} & 0 \\ 0 & g_{ef} & 0 & 0 & 0 & \omega_f^{Q2} \end{pmatrix}, \tag{4.51}
$$

with basisvectors $\{|g,g,2\rangle, |g,e,1\rangle, |e,g,1\rangle \, |e,e,0\rangle \, |f,g,0\rangle \, |g,f,0\rangle\}$.

Diagonalization of the Hamiltonians in Eq. 4.50 and Eq. 4.51 yields the eigenenergies of the first two excitation manifolds of the system. The level-scheme is shown in Fig. 4.31 d). The experimental result of 2 qubit resonant with the resonator is shown in Fig. 4.31 a). Fig. 4.31 b) shows the numerical simulation of the master equation by QuTiP [JNN12] for two three-level qubits interacting with a resonator which has an average thermal photon population of 0.1 photons.
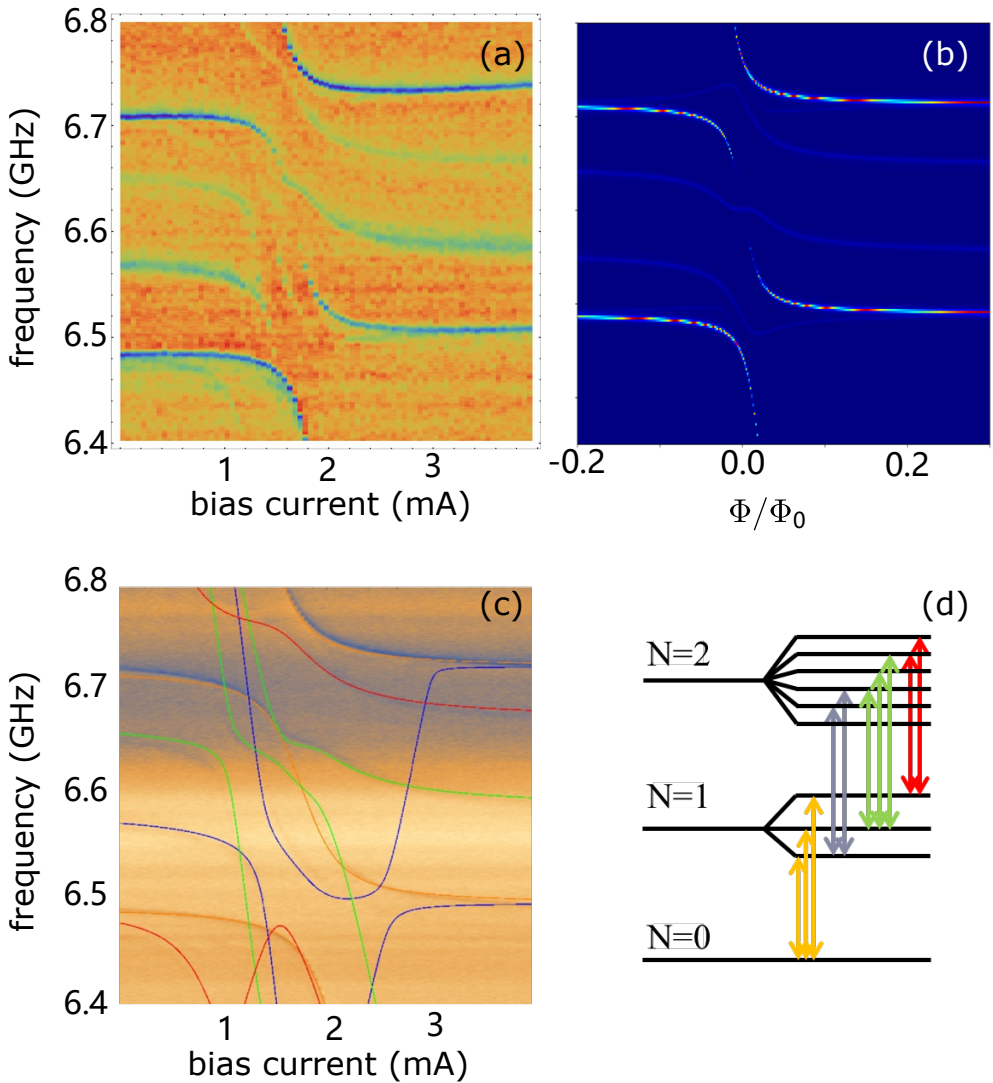
Figure 4.31: (Color online) Experimental data and fitting to the theoretical model of the second qubit tuned through the resonator frequency. (a) Experimental data. (b) Master equation simulation by QuTiP [JNN12] for two three-level qubits interacting with a resonator which has an average thermal photon population of 0.1 photons. (c) Theoretical curves plotted together with the measured data. The different color of the solid lines correspond to the color in figure d). (d) Energy-diagram of the first two manifolds of the dressed system.

5 Collective mode of an array of transmon qubits

Except for the study on the individual-controllable qubits, I am also interested in the collective behavior of multiple qubits. Precess control of each individual qubits limits the number of qubits I could study (in my case 6 qubits), on the contrary, globally controlled qubits allow me to study larger number of qubits. A large number of artificial atoms can constitute quantum metamaterials because of controllable quantum states and their coherent behavior.

In order to investigate the collective mode of multiple qubits, I collaborate with Dr. Kirill. V. Shulga in such a way that I design and fabricate the sample with an array of transmon qubits coupled to a mutual resonator with global control for the qubit-array, and he measures the sample in Moscow.

In this chapter we discuss about the preparation and investigation of the system consists of a $\lambda/2$ resonator and 20 transmon qubits that are capacitively coupled to one end of the resonator. A similar work about such quantum metamaterials was done by flux qubits that are magnetically coupled to the resonator [Mac+14]. In our work we find that because of the relatively small anharmonicity of the transmon, the transitions to higher qubit-levels of the collective multi-photon are excited. What's more, the transmon qubits show a more pronounced coherent property because they are practically more identical due to smaller uncertainty during fabrication.

5.1 The sample

The sample is designed in Karlsruhe Institute of Technology, and fabricated in the clean room of CFN (Center for Functional Nanostructures). The picture of the sample is shown in Fig. 5.1. The transmission line (marked as feedline C) is used to transmit the microwave signal. Two $\lambda/2$ CPW resonators having different fundamental frequencies are capacitively coupled by one end to the feedline to readout and manipulate the qubits. An array of 20 transmon qubits designed to be identical are
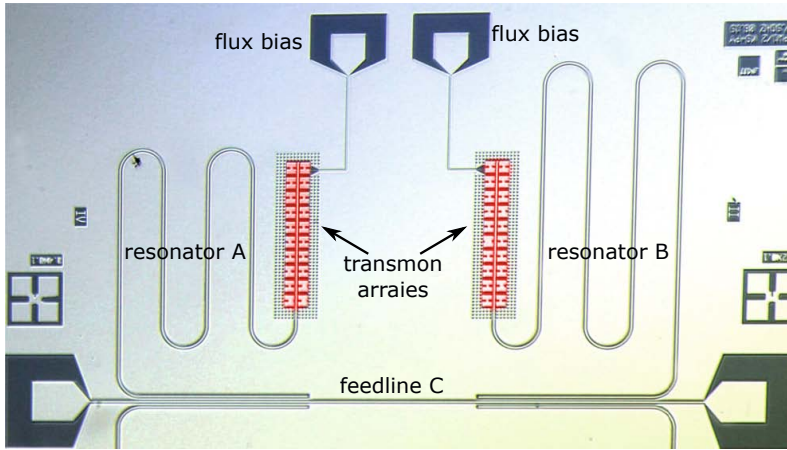
Figure 5.1: (Color online) Optical photograph of the sample [Shu+17]. At the bottom is the feedline C used to transport the microwave signal. $\lambda/2$ resonator A and B are capacitively coupled to the feedline by one end. At the other end of each resonator, there is an array of 20 transmon qubits capacitively coupled, who has a global flux bias control.

placed around the center conductor of each resonator on the other end and biased by a mutual flux control element.

The fabrication of the sample is a two-step procedure employing both optical lithography and electron-beam lithography which are discussed in Sec. 3.3. The micron-sized elements (such as the resonator, the flux bias control elements and the grounding panel) are fabricated firstly by optical lithography. The second step is to produce the Josephson junctions by the standard shadow evaporation technique. The material employed for this sample is also aluminum. Each of the qubit has a SQUID with 2 junctions which makes it tunable. The designed Josephson energy $E_{J_{max}}/2\pi\hbar = 19.86$ GHz and charging energy $E_C/2\pi\hbar = 290$ MHz. The designed maximum transition frequencies between ground state and the first excited state is $f_{01} = 6.503$ GHz. As discussed before, the anharmonicity is roughly $E_C/2\pi\hbar$.

The quality factor of the resonator is measured by sending a weak probing microwave signal through the feedline and measure the dip formed by the resonator in the amplitude of $|S_{21}|$. The intrinsic quality factor is measured to be $Q \simeq 5000$.

5.2 Experimental result

The experiments are also done by a dilution refrigerator which cools down the sample to about 20 mK [Shu+17]. A VNA (vector network analyzer) is employed to probe

the amplitude of the transmitted microwave signalled through the feedline. The two CPW resonators used for this sample are expected to form a Lorentzian-shaped dip in the transmitted signal because of the absorbtion of the microwave which hits their resonant frequencies. In order to apply a uniform static magnetic field to all the qubits, the on-chip flux bias control element is not used, but a superconducting coil is chosen instead. The coil is twined around the sample holder, to apply a magnetic field perpendicular to the surface of the sample. The sample holder has a special shape [Ave+14] in order to avoid the influence on the qubit signal caused by the parasitic electromagnetic modes of the coil.

While sweeping the current of the coil, the frequencies of all the qubits are tuned. One observes in the spectrum a large number of anti-crossings between a resonator and the 20 qubits coupled to it. The qubits are designed to be identical, but in practice, they are not perfectly the same. The parameters of the real qubits always deviate from the desired value due to technical reason: the Josephson junctions have tiny areas (100 $nm \times$ 100 nm), and could not be completely identically fabricated. However, exactly these features give rise to the possibility to observe multitude of anti-crossings in the spectrum. In other words, even though the qubits do not have the same transition frequency, the synchronized collective modes are still expected due to the interaction between the qubits through the electromagnetic filed of the mutual resonator. Ref. [VF14] provides the theoretical model of such processes under certain conditions.

Fig. 5.2 shows the experiment on the amplitude of the transmitted signal with respect to the frequency and the change of the magnetic field which is represented by the current sending through the coil. In Fig. 5.2 (a), the experiment is done in the power of single-photon level as the total microwave power on-chip is less than -130 dBm. A number of quasi-crossings between the resonator and the qubits show up due to not only the qubit-resonator interaction but also the qubit-qubit interactions. Most interestingly, when the current is about ± 16 mA, large splitting appears. In these two regions, the energies of the dressed states $|+, n\rangle$ and $|-, n + 1\rangle$ degenerate. It indicates the energy exchange between the resonator and a collective mode of multiple qubits. Except for the individual behavior of the qubits, a common resonance frequency of the entire qubit array also has the same periodic dependence on the magnetic field as N individual qubits. The splitting scales up with $\sqrt{N}$ compared with the splitting of a single qubit. This result agrees with the observation with flux qubit in Ref. [Mac+14] and in our experimental results with the 8-qubit chip. The dephasing rate Γ_ϕ is expected to be much larger than the coupling strength between a single qubit and the resonator (i.e. $\Gamma_\phi \gg g$). This means the anti-crossings of each qubit from the cluster could hardly be resolved against the background noise and the line of the collective mode.

When there is no magnetic field (i.e. the current is 0 mA), there is also an interesting feature of the spectral lines: the resonator frequency becomes higher and two additional resonances appear. It is because the transition frequencies of two qubits happen to be lower and very close to the resonator frequency. And they push the resonator up to higher frequency and get excited directly by the driving microwave field.

Fig. 5.2 (b) shows a similar measurement as figure(a), but with higher driving power (-100 dBm on-chip) which enables one to distinguish the two different types of anti-crossings (individual and collective). The small splitting corresponds to individual qubit-resonator interaction, and the large ones are generated by the interaction between a qubit cluster and the resonator. By measuring the small splitting, the coupling strength of a single qubit to the resonator is obtained to be about 5 MHz. And the collective coupling strength for the large splitting at ± 13 mA is 10-13 MHz. Considering the coupling strength scales up with the square root of the qubit number, One can estimate the number of qubits in this cluster is $N \approx 5 - 7$. It is reasonable that this number is smaller than 20, on account of defect qubits and non-identical qubit parameters.

However, a larger splitting of the collective mode indicates shorter coherence time compared to a single qubit in the array. It is caused by a stronger dephasing because of both the enhanced effective collective coupling strength and the uncertainty of the photon numbers for the coherent state of the resonator at higher radiation power.

Fig. 5.3 show the experimental results on the collective behavior of the qubits as well as the individual qubits of this metamaterial structure with two-tone measurement. The $|S_{21}|$ amplitude is from the weak probing tone, while the y axis is the frequency of the strong driving tone (-100 dBm). There are numbers of spectroscopic curves which show the transition frequencies of not only the single qubit but also the cluster of qubit (more intense lines). According to these results, the deviation of the maximum frequencies of the qubits is larger than 2 GHz. Multi-photon transitions from the ground state to higher levels of the qubit array are also observed in this experiment. The principle is explained previously in Fig. 4.9. The observed transitions are marked by the blue arrows in Fig. 5.3, where m is the photon number corresponding to the transition $\frac{1}{m}(|0\rangle \rightarrow |m\rangle)$. It is worth noticing that a 6.0 GHz signal which is far from the resonator frequency excites weakly the collective mode, which is an evidence for qubit-qubit coupling through the resonator.

The two green rectangles in Fig. 5.3 indicate the anti-crossing formed by individual qubits and the qubit cluster. The transition frequencies of the qubits have different dependence on the global flux control. Thus a particular single qubit (label as "X") could be picked out from the transmon array and interact with the common cluster
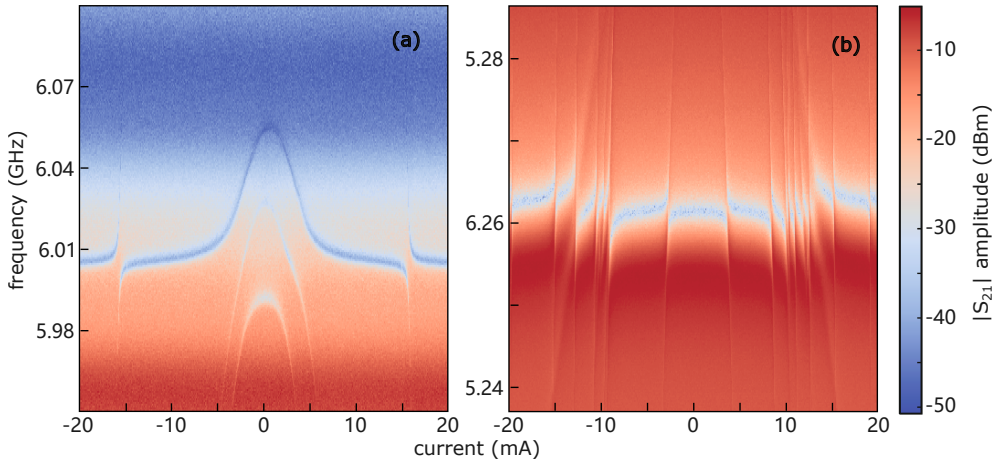
Figure 5.2: (Color online) The experiment on the amplitude of the transmitted signal with respect to the frequency and the change of the magnetic field which is represented by the current sending through the coil. (a) Measurement on resonator A with low power (-130 dBm). A number of quasi-crossings between the resonator and the qubits show up due to not only the qubit-resonator interaction but also the qubit-qubit interactions. When the current is about ±16 mA, large splitting appear. In these two regions, the energy exchange between the resonator and a collective mode of multiple qubits appears. (b) Measurement on resonator B with high power (-100 dBm). The splitting corresponding to the qubit cluster which are indicated by the yellow arrows can be separated from the splitting for a single qubit.

mode. The depth of the signal decreases while the detuning increases in the region of the anti-crossing. It is another evidence for qubit-qubit coupling through the resonator.

in summary, we study the coherence behavior of an transmon array coupled to a mutual CPW resonator. Collective modes of multiple qubits are investigated and are stable for multi-photon transition. The observed interaction between the qubit cluster and a single qubit opens up the gate to making quantum memory with large arrays of superconducting qubits.
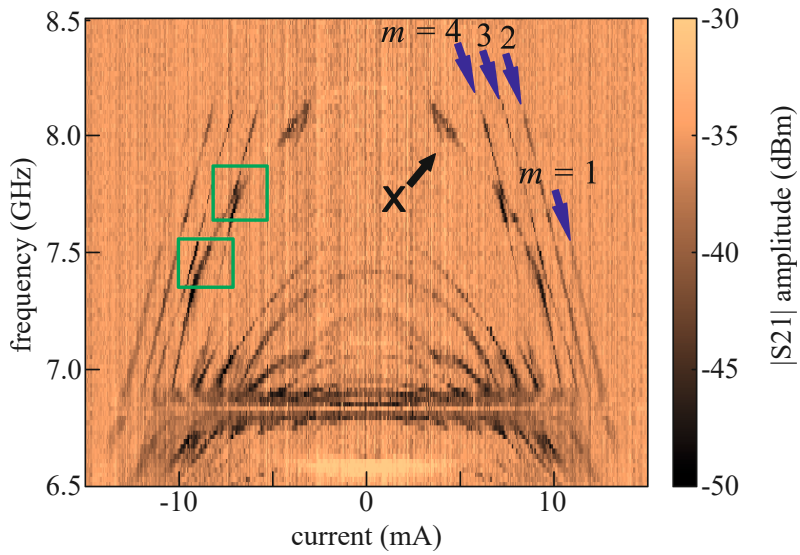
Figure 5.3: (Color online) Two-tone measurement on the qubits coupled to resonator A at high driving power (-100 dBm) of the qubits. The horizontal line at about 6.8 GHz is due to another test resonator on the sample. The blue arrows mark the multi-photon transitions from the ground state to higher levels of the qubit array, with m which is the photon number for the transition $\frac{1}{m}(|0\rangle \rightarrow |m\rangle)$. The two green rectangles indicate the anti-crossing formed by individual qubits and the qubit cluster.

6 Conclusion and outlook

In this thesis multiple transmon qubits and their mutually coupled read-out resonator are studied. The aim of this work is to build an array of fully controllable superconducting qubits which are readout by a mutual CPW resonator.

The relevant principles in Circuit QED are introduced in Chapter 2, including how the CPW resonator and the Transmon qubit work, the theoretical model to described the coupled system, as well as how the resonators functions as the readout tool.

The design and fabrication are explained in Chapter 3. The samples are devised and manufactured in Physics Institute of KIT (Karlsruhe Institute of Technology) by ourselves. The design of the sampled is done by a combination of the softwares L-Edit and Sonnet for layout generator and simulation. The pattern of the sample with multiple layers for different elements is generated by L-Edit. The simulation on the CPW resonator is done by Sonnet based on the real pattern employing lossless metal. However, the qubits are simplified and replaced by harmonic oscillators with ideal elements presenting their characteristic parameters, in order to investigate the influence on the resonator.

The sample is fabricated by a standard one-step double-angle evaporation technique. The accomplishment for the home-made samples is that the real parameters obtained from measurements match very well with the targeted values, in particular the coupling strength between the resonator and the qubits, which depends on the ratio of E_J and E_C and the geometric capacitances among the resonator, the qubits and the ground. All of the Josephson junctions are alive since all the qubits are tunable. What's more, based on the experiments of tuning the qubits, the maximum frequencies of the qubits stay in a reasonable range around the targeted value, this means the junctions are not far different from the design.

With the single-qubit chip, I exam the properties of the resonator and qubit, and it shows expected behavior and promising quality of the 8-qubit chip. How ever, for the 8 qubit-chip, unexpected dip-peak-dip change of the form of the resonator occurs. It is well explained by Fano resonance. Theoretical model is built considering the dissipation through a parallel channel of background and heating effect caused by the flux bias lines which carries DC currents. Despite for the asymmetric line-shape

of the resonator, the scattering phenomenon has no influence on the level-transition in our Tavis-Cummings system, and the resonator works well as a readout tool.

The qubits are well isolated from the non-corresponding flux bias lines thanks to the calibration of the bias lines. The idea of the calibration is to compensate the current through the other bias lines while tuning a single qubit with its corresponding flux bias, so that the flux applied on the rest of the qubits stay unchanged. The method I used is simple, fast and reproducible. Because for the calibration, I do not measure the qubits at all, but rather perform measurement only on the shift of the resonance frequency of resonator by a single-tone measurement while tuning 2 coils. By fitting the slops, the matrix of the mutual inductance is obtained, with which I build the compensation routine.

I am able to manipulate the transition frequencies of the qubits very precisely. Parking all 8 qubits at their maximum frequencies is simple because the qubits are at their sweet spots. However, tuning the qubits into resonance with the resonator is very difficult as they are much more sensitive to the flux change. I finally end up with tuning 6 qubits into resonance with the resonator, and the data demonstrates the coupling strength between the resonator and the ensemble scales up with the square root of the number of qubits.

Transitions between the first manifold and the second manifold of the coupled system is observed during tuning the qubits on resonance of the resonator. The theoretical model is studied for single-qubit case and two-qubit case. The numerical simulation done by QuTiP agrees well with the measured data. This phenomenon proves again that there is probably heating effect caused by the flux bias currents, which thermally populates the first excited manifold.

In conclusion, I have successfully fabricated the sample with aimed parameters for 8 superconducting transmon qubits coupled to a mutual resonator bus. The change of the line-shape of the resonator is well understood. All the qubits are in practice individually tunable, due to the isolation from the cross-talk to non-corresponding flux bias lines to the first order. The calibration method is simple, fast, reproducible and scalable. I have proved the coupling strength between the mutual readout resonator and the qubits cluster scales up with the square root of the number of qubits. Higher level transitions are studied for system including up to 2 qubits.

Our circuit is a perfect quantum simulator for Tavis-Cummings model. One could fully control the number of qubits interacting with the mutual resonator bus, and manipulates the transition frequencies of the qubits precisely.

Our approach could be in principle scaled up to an array of any number of qubits, so that makes it possible to explore the physics beyond the strong coupling regime

(where the rotating wave approximation is no longer valid). The scaled-up multiple qubits could be treated as a macrospin which allows one to simulate the ultra-strong coupling limit.

The present sample could also be employed to investigate the system of which the coupling strength is comparable to the anharmonicity of the qubits, entanglement generation of artificial atoms which have identical transition frequencies through coupling to the mutual cavity bus, superradiance phenomenon of multiple excited superconducting qubits, and many other interesting topics in quantum physics and quantum simulation.

Bibliography

[Abr61]   A. Abragam: *The principles of nuclear magnetism*. Oxford university press, 1961 (cit. on p. 65).

[Ave+14]   A. Averkin, A. Karpov, K. Shulga, E. Glushkov, N. Abramov, U. Huebner, E. Il'ichev, and A. Ustinov: *Broadband sample holder for microwave spectroscopy of superconducting qubits*. Review of Scientific Instruments **85**.10 (2014), p. 104702 (cit. on p. 105).

[BCS57]   J. Bardeen, L. N. Cooper, and J. R. Schrieffer: *Microscopic theory of superconductivity*. Physical Review **106**.1 (1957), p. 162 (cit. on p. 10).

[Bar+13]   R. Barends, J. Kelly, A. Megrant, D. Sank, E. Jeffrey, Y. Chen, Y. Yin, B. Chiaro, J. Mutus, C. Neill, et al.: *Coherent Josephson qubit suitable for scalable quantum integrated circuits*. Physical review letters **111**.8 (2013), p. 080502 (cit. on p. 12).

[Ben80]   P. Benioff: *The computer as a physical system: A microscopic quantum mechanical Hamiltonian model of computers as represented by Turing machines*. Journal of statistical physics **22**.5 (1980), pp. 563–591 (cit. on p. 1).

[Bis+09]   L. S. Bishop, J. Chow, J. Koch, A. Houck, M. Devoret, E. Thuneberg, S. Girvin, and R. Schoelkopf: *Nonlinear response of the vacuum Rabi resonance*. Nature Physics **5**.2 (2009), p. 105 (cit. on p. 73).

[Bla+04]   A. Blais, R.-S. Huang, A. Wallraff, S. M. Girvin, and R. J. Schoelkopf: *Cavity quantum electrodynamics for superconducting electrical circuits: An architecture for quantum computation*. Physical Review A **69**.6 (2004), p. 062320 (cit. on p. 2).

[Blo05]   I. Bloch: *Ultracold quantum gases in optical lattices*. Nature Physics **1**.1 (2005), p. 23 (cit. on p. 1).

[Bos24]   S. N. Bose: *Planck's law and the hypothesis of light quanta*. Z. Phys **26**.178 (1924), pp. 1–5 (cit. on p. 10).

[Bou+98]   V. Bouchiat, D. Vion, P. Joyez, D. Esteve, and M. Devoret: *Quantum coherence with a single Cooper pair*. Physica Scripta **1998**.T76 (1998), p. 165 (cit. on p. 11).

[Bra+15] J. Braumüller, J. Cramer, S. Schlör, H. Rotzinger, L. Radtke, A. Lukashenko, P. Yang, S. T. Skacel, S. Probst, M. Marthaler, et al.: *Multiphoton dressing of an anharmonic superconducting many-level quantum circuit*. Physical Review B **91**.5 (2015), p. 054523 (cit. on p. 60).

[Bra+17] J. Braumüller, M. Marthaler, A. Schneider, A. Stehli, H. Rotzinger, M. Weides, and A. V. Ustinov: *Analog quantum simulation of the Rabi model in the ultra-strong coupling regime*. Nature Communications **8**.1 (2017). DOI: 10.1038/s41467-017-00894-w (cit. on p. 2).

[Bre+18] J. Brehm, P. Yang, J. Leppäkangas, L. Guo, A. Ustinov, and M. Weides: *Higher level transition in Tavis-Cummings system with multiple qubits in resonance with the resonator*. In preparation (2018) (cit. on p. 95).

[Chi+10] I. Chiorescu, N. Groll, S. Bertaina, T. Mori, and S. Miyashita: *Magnetic strong coupling in a spin-photon system and transition to classical regime*. Physical Review B **82**.2 (2010), p. 024413 (cit. on pp. 87, 92).

[Chi+03] I. Chiorescu, Y. Nakamura, C. M. Harmans, and J. Mooij: *Coherent quantum dynamics of a superconducting flux qubit*. Science **299**.5614 (2003), pp. 1869–1871 (cit. on p. 11).

[CZ95] J. I. Cirac and P. Zoller: *Quantum computations with cold trapped ions*. Physical review letters **74**.20 (1995), p. 4091 (cit. on p. 1).

[CFH97] D. G. Cory, A. F. Fahmy, and T. F. Havel: *Ensemble quantum computing by NMR spectroscopy*. Proceedings of the National Academy of Sciences **94**.5 (1997), pp. 1634–1639 (cit. on p. 1).

[DOT65] P. Das, R. B. de Ouboter, and K. Taconis: "A realization of a London-Clarke-Mendoza type refrigerator". *Low Temperature Physics LT9*. Springer, 1965, pp. 1253–1255 (cit. on p. 50).

[DF61] B. S. Deaver Jr and W. M. Fairbank: *Experimental evidence for quantized flux in superconducting cylinders*. Physical Review Letters **7**.2 (1961), p. 43 (cit. on p. 10).

[DS13] M. H. Devoret and R. J. Schoelkopf: *Superconducting circuits for quantum information: an outlook*. Science **339**.6124 (2013), pp. 1169–1174 (cit. on p. 2).

[DWM04] M. H. Devoret, A. Wallraff, and J. M. Martinis: *Superconducting qubits: A short review*. arXiv preprint cond-mat/0411174 (2004) (cit. on p. 1).

[Dic54] R. H. Dicke: *Coherence in Spontaneous Radiation Processes*. Phys. Rev. **93** (1954), p. 99 (cit. on p. 2).

[DiV+00] D. P. DiVincenzo et al.: *The physical implementation of quantum computation*. arXiv preprint quant-ph/0002077 (2000) (cit. on p. 1).

[Dol77]   G. Dolan: *Offset masks for lift-off photoprocessing*. Applied Physics Letters **31**.5 (1977), pp. 337–339 (cit. on pp. 37, 39, 40).

[DN61]   R. Doll and M. Näbauer: *Experimental proof of magnetic flux quantization in a superconducting ring*. Physical Review Letters **7**.2 (1961), p. 51 (cit. on p. 10).

[Fan61]   U. Fano: *Effects of configuration interaction on intensities and phase shifts*. Physical Review **124**.6 (1961), p. 1866 (cit. on pp. 49, 75).

[Fey59]   R. P. Feynman: *There's plenty of room at the bottom*. Miniaturization (1959), pp. 282–296 (cit. on p. 1).

[Fey82a]   R. P. Feynman: *Simulating physics with computers*. International journal of theoretical physics **21**.6-7 (1982), pp. 467–488 (cit. on p. 1).

[Fey82b]   R. P. Feynman: *Simulating physics with computers*. International Journal of Theoretical Physics **21**.6 (1982), pp. 467–488. DOI: 10.1007/BF02650179 (cit. on p. 2).

[Fil+11a]   S. Filipp, M. Göppl, J. M. Fink, M. Baur, R. Bianchetti, L. Steffen, and A. Wallraff: *Multimode mediated qubit-qubit coupling and dark-state symmetries in circuit quantum electrodynamics*. Phys. Rev. A **83** (2011), p. 063827. DOI: 10.1103/PhysRevA.83.063827 (cit. on p. 2).

[Fil+11b]   S. Filipp, A. F. van Loo, M. Baur, L. Steffen, and A. Wallraff: *Preparation of subradiant states using local qubit control in circuit QED*. Phys. Rev. A **84** (2011), p. 061805. DOI: 10.1103/PhysRevA.84.061805 (cit. on p. 2).

[Fin+09]   J. M. Fink, R. Bianchetti, M. Baur, M. Göppl, L. Steffen, S. Filipp, P. J. Leek, A. Blais, and A. Wallraff: *Dressed collective qubit states and the Tavis-Cummings model in circuit QED*. Physical review letters **103**.8 (2009), p. 083601 (cit. on pp. 49, 92).

[Fri+18]   A. Frisk Kockum, A. Miranowicz, S. De Liberato, S. Savasta, and F. Nori: *Ultrastrong coupling between light and matter*. arXiv:1807.11636 (2018) (cit. on p. 2).

[GAN14]   I. M. Georgescu, S. Ashhab, and F. Nori: *Quantum simulation*. Rev. Mod. Phys. **86** (2014), pp. 153–185. DOI: 10.1103/RevModPhys.86.153 (cit. on p. 2).

[Göp+08]   M. Göppl, A. Fragner, M. Baur, R. Bianchetti, S. Filipp, J. Fink, P. Leek, G. Puebla, L. Steffen, and A. Wallraff: *Coplanar waveguide resonators for circuit quantum electrodynamics*. Journal of Applied Physics **104**.11 (2008), p. 113904 (cit. on pp. 5, 7–9, 23, 65, 68).

[Ima+99]   A. Imamog, D. D. Awschalom, G. Burkard, D. P. DiVincenzo, D. Loss, M. Sherwin, A. Small, et al.: *Quantum information processing using quantum dot spins and cavity QED*. Physical review letters **83**.20 (1999), p. 4204 (cit. on p. 1).

[JC63]   E. T. Jaynes and F. W. Cummings: *Comparison of quantum and semiclassical radiation theories with application to the beam maser*. Proceedings of the IEEE **51**.1 (1963), pp. 89–109 (cit. on pp. 2, 13, 49).

[JNN12]   J. R. Johansson, P. D. Nation, and F. Nori: *QuTiP: An open-source Python framework for the dynamics of open quantum systems*. Computer Physics Communications **183**.8 (2012), pp. 1760–1772 (cit. on pp. 98–101).

[Jos62]   B. D. Josephson: *Possible new effects in superconductive tunnelling*. Physics letters **1**.7 (1962), pp. 251–253 (cit. on pp. 10, 11).

[KMM95]   A. W. Kleinsasser, R. E. Miller, and W. H. Mallison: *Dependence of critical current density on oxygen exposure in Nb-AlO/sub x/-Nb tunnel junctions*. IEEE transactions on applied superconductivity **5**.1 (1995), pp. 26–30 (cit. on p. 29).

[Koc+07]   J. Koch, M. Y. Terri, J. Gambetta, A. A. Houck, D. Schuster, J. Majer, A. Blais, M. H. Devoret, S. M. Girvin, and R. J. Schoelkopf: *Charge-insensitive qubit design derived from the Cooper pair box*. Physical Review A **76**.4 (2007), p. 042319 (cit. on pp. 1, 2, 12, 15, 17, 18, 34, 98).

[Lep+]   J. Leppäkangas, J. D. Brehm, P. Yang, L. Guo, M. Marthlaer, A. V. Ustinov, and M. Weides: *Resonance inversion in a superconducting cavity coupled to artificial atoms and a microwave background*. arXiv:1807.09567 () (cit. on pp. 49, 66, 68, 69, 71–73, 75, 77–85).

[Lis03]   J. Lisenfeld: *Probing quantum states of Josephson junctions by microwaves*. PhD thesis. Master's thesis, Friedrich-Alexander-Universität Erlangen-Nürnberg, 2003 (cit. on p. 11).

[Lis08]   J. Lisenfeld: *Experiments on superconducting Josephson phase quantum bits*. Citeseer, 2008 (cit. on p. 65).

[Mac+14]   P. Macha, G. Oelsner, J.-M. Reiner, M. Marthaler, S. André, G. Schön, U. Hübner, H.-G. Meyer, E. Il'ichev, and A. V. Ustinov: *Implementation of a quantum metamaterial using superconducting qubits*. Nature communications **5** (2014), p. 5146 (cit. on pp. 3, 103, 105).

[Maj+07a]   J. Majer, J. M. Chow, J. M. Gambetta, J. Koch, B. R. Johnson, J. A. Schreier, L. Frunzio, D. I. Schuster, A. A. Houck, A. Wallraff, A. Blais, M. H. Devoret, S. M. Girvin, and R. J. Schoelkopf: *Coupling superconducting qubits via a cavity bus*. Nature **449**.7161 (2007), pp. 443–447. DOI: 10.1038/nature06184 (cit. on p. 2).

[Maj+07b]   J. Majer, J. Chow, J. Gambetta, J. Koch, B. Johnson, J. Schreier, L. Frunzio, D. Schuster, A. Houck, A. Wallraff, et al.: *Coupling superconducting qubits via a cavity bus*. Nature **449**.7161 (2007), p. 443 (cit. on p. 5).

[MW95]   L. Mandel and E. Wolf: *Optical coherence and quantum optics*. Cambridge university press, 1995 (cit. on p. 1).

[Man+09]   V. E. Manucharyan, J. Koch, L. I. Glazman, and M. H. Devoret: *Fluxonium: Single cooper-pair circuit free of charge offsets*. Science **326**.5949 (2009), pp. 113–116 (cit. on pp. 1, 12).

[Mar+11]   M. Mariantoni, H. Wang, T. Yamamoto, M. Neeley, R. C. Bialczak, Y. Chen, M. Lenander, E. Lucero, A. D. O'Connell, D. Sank, M. Weides, J. Wenner, Y. Yin, J. Zhao, A. N. Korotkov, A. N. Cleland, and J. M. Martinis: *Implementing the Quantum von Neumann Architecture with Superconducting Circuits*. Science **334**.6052 (2011), pp. 61–65. DOI: 10.1126/science.1208517 (cit. on p. 2).

[Mar09]   J. M. Martinis: *Superconducting phase qubits*. Quantum Information Processing **8**.2-3 (2009), pp. 81–103 (cit. on p. 11).

[MGC63]   B. T. Matthias, T. H. Geballe, and V. B. Compton: *Superconductivity*. Rev. Mod. Phys. **35** (1963), pp. 1–22 (cit. on p. 50).

[MO33]   W. Meissner and R. Ochsenfeld: *Ein neuer effekt bei eintritt der supraleitfähigkeit*. Naturwissenschaften **21**.44 (1933), pp. 787–788 (cit. on p. 10).

[Moo+99]   J. Mooij, T. Orlando, L. Levitov, L. Tian, C. H. Van der Wal, and S. Lloyd: *Josephson persistent-current qubit*. Science **285**.5430 (1999), pp. 1036–1039 (cit. on p. 11).

[NC02]   M. A. Nielsen and I. Chuang: *Quantum computation and quantum information*. (2002) (cit. on p. 1).

[NK76]   J. Niemeyer and V. Kose: *Observation of large dc supercurrents at nonzero voltages in Josephson tunnel junctions*. Applied Physics Letters **29**.6 (1976), pp. 380–382 (cit. on p. 37).

[Nie74]   J. Niemeyer: *Eine einfache methode zur herstellung kleinster Josephsonelemente*. PTB-Mitteilungen **84** (1974), pp. 251–253 (cit. on pp. 37, 39, 40).

[Nis+07]   A. Niskanen, K. Harrabi, F. Yoshihara, Y. Nakamura, S. Lloyd, and J. Tsai: *Quantum coherent tunable coupling of superconducting qubits*. Science **316**.5825 (2007), pp. 723–726 (cit. on p. 2).

[Onn11]   H. K. Onnes: *The resistance of pure mercury at helium temperatures*. Commun. Phys. Lab. Univ. Leiden **12**.120 (1911), p. 1 (cit. on p. 10).

[PS95]   M. E. Peskin and D. V. Schroeder: *An Introduction To Quantum Field Theory (Frontiers in Physics)*. Westview Press Incorporated, 1995 (cit. on p. 70).

[Poz09]   D. M. Pozar: *Microwave engineering*. John Wiley & Sons, 2009 (cit. on pp. 5, 6, 9, 24, 27, 67).

[RSR07]   A. Retzker, E. Solano, and B. Reznik: *Tavis-Cummings model and collective multiqubit entanglement in trapped ions*. Phys. Rev. A **75** (2007), p. 022312. DOI: 10.1103/PhysRevA.75.022312 (cit. on p. 2).

[Shu+17]   K. V. Shulga, P. Yang, G. Fedorov, M. V. Fistul, M. Weides, and A. V. Ustinov: *Observation of a collective mode of an array of transmon qubits*. JETP letters **105**.1 (2017), pp. 47–50 (cit. on pp. 3, 35, 104).

[SPS07]   M. A. Sillanpää, J. I. Park, and R. W. Simmonds: *Coherent quantum state storage and transfer between two phase qubits via a resonant cavity*. Nature **449**.7161 (2007), pp. 438–442. DOI: 10.1038/nature06124 (cit. on p. 2).

[Sim04]   R. N. Simons: *Coplanar waveguide circuits, components, and systems*. Vol. 165. John Wiley & Sons, 2004 (cit. on p. 7).

[TC68]   M. Tavis and F. W. Cummings: *Exact solution for an N-molecule—radiation-field Hamiltonian*. Physical Review **170**.2 (1968), p. 379 (cit. on pp. 2, 18, 49).

[Tin04]   M. Tinkham: *Introduction to superconductivity*. Courier Corporation, 2004 (cit. on p. 10).

[Vie+00]   C. Vieu, F. Carcenac, A. Pepin, Y. Chen, M. Mejias, A. Lebib, L. Manin-Ferlazzo, L. Couraud, and H. Launois: *Electron beam lithography: resolution limits and applications*. Applied surface science **164**.1-4 (2000), pp. 111–117 (cit. on p. 35).

[VF14]   P. A. Volkov and M. Fistul: *Collective quantum coherent oscillations in a globally coupled array of superconducting qubits*. Physical Review B **89**.5 (2014), p. 054507 (cit. on p. 105).

[WM08]   D. F. Walls and G. J. Milburn: *Quantum optics*. Springer, 2008 (cit. on pp. 70, 71, 73, 74).

[Wen69]   C. P. Wen: *Coplanar waveguide: A surface strip transmission line suitable for nonreciprocal gyromagnetic device applications*. IEEE Transactions on Microwave Theory and Techniques **17**.12 (1969), pp. 1087–1090 (cit. on p. 5).

[WDR97]   C. G. Willson, R. R. Dammel, and A. Reiser: *Photoresist materials: a historical perspective. Metrology, Inspection, and Process Control for Microlithography XI*. Vol. 3050. International Society for Optics and Photonics. 1997, pp. 38–52 (cit. on p. 35).

[Yan+18]   P. Yang, J. D. Brehm, J. Leppäkangas, L. Guo, M. Marthaler, I. Boventer, A. Stehli, T. Wolz, A. V. Ustinov, and M. Weides: *Probing the Tavis-Cummings level splitting with intermediate-scale superconducting circuits*. arXiv preprint arXiv:1810.00652 (2018) (cit. on pp. 90, 92).

List of publications

[Bra+15] J. Braumüller, J. Cramer, S. Schlör, H. Rotzinger, L. Radtke, A. Lukashenko, P. Yang, S. T. Skacel, S. Probst, M. Marthaler, et al.: *Multiphoton dressing of an anharmonic superconducting many-level quantum circuit*. Physical Review B **91**.5 (2015), p. 054523.

[Bre+18] J. Brehm, P. Yang, J. Leppäkangas, L. Guo, A. Ustinov, and M. Weides: *Higher level transition in Tavis-Cummings system with multiple qubits in resonance with the resonator*. In preparation (2018).

[Lep+]   J. Leppäkangas, J. D. Brehm, P. Yang, L. Guo, M. Marthlaer, A. V. Ustinov, and M. Weides: *Resonance inversion in a superconducting cavity coupled to artificial atoms and a microwave background*. arXiv:1807.09567 ().

[Shu+17] K. V. Shulga, P. Yang, G. Fedorov, M. V. Fistul, M. Weides, and A. V. Ustinov: *Observation of a collective mode of an array of transmon qubits*. JETP letters **105**.1 (2017), pp. 47–50.

[Yan+18] P. Yang, J. D. Brehm, J. Leppäkangas, L. Guo, M. Marthaler, I. Boventer, A. Stehli, T. Wolz, A. V. Ustinov, and M. Weides: *Probing the Tavis-Cummings level splitting with intermediate-scale superconducting circuits*. arXiv preprint arXiv:1810.00652 (2018).

Acknowledgements

I am thankful for Dr. Oleksandr Lukashenko for generously sharing his precious experience on operating cryogenic equipment and the great help for running the "UFO" fridge during our measurements. He is an amazing live saver whenever problems occurred to the refrigerator, he responses quickly even over the weekend. The fabrication of my sample is under the help of Lucas Radtke and Dr. Silvia Diewald. Thank you all for the experience about optical and electron-beam lithography, and the great help in the clean room.

I owe a big thanks for the team-work between the members in our group, thank you Andre Schneider, Lukas Grünhaupt, Steffen Schlör, Alexander Stehli and Tim Wolz. I am especially grateful for you to take care of the fridge when I was pregnant, otherwise my experiments would be interrupted for a long time. I want to thank Roland Jehle for the making cables, the PCBs and the support about the electric equipment. Gratitude also goes to the secretaries Steffi Baatz, Ilona Brosch and Birgit Schelske.

I want to thank my dear dad and mom, for their selfless love and being supportive all the time when I make big decisions. I want to thank my beloved husband. You are my super hero, I would not have made it without you. Thank you also my adorable daughter Isabella, you are my sunshine, you make me stronger.

Karlsruhe, June 2018   Ping Yang